POLITECNICO DI TORINO

Master's Degree Programme in
Energy and Nuclear Engineering

Specialist Track: Sustainable Nuclear Energy

Master's Thesis

Numerical Modeling of Laser-Driven Shock Propagation in Targets Relevant to Inertial Confinement Fusion

Supervisors:

Prof. Roberto Bonifetto
Prof. Raffaella Testoni
Prof. Antonio Froio
Dr. Antonio Zurzolo

Candidate:

Giuseppe Maria Fracanzani

July 2026

Abstract

In order to reach the extreme densities and temperatures required for a fusion reaction, laser energy is exploited to irradiate a fuel target from all directions, generating plasma on its surface. As this plasma expands outward, it drives the remaining material inward and produces a highly compressed state at the target center, creating favorable conditions for fusion reactions to occur. This approach is known as inertial confinement fusion because the time over which these reactions can take place is determined only by the inertia of the imploding plasma.

Shock wave propagation in multi-material targets is fundamental to understand material behavior under the extreme conditions relevant to inertial confinement fusion. In this context, low-density polymer foams are of particular interest for target design, although their thermodynamic response to shock compression remains poorly characterized. This thesis develops a numerical framework based on the FLASH code, a high-performance multi-physics simulation code developed by the Flash Center for Computational Science. The objective is to reproduce a laser-driven reference experiment on shock propagation in quartz and TMPTA plastic foams.

This work follows a progressive two-step strategy. First, a simplified hydrodynamic model replaces the laser drive with an equivalent pressure source and describes the materials through a gamma-law equation of state. This step evaluates the extent to which a reduced model, without tabulated equations of state, multi-temperature physics, or explicit laser-plasma interaction, can reproduce the main features of the reference experiment. A second, more physically detailed model is then considered. This stage explicitly simulates laser energy deposition, plasma formation and ablation. Additionally, it introduces tabulated equations of state and a separate energy treatment for ions, electrons and radiation to provide a more realistic description of the target response. The resulting simulations are analyzed in terms of shock position, shock velocity, particle velocity, pressure, and temperature, which are the main quantities used for comparison with the experimental data.

The aim is therefore to establish and test a FLASH-based workflow for the numerical reproduction of laser-driven shock experiments in foam-containing targets. Once validated against the reference case, this framework can support future studies on different foam compositions, densities, and target geometries relevant to inertial confinement fusion applications.

Acknowledgments

The numerical simulations were performed with the FLASH code on the Legion cluster, using computational resources provided by HPC@PoliTO (`www.hpc.polito.it`). The software used in this work was developed in part by the DOE NNSA- and DOE Office of Science-supported Flash Center for Computational Science at the University of Chicago and the University of Rochester.

I would like to express my sincere gratitude to my supervisors, who patiently guided me throughout the development of this thesis. They always promptly provided me with all the material I needed and were consistently available for discussion, offering valuable advice and support at every stage of this work.

A special acknowledgment goes to all the friends who have accompanied me throughout my academic journey. In particular, during my Master's degree, I would like to thank Valeria for her empathy, Giulia for her patience and understanding, and, last but not least, Andrea, whose extraordinary altruism has given me a deeper understanding of the meaning of friendship.

Finally, I must express my deepest gratitude to my family, without whose constant support I could never have reached this milestone, nor any of those that came before it. Thank you for always supporting my past, present, and future choices.

Contents

List of Figures

List of Tables

Chapter 1

Introduction

1.1 Inertial Confinement Fusion

Achieving fusion in laboratory conditions requires the creation of sufficiently hot and dense plasma states, where light nuclei can overcome Coulomb repulsion and undergo fusion reactions. Among the different strategies proposed to reach these conditions, inertial confinement fusion (ICF) represents one of the principal technological approaches. In contrast to magnetic confinement approaches, where plasma is confined over relatively long times by electromagnetic fields, ICF relies on the rapid compression of a small fuel target to extreme density and temperature over very short timescales, such that fusion reactions occur before the target can significantly expand. In this case, confinement is provided by the inertia of the compressed fuel itself.

The general operating principle of ICF is based on the implosion of a spherical pellet, typically containing deuterium-tritium fuel and surrounded by an external ablator layer. When a sufficiently intense driver deposits energy onto the outer surface of the target, the ablator is rapidly heated, ionized, and converted into plasma. This hot plasma expands outward at high velocity, and by momentum conservation the reaction force drives the remaining shell inward. The result is a nearly spherical compression wave that converges toward the pellet center, compressing and heating the inner fuel. If the implosion symmetry, pressure, and temperature are sufficiently high, a central hot spot can form where conditions become sufficient to initiate thermonuclear ignition. Once it occurs, the energetic fusion products, particularly alpha particles, can deposit energy into the surrounding compressed fuel, potentially triggering further burn propagation through the pellet and significantly amplifying the total fusion yield [1].

Different technical strategies have been developed to achieve the conditions required for ignition. In direct-drive ICF, multiple laser beams directly irradiate the target surface, aiming for symmetric ablation and compression. In indirect-drive configurations, laser energy is first deposited into a high-Z enclosure, or hohlraum, where it is converted into x rays that more uniformly irradiate the capsule. A third major concept, fast ignition, separates the compression and ignition phases: the fuel is first compressed, then an additional ultra-intense pulse rapidly heats a localized region to initiate burn [2].

Despite its conceptual simplicity, ICF presents major scientific and technological challenges. Among the primary difficulties are achieving highly uniform energy deposition and compression symmetry, since even small perturbations can seed hydrodynamic instabilities that degrade the implosion performance. In addition, practical energy production would require high driver efficiency, substantial fusion gain, and rapid target repetition

rates. These requirements make ICF not only a plasma physics problem, but also a systems-engineering challenge involving laser technology, target fabrication, and materials science.

The success of inertial confinement fusion is fundamentally determined by how matter behaves under extreme temperature, pressure, and irradiation conditions. For this reason, its study is intrinsically connected to the domain of high-energy-density physics. In laser-driven ICF, target compression is governed by laser-matter interaction, which controls how driver energy is deposited into the target and ultimately determines plasma formation, ablation dynamics, and shock generation.

1.2 Physical and Numerical Framework of Laser-Driven Experiments

Laser-matter interaction is commonly investigated through laser-shot experiments, in which a high-power laser pulse is focused onto a material target in order to generate plasma and rapidly drive matter away from equilibrium. These experiments are directly connected to inertial confinement fusion, since they reproduce on a laboratory scale many of the physical processes involved in laser-driven compression. At the same time, they provide access to pressure and temperature conditions typical of high-energy-density physics, making them a powerful platform for studying matter under extreme conditions [2].

The interpretation of these experiments depends on the physical description adopted for the plasma and for the target material. Plasma can be described at different levels of detail, ranging from kinetic models, which follow the evolution of particle distribution functions, to fluid models, which describe the system through macroscopic quantities. The kinetic description is more general and is required when non-equilibrium effects, collisionless dynamics, or non-local transport are dominant. However, when the relevant length and time scales are large compared with microscopic scales, and when collisions or collective effects allow the definition of local averaged quantities, a fluid description becomes appropriate [3].

Within a fluid description, the plasma and the target are represented through fields such as density, velocity, pressure, and temperature. This approach is particularly useful for studying shock propagation, compression waves, and large-scale hydrodynamic motion in laser-driven targets. The choice of a fluid model, however, still involves different levels of approximation. In the simplest case, matter is described by a single temperature, assuming that ions, electrons, and radiation are sufficiently coupled to be treated as one thermodynamic system. More refined descriptions may instead treat the different components as coupled fluids, for example electrons and ions, exchanging energy and momentum mainly through collisional processes. If radiation transport is also included as an additional transport component, the model becomes a three coupled fluid description.

This distinction is important because laser-driven experiments often involve processes occurring on different relaxation timescales. Electrons can be heated directly by the laser, ions respond through collisions and hydrodynamic motion, and radiation can transport energy through the target. A one-fluid model is therefore a simplified approximation, while two-fluid and three-fluid models allow a more detailed treatment of energy exchange between the different components. The appropriate choice depends on the physical regime, the timescale of interest, and the observables that the simulation aims to reproduce.

In this work, laser-driven shock experiments are modeled within a hydrodynamic

framework using the FLASH code. FLASH is a modular, parallel, multi-physics simulation code originally developed by the Flash Center for Computational Science to study compressible astrophysical flows and thermonuclear flashes [4]. It already includes fully compressible reactive hydrodynamics, adaptive mesh refinement, equation-of-state modules, and thermonuclear reaction networks, making it suitable for problems involving shocks, strong gradients, and reactive flows.

A key feature of FLASH is its modular philosophy. The code is organized in independent units that can be combined to build problem-specific applications, allowing users to select the required physics, geometry, solvers, material models, and runtime parameters. This structure makes it possible to construct simplified hydrodynamic configurations as well as more complete multi-physics simulations. For laser-driven problems, this flexibility is particularly useful because different levels of physical complexity may be introduced depending on the objective of the study.

FLASH also supports adaptive mesh refinement (AMR), which is especially relevant for simulations focused on shock evolution. In shock-dominated problems, the most important gradients are often localized near shock fronts, contact discontinuities, or material interfaces. AMR allows high spatial resolution to be concentrated in these regions while retaining a coarser grid elsewhere, avoiding the computational cost of a uniformly fine discretization over the entire domain. This feature is particularly useful when the goal is to follow the propagation of a shock through a multi-material target, where both the shock front and the interfaces between layers must be adequately resolved.

In addition, FLASH includes capabilities for multi-temperature and reactive-flow modeling, allowing the same numerical framework to be applied to increasingly complex physical descriptions, including radiation hydrodynamics and fusion-related source terms.

1.3 Benchmark with existing work

The experiment by Paddock et al. [5] was designed to investigate the principal Hugoniot of low-density TMPTA plastic foam under laser-driven shock compression, in a pressure range relevant to inertial-confinement-fusion applications. The main objective was to assess whether such a foam can be modeled, at least in this regime, as a homogeneous material with the same average density. This point is particularly important because foam layers are frequently used in ICF-related target designs, while their equation of state remains less well characterized than that of the corresponding dense material. In simulations, foams are often treated as lower-density versions of the corresponding homogeneous material.

The target employed in the experiment had a four-layer structure. From the laser-irradiated side to the rear surface, it consisted of an approximately $40\,\mu$m CH ablator, a thin gold layer of about $3\,\mu$m, an α-quartz reference layer of about $40\,\mu$m, and a TMPTA foam layer of about $40\,\mu$m. The CH layer acted as the laser ablator, while the gold layer was included to absorb x rays generated in the coronal plasma and thereby limit preheating of the downstream layers. Quartz was used as a reference material for both impedance matching and temperature analysis. The foam covered only half of the rear side of the target, producing a step target geometry that allowed diagnostics to observe both the quartz and the foam.

The target was driven by the VULCAN laser using six frequency-doubled beams at 527 nm, arranged to produce a nearly flat-topped focal spot and a top-hat temporal pulse. The pulse duration was varied between about 2 and 9 ns, with total energies between

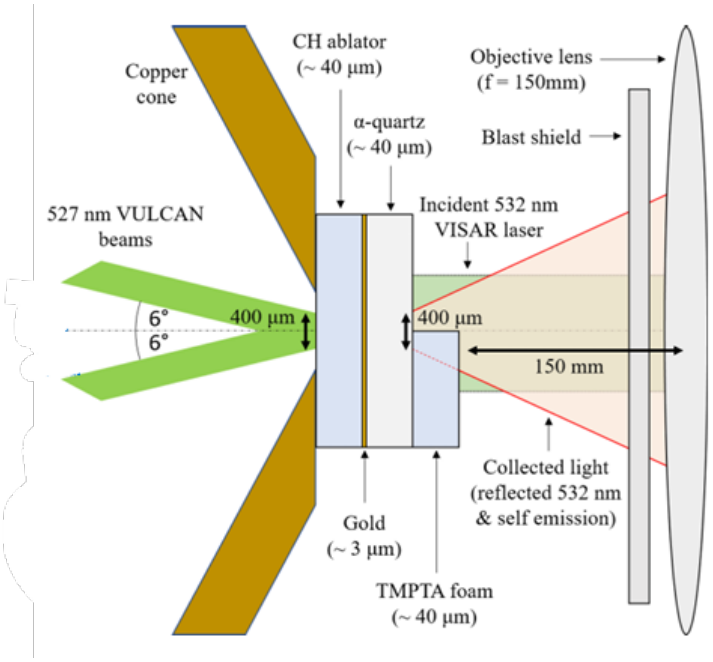

Figure 1.1: Schematic of the layered target used in the Paddock experiment[5].

roughly 300 and 700 J, corresponding to intensities on target from about 3×10^{13} to $2 \times 10^{14}\,\mathrm{W\,cm^{-2}}$. Under these conditions the laser ablated the CH layer and launched a shock wave through the multilayer target. Post-experiment simulations indicate that the ablation front remained confined within the CH layer, so that neither the gold nor the quartz were directly ablated by the laser.

The main diagnostics were VISAR and streaked optical pyrometry (SOP). VISAR provided measurements of the shock velocities in both quartz and foam, which constitute the primary experimental observables. These measurements were then used to reconstruct the thermodynamic state reached in each shot for both quartz and TMPTA foam.

In particular, the quartz state was first determined by intersecting the measured Rayleigh line with the known quartz Hugoniot in the (u_p, P) plane. Once the shocked state in quartz was identified, a quartz release isentrope was constructed. Physically, this release path corresponds to the rarefaction wave generated in quartz when the shock reaches the quartz–foam interface. The release isentrope therefore represents the set of thermodynamic states that quartz can access during unloading, while maintaining continuity conditions at the interface.

The measured foam shock velocity defined a second Rayleigh line, and its intersection with the quartz release isentrope provided the common pressure and particle velocity at the quartz-foam interface. From this impedance-matching procedure, the corresponding state in the foam was determined using the Rankine-Hugoniot relations. Repeating this procedure over multiple shots allowed the reconstruction of the foam Hugoniot.

Temperature was also estimated experimentally using SOP diagnostics, but with significantly larger uncertainties compared to velocity measurements. The SOP signal required on-shot calibration using shocked quartz as a reference, and the foam emission was relatively weak, leading to noisier data. As a consequence, the temperature measurements exhibit large error bars, and the agreement with theoretical predictions is less conclusive than for pressure and velocity. In particular, the reported temperatures tend to be lower than those predicted by tabulated EOS models, although the uncertainty prevents

definitive conclusions.

For the present thesis, this experiment represents a suitable benchmark because it provides directly measured shock velocities together with reconstructed Hugoniot points for a system involving both a well-characterized reference material and a low-density foam. It is important to stress that the primary goal of the experiment is not to investigate shock transmission at material interfaces, but rather to characterize the compression behavior of TMPTA foam and to assess the validity of describing it as a homogeneous material at the corresponding density. In the pressure range explored ($\sim$ 20–120 GPa), the experimental results suggest that this approximation is reasonable.

1.4 Scope of the Work

The aim of this thesis is to develop a FLASH-based simulation framework capable of reproducing shock generation and evolution within the operating range of the reference experiment presented in the previous section. Quantitatively, the benchmark consists of the measured shock velocities in quartz, U_s^{quartz}, and in TMPTA foam, U_s^{foam}, together with the post-shock quantities reconstructed by the impedance-matching procedure: P^{quartz}, T^{quartz}, u_p^{quartz}, P^{foam}, T^{foam}, and u_p^{foam}.

U_s^{quartz} (km/s)	u_p^{quartz} (km/s)	P^{quartz} (GPa)	T^{quartz} (eV)	U_s^{foam} (km/s)	u_p^{foam} (km/s)	P^{foam} (GPa)	T^{foam} (eV)
9.2 ± 0.6	$4.3^{+0.4}_{-0.4}$	106^{+17}_{-16}	–	11.1 ± 1.1	$6.8^{+0.6}_{-0.7}$	$19.2^{+3.0}_{-2.1}$	–
13.4 ± 2.4	$7.0^{+1.8}_{-1.6}$	249^{+123}_{-93}	$0.96^{+0.59}_{-0.40}$	15.9 ± 4.9	$11.1^{+3.2}_{-2.8}$	$44.4^{+19.3}_{-16.0}$	$0.60^{+0.30}_{-0.23}$
13.4 ± 0.4	$7.0^{+0.2}_{-0.2}$	250^{+16}_{-15}	–	22.3 ± 3.5	$10.5^{+0.5}_{-0.5}$	$59.0^{+9.9}_{-7.3}$	–
13.5 ± 1.0	$7.1^{+0.7}_{-0.7}$	253^{+47}_{-42}	$0.98^{+0.21}_{-0.18}$	17.0 ± 2.0	$11.0^{+1.2}_{-1.2}$	$47.4^{+8.6}_{-6.2}$	$0.62^{+0.16}_{-0.13}$
14.3 ± 1.5	$7.7^{+1.0}_{-1.0}$	290^{+73}_{-64}	$1.14^{+0.35}_{-0.28}$	16.3 ± 2.7	$12.1^{+1.9}_{-1.8}$	$50.0^{+12.0}_{-9.4}$	$0.68^{+0.20}_{-0.17}$
14.4 ± 2.7	$7.7^{+2.0}_{-1.9}$	296^{+150}_{-117}	$1.17^{+0.76}_{-0.53}$	14.5 ± 3.3	$12.5^{+3.7}_{-3.3}$	$45.7^{+17.9}_{-14.8}$	$0.69^{+0.35}_{-0.28}$
15.7 ± 1.8	$8.7^{+1.3}_{-1.2}$	362^{+102}_{-87}	–	25.2 ± 2.8	$13.0^{+2.2}_{-2.1}$	$82.9^{+18.8}_{-13.9}$	–
16.9 ± 1.1	$9.5^{+0.8}_{-0.8}$	423^{+69}_{-62}	$1.79^{+0.36}_{-0.31}$	19.0 ± 2.5	$15.1^{+1.5}_{-1.5}$	$72.3^{+13.2}_{-9.6}$	$1.29^{+0.31}_{-0.24}$
21.6 ± 0.8	$13.1^{+0.7}_{-0.7}$	749^{+69}_{-66}	$3.62^{+0.42}_{-0.40}$	22.3 ± 2.3	$21.2^{+1.2}_{-1.4}$	$120.0^{+16.1}_{-10.9}$	$1.43^{+0.32}_{-0.26}$

Figure 1.2: Experimental and reconstructed values used in this thesis as benchmarks [5].

FLASH is first employed to develop a simplified hydrodynamic model of shock propagation through the laser-driven multi-material target used in the experiment. This first approach was initially adopted because the tabulated equations of state required for a more realistic material description were not yet available. The complete laser-plasma interaction is therefore not reproduced; instead, the resulting shock dynamics are investigated using an imposed pressure drive and simplified material models. The objective is to assess whether such a reduced hydrodynamic description, requiring considerably less information about the materials and the laser-target interaction, can still provide a meaningful representation of the system.

A second and more physically detailed modeling approach is then considered. In this case, a complete laser-driven simulation is developed independently from the simplified model. The interaction between the laser and the target, together with the resulting plasma formation, ablation, and shock generation, is explicitly represented. Tabulated equations of state and separate energy descriptions for ions, electrons, and radiation are also introduced to provide a more realistic treatment of the target response.

The thesis is organized into two main parts, corresponding to these two modeling approaches. Part I, comprising Chapters 2-4, presents the simplified gamma-law simulation.

Chapter 2 introduces the physical model adopted to describe shock propagation through the multi-material target, including the hydrodynamic formulation, the interaction of shock waves with material interfaces, and the gamma-law equation of state. Chapter 3 describes the numerical domain, the initial and boundary conditions, and the implementation of the model in FLASH. The corresponding results are presented in Chapter 4, where the simulated pressure, velocity, and temperature states are compared with the experimental benchmark presented in Figure 1.2 and the main limitations of the simplified description are discussed.

Part II, comprising Chapters 5-7, presents the full-physics laser-driven simulation. Chapter 5 introduces the physical description adopted for laser energy deposition, the separate treatment of ions, electrons, and radiation, the tabulated equations of state, and the diffusive energy-transport processes. Chapter 6 describes the numerical setup and its implementation in FLASH. The results are then presented in Chapter 7, where the post-shock quantities are compared with the same experimental values used for the gamma-law simulation. In this chapter, the temporal, one-dimensional, and two-dimensional structures obtained from the simulation are also analyzed.

This two-part structure is intended to assess the capabilities and limitations of the two numerical frameworks within the same experimental reference case [5].

Part I

Gamma-Law Simulation

Chapter 2

Physical Model

2.1 Modeling Framework and Assumptions

In this work, the material response is initially modeled using a simplified hydrodynamic approach based on a gamma-law equation of state. This choice is primarily motivated by the absence of readily available tabulated equations of state for the materials of interest within the present framework. As a consequence, a gamma-law approximation is adopted as a first attempt to reproduce the experimental observations in a controlled and systematic manner.

The analysis focuses on quartz and TMPTA foam, as these are the materials for which experimental data are available from the reference experiment [5]. The objective of this first modeling step is to assess whether an effective gamma-law description, with parameters inferred from experimental data, is capable of reproducing the observed shock behavior. This approach makes it possible to evaluate to what extent such a simplified model can capture the compression response of both a solid material and a low-density foam within a unified framework.

Within this context, a number of simplifying assumptions are introduced. The most relevant one is the adoption of a purely hydrodynamic description, in which the detailed laser-matter interaction is not modeled explicitly. Instead, the laser drive is replaced by an equivalent pressure-driven configuration, allowing the material response to be isolated from the complexities associated with energy deposition and plasma formation. This approximation is also physically consistent with the experimental configuration, in which only the CH ablator directly interacts with the laser, while the quartz and TMPTA layers are compressed by the resulting shock wave rather than by direct laser energy deposition.

The model is formulated within a one-dimensional framework along the direction of shock propagation. Although the experimental configuration is inherently multidimensional, the central region of the target can be reasonably approximated as undergoing planar shock propagation. This simplification is further required to remain consistent with the adopted Sod-like framework, in which a pressure discontinuity drives the formation of a shock wave [6]. As a consequence, geometrical features such as the step configuration of the TMPTA layer are not explicitly modeled.

The fluid dynamics is described by the Euler equations for compressible flow, assuming an inviscid and non-conductive medium. Dissipative processes such as viscosity and thermal conduction are neglected, as they are expected to play a secondary role over the characteristic spatial and temporal scales of interest, where the flow is dominated by compressive and convective effects.

From a thermodynamic point of view, both materials are described using a gamma-law equation of state with effective parameters. This approximation neglects detailed material properties, including phase transitions, electronic contributions, and ionization effects, and therefore represents a significant simplification of the real physical behavior. In this sense, the parameters of the model should be interpreted as effective quantities, calibrated to reproduce the macroscopic response of the materials under shock compression.

The analysis is restricted to the strong shock regime relevant to the experimental conditions. In this limit, the post-shock state becomes weakly dependent on the initial thermodynamic conditions and is mainly determined by the shock velocity and the material properties. In particular, for an ideal gas, the compression ratio approaches a finite asymptotic value, given by $(\gamma + 1)/(\gamma - 1)$, rather than increasing indefinitely with pressure. This behavior supports the use of simplified models to capture the leading-order features of the flow [7].

A single-temperature (1T) description is also adopted, assuming thermal equilibrium between electrons and ions and neglecting ionization. This assumption is further justified by the fact that the quartz and TMPTA layers are not directly ablated by the laser pulse in the experiment [5], and therefore remain in a regime where ionization effects are reduced and a single-temperature approximation provides a reasonable first description of the thermodynamic state.

2.2 Hydrodynamic Description of Shock Propagation

Euler Equations for Compressible Flow Under the assumptions introduced in the previous section, the dynamics of the system is described by the one-dimensional Euler equations for compressible flow. In particular, gravitational effects are neglected, as the characteristic timescales of the problem (of the order of nanoseconds), together with the high pressure drive, make body forces negligible compared to pressure-driven dynamics.

In conservative form, the Euler equations are:

$$\frac{\partial \rho}{\partial t} + \frac{\partial (\rho u)}{\partial x} = 0, \tag{2.1}$$

$$\frac{\partial (\rho u)}{\partial t} + \frac{\partial (\rho u^2 + P)}{\partial x} = 0, \tag{2.2}$$

$$\frac{\partial (\rho E)}{\partial t} + \frac{\partial \left[(\rho E + P) u \right]}{\partial x} = 0, \tag{2.3}$$

where ρ is the mass density, u the fluid velocity, p the pressure, and E the specific total energy, which is defined as the sum of internal and kinetic contributions:

$$E = e + \frac{1}{2} u^2, \tag{2.4}$$

where e is the specific internal energy.

These equations express the conservation of the fundamental physical quantities governing the flow. The first equation represents the conservation of mass, the second describes the conservation of momentum along the flow direction, and the third accounts for the conservation of total energy. Together, they provide a complete description of the evolution of a compressible fluid under the present assumptions. However the system of equations is not closed and requires the introduction of an equation of state (EOS), which provides a relation between the thermodynamic variables. In general, the EOS can

be expressed in the form $P = f(\rho, e)$, allowing the pressure to be determined from the density and internal energy.

Wave Structure in Compressible Flows From a mathematical perspective, the Euler equations constitute a system of non-linear hyperbolic conservation laws. Because of this characteristic, their solutions may develop discontinuities, such as shock waves [6]. In real fluids, however, these discontinuities represent extremely thin regions in which the flow variables vary rapidly but continuously over microscopic length scales [7]. The resulting flow evolution can be described in terms of a limited set of characteristic wave structures, which organize and govern the propagation of disturbances through the system.

Two main types of waves can arise: shock waves and rarefaction waves. Shock waves are propagating discontinuities across which the flow variables undergo abrupt changes. In particular, pressure, density, and velocity increase across the shock front, reflecting the compressive nature of the process. The relation between the pre-shock (1) and post-shock (2) states is determined by the Rankine-Hugoniot jump conditions, which express the conservation of mass, momentum, and energy across the discontinuity [7]:

$$\rho_1(U_s - u_1) = \rho_2(U_s - u_2), \tag{2.5}$$

$$P_1 + \rho_1(U_s - u_1)^2 = P_2 + \rho_2(U_s - u_2)^2, \tag{2.6}$$

$$e_1 + \frac{P_1}{\rho_1} + \frac{1}{2}(U_s - u_1)^2 = e_2 + \frac{P_2}{\rho_2} + \frac{1}{2}(U_s - u_2)^2, \tag{2.7}$$

where U_s is the shock velocity and u_1 , u_2 are respectively the pre and post shock velocity respect to the laboratory system. These relations define the set of physically admissible states that can be reached through shock compression.

By combining the conservation laws, it is possible to derive a relation between thermodynamic quantities that characterizes the shocked states. In particular, the Hugoniot relation can be written in terms of the specific internal energy as

$$e_2 - e_1 = \frac{1}{2}(P_2 + P_1)\left(\frac{1}{\rho_1} - \frac{1}{\rho_2}\right), \tag{2.8}$$

which defines the locus of all possible final states that can be reached from a given initial condition through a single shock. It is important to note that the Hugoniot does not represent a thermodynamic path, but rather a set of admissible end states.

For an ideal gas with constant specific heat, Eq. 2.8 can be combined with the equation of state to obtain explicit relations between thermodynamic variables. In this framework, the shocked states can be conveniently represented in the pressure-volume (P, V) plane, where the Hugoniot curve exhibits a characteristic behavior. In the strong shock regime, the post-shock state becomes weakly dependent on the initial conditions and is mainly determined by the properties of the material. In this limit, the compression ratio approaches a finite asymptotic value,

$$\frac{\rho_2}{\rho_1} = \frac{\gamma + 1}{\gamma - 1}, \tag{2.9}$$

which depends only on the adiabatic index γ. This limiting behavior can be directly observed from the asymptotic trend of the Hugoniot curve in the (P, V) plane in Figure 2.1.

In contrast to shock waves, rarefaction waves correspond to smooth expansion regions in which the flow variables vary continuously. These structures arise when a high-pressure region expands into a lower-pressure environment, leading to a decrease in pressure and density. The transition is not localized at a discontinuity, but occurs over a finite region, forming a continuous fan of states.

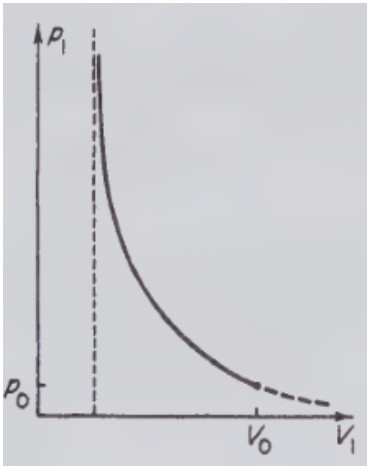

Figure 2.1: Schematic representation of the Hugoniot curve in the P-V plane for an ideal gas [7].

The coexistence of these two wave structures can be clearly observed in the classical shock-tube configuration, where a pressure and density discontinuity evolves into a pattern composed of a shock wave, a rarefaction wave, and a contact discontinuity. In the configuration of figure 2.2, the shock is identified by a sharp jump in all variables and the rarefaction by a smooth variation.

The density jump with continuous pressure and velocity defines a contact discontinuity. It is advected with the local fluid velocity and does not involve compression or expansion. This structure is particularly relevant in multi-material configurations, where it identifies the interface between different materials or between regions that have undergone different thermodynamic evolutions.

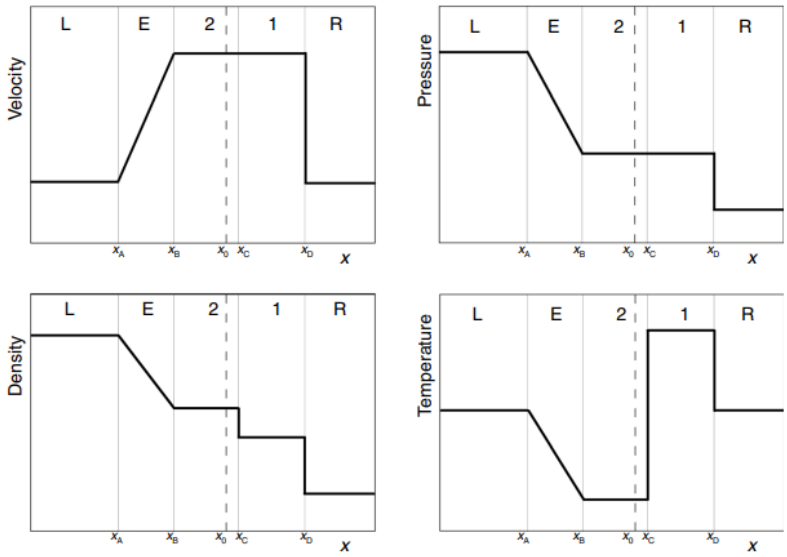

Figure 2.2: Typical solution of a shock-tube problem [8].

These wave structures provide the basis for the interpretation of the flow evolution in the present simulation. In particular, the identification of shock fronts, expansion regions, and contact surfaces allows a direct physical reading of the numerical results, such as the location of the compressed region and the determination of post-shock states.

2.3 Shock Interaction in Multi-Material Systems

Contact discontinuities represent interfaces separating regions characterized by different densities but identical pressure and velocity. In multi-material systems, these discontinuities correspond to physical interfaces between different materials and therefore play a central role in shock propagation across layered targets.

At such interfaces, mechanical equilibrium requires the continuity of pressure and particle velocity, which can be expressed as

$$\begin{aligned} P_1 &= P_2, \\ u_1 &= u_2, \end{aligned} \tag{2.10}$$

where the subscripts denote the states on the two sides of the interface [6].

When a shock wave propagates across an interface separating different materials, the flow becomes more complex due to the mismatch in their mechanical response. In particular, the difference in material properties leads to a redistribution of the wave structure, generating both transmitted and reflected waves.

A key quantity governing this interaction is the shock impedance of the material, commonly defined as

$$Z = \rho_1 U_s, \tag{2.11}$$

where ρ_1 is the initial density and U_s is the shock velocity in the material [9].

The relative impedance between the two media, in which the shock is propagating, determines the nature of the reflected wave. If the second material has a higher impedance, the transmitted shock is stronger and a reflected shock wave is generated in the first

material. Conversely, if the second material has a lower impedance, the transmitted wave is weaker and a rarefaction wave is reflected back into the first material.

The determination of the post-shock state in a given material can be understood in terms of the intersection between conservation laws and thermodynamic constraints. For a given initial state, the Hugoniot relation defines all possible final states that can be reached through shock compression. At the same time, the conservation of mass and momentum across the shock provides additional constraints. Starting from the Rankine-Hugoniot conditions and assuming the upstream material initially at rest ($u_1 = 0$) and the downstream velocity equal to the particle velocity ($u_2 = u_p$), the conservation of mass gives

$$\rho_1 U_s = \rho_2 (U_s - u_p), \tag{2.12}$$

while the conservation of momentum becomes

$$P_2 - P_1 = \rho_1 U_s u_p = Z u_p. \tag{2.13}$$

Equation 2.13 directly defines the Rayleigh line in the (P, u_p) plane, representing a linear relation between pressure and particle velocity for a given shock velocity. It is important to note that the material impedance determines the slope of the Rayleigh line in the (P, u_p) plane. A higher impedance corresponds to a steeper Rayleigh line and therefore, for the same particle velocity, to a larger pressure increase at the post-shock state.

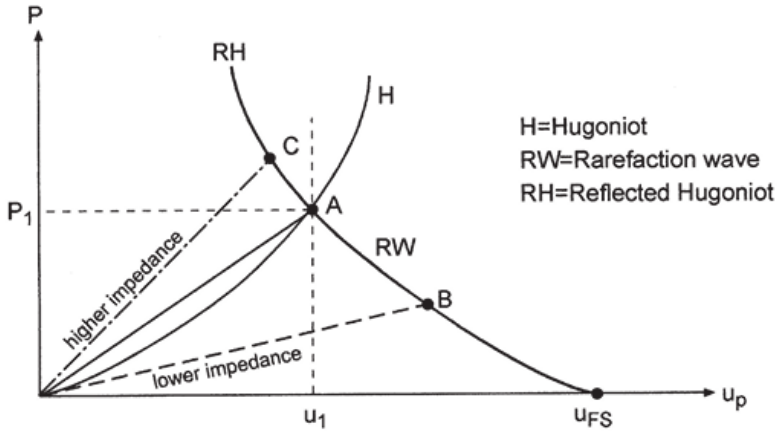

Figure 2.3: Possible shock states B and C resulting from the interaction of a shock with an interface, given the pre-interface shocked state A [9].

The interaction represented in Figure 2.3 starts from state A, which is the shocked state reached in the material before the interface. The resulting post-interface state is obtained by matching the response of this already shocked material with the Rayleigh line of the material beyond the interface.

If this material has a higher impedance, $Z_{\mathrm{C}} > Z_{\mathrm{A}}$, a shock wave is reflected into material A. The resulting back-scattered shock state C is determined by the intersection between the Rayleigh line associated with material C and the reflected Hugoniot of material A. This Hugoniot originates from state A; therefore, its initial pressure and density coincide with those of its already shocked state. Conversely, if the material beyond the interface has a lower impedance, $Z_{\mathrm{B}} < Z_{\mathrm{A}}$, a rarefaction wave is reflected into material

A. This wave, unlike the reflected shock, continuously connects the post-shock state A to the shocked state B, which is determined by the intersection between the Rayleigh line associated with material B and the release curve originating from state A.

In both cases, a shock wave is transmitted into the material beyond the interface. Because of the mechanical-equilibrium conditions expressed in Equation 2.10, pressure and particle velocity are continuous across the interface, making the transmitted shock reaches state C in the higher-impedance case and state B in the lower-impedance case.

This concept forms the basis of impedance-matching techniques, through which the shock state of a material with an unknown equation of state, and therefore an unknown Hugoniot curve, can be determined using a reference material with known properties [2]. In particular, the transmission of a shock into a lower-impedance material is the method used to determine the reference values employed as benchmarks in Figure 1.2.

As already discussed in Section 1.3, the aim of the experiment conducted by Paddock et al. is to determine the shocked state of the TMPTA foam, whose EOS is unknown, through the impedance-matching technique. The quartz slab is used as the reference material [5], and its shocked state corresponds to state A in Figure 2.3.

2.4 Gamma-Law Equation of State

2.4.1 Model Formulation and Physical Interpretation

The thermodynamic behavior of the materials is described using a gamma-law equation of state, which corresponds to the model of an ideal gas with constant specific heats[10]. In this framework, pressure is related to density and specific internal energy through the relation

$$P = (\gamma - 1)\rho e, \tag{2.14}$$

where γ is the adiabatic index.

The specific internal energy can be expressed in terms of temperature as

$$e = c_v T, \tag{2.15}$$

where c_v is the specific heat at constant volume. In the ideal-gas framework, the thermodynamic properties are fully determined by the relations

$$\gamma = \frac{c_p}{c_v}, \qquad R^* = c_p - c_v, \tag{2.16}$$

where c_p is the specific heat at constant pressure and R^* is the specific gas constant.

This model provides a simplified description of matter, in which the internal energy is entirely associated with thermal motion. As a consequence, it neglects several physical mechanisms that are relevant in condensed matter, such as the contribution of the cold compression curve, electronic excitations, and ionization effects. For this reason, the gamma-law EOS is not expected to provide an accurate thermodynamic description of materials such as quartz or polymer foams under shock compression. Despite these limitations, the model can still be employed as an effective description of the hydrodynamic response. In particular, the objective of the present work is not to reproduce the full thermodynamic behavior of the materials, but rather to assess whether a simplified EOS is sufficient to capture the main features of shock propagation.

Within this perspective, the parameters of the model are not interpreted as physical constants of the material, but rather as effective quantities. In particular, an effective

adiabatic index γ and an effective gas constant R^* are introduced, with the aim of reproducing the experimentally observed shock behavior. These parameters are therefore calibrated using experimental data, and their role is to provide a consistent macroscopic description of the flow rather than a detailed microscopic model.

This approach allows to construct a controlled baseline model, in which the complexity of the equation of state is reduced to a minimal set of parameters.

2.4.2 Determination of Effective Parameters

In order to construct an effective gamma-law description for quartz and TMPTA foam, the post-shock experimental quantities reported by Paddock et al. [5] are used directly. In particular, the available measurements of shock velocity U_s, post-shock particle velocity u_p, pressure P, and temperature T are treated as the reference dataset from which the effective parameters of the model are inferred.

The objective of this procedure is not to derive exact material constants, but rather to define effective parameters that best reproduce the experimentally observed shock regime within a simplified hydrodynamic framework. The resulting parameters are therefore intended to represent an averaged macroscopic response over the explored pressure range.

Starting from the Hugoniot relations, and assuming strong shock conditions such that the pre-shock pressure and internal energy are negligible compared to the shocked state,

$$P_1 \approx 0, \qquad e_1 \approx 0,$$

the combination of mass conservation across the shock front, Hugoniot energy conservation, and the gamma-law EOS leads to an explicit relation for the effective adiabatic index:

$$\gamma = 2\left(\frac{U_s}{u_p}\right) - 1. \tag{2.17}$$

Within this approximation, γ depends only on the experimentally measured shock velocity and post-shock particle velocity. This result is physically consistent with the strong shock limit for an ideal gas. In fact, by combining the Rankine-Hugoniot mass conservation relation with the asymptotic compression ratio

$$\frac{\rho_2}{\rho_1} = \frac{\gamma+1}{\gamma-1}, \tag{2.18}$$

the same expression for Eq. 2.17 is recovered.

The effective specific gas constant R^* can be estimated directly from the shocked-state thermodynamic variables using the ideal-gas relation

$$\frac{P}{\rho} = R^* T, \tag{2.19}$$

which gives

$$R^* = \frac{P}{\rho T}. \tag{2.20}$$

Since pressure, density, and temperature are all available from the post-shock experimental state, Eq. 2.20 allows a direct determination of the effective gas constant for each experimental shot.

Applying Eqs. 2.17 and 2.20 to the full experimental dataset produces distributions of γ and R^* values for both quartz and TMPTA foam along all the experimental pressure

range. To obtain representative parameters for each material over the explored shock regime, the sample mean is computed:

$$\bar{x} = \frac{1}{N} \sum_{i=1}^{N} x_i, \tag{2.21}$$

where x_i represents the parameter obtained from each shot and N is the global amount of shots carried during the experiment.

In addition, in order to quantify how representative the mean value is of the full dataset, the relative standard deviation (RSD) is evaluated:

$$\mathrm{RSD}(\%) = \frac{\sigma}{\bar{x}} \times 100, \tag{2.22}$$

with

$$\sigma = \sqrt{\frac{1}{N} \sum_{i=1}^{N} (x_i - \bar{x})^2}. \tag{2.23}$$

The RSD provides a direct measure of the shot-to-shot dispersion of the inferred parameters and therefore indicates whether a single averaged value can reasonably represent the material behavior over the considered experimental range.

The resulting effective parameters are summarized in Table 2.1.

	Quartz γ	Foam γ	Quartz R^* $\left[\frac{\mathrm{J}}{\mathrm{kg\,K}}\right]$	Foam R^* $\left[\frac{\mathrm{J}}{\mathrm{kg\,K}}\right]$
Mean	2.74	2.00	48.63	69.21
Standard deviation	0.25	0.668	35.00	60.37
RSD (%)	9.08	33.43	71.95	87.21

Table 2.1: Effective gamma-law parameters derived from Paddock experimental data using strong shock approximations.

The results show that the effective adiabatic index exhibits a comparatively limited dispersion, particularly for quartz, where the relative standard deviation remains below 10%. This suggests that, within the explored pressure range, a single averaged γ can provide a reasonably representative description of the material compressibility and therefore of its dominant hydrodynamic shock response. For TMPTA foam, the larger spread indicates a reduced but still potentially useful level of representation.

A markedly different behavior is observed for the effective gas constant R^*. In both materials, and especially in the foam, the relative standard deviation is extremely large. This indicates that the inferred thermal parameter is highly sensitive to the specific shocked state and cannot be reliably represented by a single average value. In addition, this large dispersion may reflect also the significantly larger experimental uncertainty associated with temperature measurements.

As a consequence, while the averaged γ values may still support a meaningful effective description of compressive hydrodynamics, the use of a single effective R^* is expected to produce intrinsically poor predictions for temperature. Therefore, even if the gamma-law framework succeeds in reproducing the dominant shock dynamics, significant discrepancies in the thermal reconstruction are already anticipated from the statistical structure of the fitted parameters themselves.

Chapter 3

Simulation Setup

The numerical setup of the problem is based on a modified version of the standard Sod shock-tube example available in FLASH [11]. This choice is motivated by the need to minimize implementation errors by relying as much as possible on a well-tested reference problem.

The Sod problem provides a natural framework to generate a one-dimensional shock within a purely hydrodynamic and single-temperature (1T) description, which is consistent with the modeling assumptions adopted in this work. The original configuration is therefore adapted to reproduce the desired shock conditions relevant for the comparison with experimental data.

3.1 Domain Configuration

The computational domain is constructed as a one-dimensional layered target, designed to reproduce the essential features of the experimental configuration while allowing a controlled initialization of the shock.

The domain consists of three consecutive slabs. From the left boundary to the right, these are: an initial quartz layer, a second quartz layer, and a TMPTA foam layer. The total domain length is $100\,\mu$m.

The first quartz slab has a thickness of $20\,\mu$m and is introduced to allow the shock to develop before reaching the region of interest. In this sense, it does not represent a physical layer of the experimental target, but rather a numerical buffer used to ensure that a well-formed shock is generated before interacting with the subsequent materials.

The second quartz slab and the TMPTA foam slab, each with a thickness of $40\,\mu$m, correspond to the materials of interest for the analysis. These values are chosen to match the experimental configuration, so that the shock propagation and the resulting thermodynamic states can be directly compared with the reference data.

With this setup, the shock is first generated in the initial quartz layer, then propagates through the second quartz slab and finally enters the TMPTA foam. The analysis is focused on the latter two regions, where the comparison with experimental measurements is performed.

3.2 Initial and Boundary Conditions

The simulations are performed using the standard `outflow` boundary conditions available in FLASH for both the left and right domain boundaries. According to the FLASH User's Guide, `outflow` corresponds to a zero-gradient boundary condition and allows shocks to leave the computational domain [11]. This choice is consistent with the present setup, where the aim is to let the generated shock propagate across the domain without artificial reflections.

The initial conditions are prescribed in analogy with the one-dimensional Sod shock-tube configuration. The first quartz slab, which acts as the driver region, is initialized at a pressure P_L, while the remaining part of the domain is initialized at a much lower uniform pressure

$$P_R = 0.26 \text{ GPa}.$$

The initial velocities are set to zero on both sides,

$$u_L = u_R = 0,$$

and the densities are taken equal,

$$\rho_L = \rho_R = 2.65 \ \frac{\text{g}}{\text{cm}^3}.$$

The target pressure to be generated is chosen to match the experimental conditions reported by Paddock et al.[5]. In particular, the values of P^* correspond to the pressures measured in the shocked quartz layer and are used as reference points for the simulations.

The right-state pressure is selected to be much smaller than the driver pressure, in agreement with the strong-shock assumption. At the same time, it is not taken arbitrarily close to zero to avoid numerical instabilities. Within this regime, the solution is not expected to depend sensitively on the precise value of the unperturbed pressure, provided it remains much smaller than P_L.

Under these assumptions, the initial pressure discontinuity between the two quartz slabs can be treated as a one-dimensional Riemann problem. The resulting wave pattern consists of a left-going rarefaction, a right-going shock, and a contact discontinuity.

To determine the appropriate driving conditions, the problem is reduced to a local Riemann problem between two identical materials, quartz. The left state corresponds to the first slab at pressure P_L, while the right state corresponds to the second slab at pressure P_R. This construction isolates the shock generation process from the presence of the TMPTA layer and focuses on the quartz region of interest.

The solution generates a *star* region between the two waves, which physically corresponds to the shocked state of the second quartz slab. The objective is therefore to determine the value of P_L such that the pressure in this region, P^*, matches the experimental target. In this formulation, P^* is fixed a priori, while P_L is the unknown to be determined.

For an ideal gas obeying a gamma-law equation of state, the Riemann solution is obtained by imposing continuity of pressure and velocity across the star region. This leads to the non-linear equation

$$f_L(P^*) + f_R(P^*) + (u_R - u_L) = 0, \tag{3.1}$$

where the functions f_L and f_R describe the relations across the left and right non-linear waves, respectively [6]. In general, these functions depend on the type of wave (shock or rarefaction) and connect the unknown star-region velocity to the known left and right states. In the present case, the left wave is a rarefaction and the right wave a shock, consistently with the imposed initial conditions.

Their explicit expressions are

$$f_L(P^*) = \frac{2a_L}{\gamma - 1}\left[\left(\frac{P^*}{P_L}\right)^{\frac{\gamma-1}{2\gamma}} - 1\right], \tag{3.2}$$

and

$$f_R(P^*) = (P^* - P_R)\sqrt{\frac{A_R}{P^* + B_R}}, \tag{3.3}$$

with

$$a_L = \sqrt{\frac{\gamma P_L}{\rho_L}}, \qquad A_R = \frac{2}{(\gamma+1)\rho_R}, \qquad B_R = \frac{\gamma-1}{\gamma+1}P_R. \tag{3.4}$$

The problem is thus formulated as follows: for a given target pressure P^*, corresponding to the shocked state of the second quartz slab, determine the value of P_L such that the above equation is satisfied. This corresponds to solving the inverse Riemann problem.

The inversion is performed numerically by solving

$$f_L(P^*; P_L) + f_R(P^*) = 0 \tag{3.5}$$

for the unknown P_L, under the condition $P_L > P^*$, which ensures that the left wave remains a rarefaction.

The solution is obtained using a bisection method. The non-linear equation is rewritten in terms of a residual function,

$$R(P_L) = f_L(P^*; P_L) + f_R(P^*), \tag{3.6}$$

so that the problem reduces to finding the root

$$R(P_L) = 0.$$

An initial interval $[P_L^{\min}, P_L^{\max}]$ is identified such that

$$R(P_L^{\min})\, R(P_L^{\max}) < 0,$$

which guarantees that the root is contained within the interval. The interval is then iteratively reduced by halving it at each step, selecting the subinterval in which the sign change is preserved.

At each iteration, the current approximation of the solution is taken as the midpoint of the interval,

$$P_L = \frac{1}{2}\left(P_L^{\min} + P_L^{\max}\right). \tag{3.7}$$

The iteration is stopped when a prescribed tolerance is reached. In particular, convergence is achieved when both the residual and the interval size satisfy

$$|R(P_L)| < \varepsilon, \qquad \frac{|P_L^{\max} - P_L^{\min}|}{|P_L|} < \varepsilon,$$

with tolerance $\varepsilon = 10^{-10}$.

In this way, the pressure imposed in the first slab is not chosen arbitrarily, but is derived from the analytical structure of the Sod problem so as to reproduce the desired shocked state in the second quartz slab.

The resulting driver pressures used in the simulations are summarized in Table 3.1, which completes the definition of the initial setup.

P^* [GPa]	P_L [GPa]
106	257.7
249	606.0
250	608.5
253	615.8
290	706.0
296	720.5
362	881.3
423	1029.9
749	1824.0

Table 3.1: Driver pressures P_L required to obtain the target star-region pressures P^*, corresponding to the shocked state of the second quartz slab and matched to the experimental values reported by Paddock et al.

3.3 Implementation in FLASH

Starting from the original Sod setup, a custom simulation unit is developed under

`FLASH4.8/source/Simulation/SimulationMain/<setup folder>`.

The original two-region configuration is extended to a three-layer structure in order to reproduce the quartz-quartz-TMPTA system described in Section 3.1. The resulting setup remains fully compatible with the one-dimensional, purely hydrodynamic and single-temperature assumptions introduced in Chapter 2.

Problem Structure and Runtime Parameters The geometry and physical parameters of the problem are defined through a set of runtime parameters declared in the `Config` file and stored in the module `Simulation_data.F90`. In particular, the positions of the interfaces between the slabs are controlled by the parameters `sim_x1` and `sim_x2`, while the initial states are specified through `sim_rho`, `sim_p` and `sim_u` for each slab. This approach allows the problem to be fully parametrized, so that different simulation conditions can be explored by modifying only the `.par` file, without requiring changes to the source code.

Initialization of the Flow Field The initialization of the hydrodynamic variables is performed in the subroutine `Simulation_initBlock.F90`. For each computational cell, the physical coordinate is evaluated and used to determine the corresponding slab based on the interface positions.

Depending on the spatial location, the density, pressure and velocity are assigned according to the values of the corresponding slab. At the interfaces, a linear interpolation is

applied in order to construct a smooth transition between adjacent materials. This avoids the presence of perfectly sharp discontinuities at the grid level and improves numerical stability.

The material composition is defined through mass fractions associated with three distinct species, corresponding to the three slabs. In the bulk regions, the mass fraction of the corresponding species is equal to unity, while at the interfaces it is distributed between adjacent species. This allows the definition of thermodynamic variables in mixed cells as weighted averages, ensuring a consistent description of the transition regions and a correct coupling with the Multispecies framework.

Multispecies and Equation of State The simulations are performed using the Multispecies and Multigamma EOS units [11]. Each slab is treated as a distinct species, labeled `SL1`, `SL2` and `SL3`. The thermodynamic properties of each material are defined through the subroutine `Simulation_initSpecies.F90`, where a specific value of the adiabatic index γ is assigned to each species.

In particular, the two quartz slabs are described using the same value of $\gamma = 2.74$, while the TMPTA foam is assigned with $\gamma = 2$, reflecting its distinct compressibility. These values are defined directly within the source code and are therefore not exposed as runtime parameters in the `.par` file.

During initialization, the equation of state is explicitly invoked to compute the internal energy from the prescribed density and pressure. This ensures thermodynamic consistency of the initial state with the selected EOS.

Simulation Setup and Execution The FLASH executable is generated using the standard setup procedure [11]. The problem is configured through the command

```
./setup <setup folder> -1d -auto +hdf5 +parallelIO -site=Legion -nxb=16
```

where the option `-1d` specifies a one-dimensional configuration, `-auto` enables automatic dependency resolution, and `+hdf5 +parallelIO` activate parallel input/output based on the HDF5 format [12].

The flag `-site=Legion` activates the site-specific configuration mechanism provided by FLASH, which allows the build system to use a customized `Makefile.h` instead of the default one by selecting the corresponding directory within `FLASH4.8/sites`. Since no configuration for the target HPC system was available in the standard distribution, a dedicated `Legion` directory was created and a modified `Makefile.h` was defined. This file specifies the compiler options, libraries and system paths required to ensure compatibility with the software environment of the PoliTo Legion cluster [13].

The option `-nxb=16` sets the number of computational cells per block in the spatial direction.

After the setup phase, the code is compiled within the FLASH source directory using the standard `make` procedure, producing the executable named `flash4` [11]. The executable is then used within a separate run directory, where it is coupled with the corresponding `flash.par` file defining the simulation parameters. This separation allows multiple runs with different configurations to be performed without recompiling the code.

Once compiled, the executable reads all runtime parameters from the `flash.par` file [11]. This file fully defines the simulation setup, including initial conditions, boundary conditions, mesh refinement parameters and output control. In this sense, the compiled

code remains unchanged, while different physical configurations are obtained by modifying only the input parameter file.

Simulation Workflow The overall simulation workflow follows the standard FLASH procedure:

1. configuration of the problem through the `setup` command;
2. compilation of the executable (`flash4`);
3. execution of the simulation in a dedicated run directory using the selected `.par` file;
4. generation of output files for post-processing.

This workflow allows for a flexible and reproducible exploration of different shock conditions, as required for the comparison with experimental data.

3.4 Simulation Parameters

This section summarizes the main numerical parameters adopted in the simulations. The chosen configuration is designed to ensure a proper resolution of the shock structure while maintaining numerical stability.

The computational domain is defined in normalized coordinates as $x \in [0, 1]$. This interval corresponds to a physical length of $100\,\mu$m, as described in Section 3.1. In this way, the simulations are performed in code units while preserving a direct mapping to the experimental spatial scale.

Similarly, time is expressed in code units and later converted to physical units during post-processing. The final simulation time is not fixed a priori, but is adapted depending on the imposed driver pressure P_L. In particular, the simulation is stopped once the shock has propagated across the region of interest, so as to avoid unnecessary computation after the shock has exited the domain. The maximum simulated time corresponds to approximately

$$t_{\max} \simeq 10\,\text{ns},$$

which is obtained for the lowest driver pressure case, where the shock propagates more slowly.

The spatial discretization is based on the `PARAMESH` adaptive mesh refinement (AMR) package, using the `FIXEDBLOCKSIZE` mode. The computational domain is initially divided into a prescribed number of blocks, in this case $N_{\text{block}} = 1$, each containing a fixed number of cells, nxb = 16, in which the physical variables are stored, as specified by the setup command presented in the previous section. Through AMR, the grid can be dynamically refined and de-refined, concentrating the computational effort in the regions of the domain where higher spatial resolution is required [11].

The AMR grid unit operates on the blocks. At each refinement level, a parent block is divided into 2^D child blocks, where D is the dimensionality of the problem. Consequently, along each coordinate direction, the block width is halved at every refinement level. The number of cells spanning the width of an original block at a given refinement level l is therefore

$$N_{\text{cells}} = \text{nxb}\, 2^{l-1}. \tag{3.8}$$

The total number of cells along the entire computational domain can then be obtained by multiplying Eq. 3.8 by the initial number of blocks along the considered direction, $N_{\text{block}} = 1$ in this case.

The minimum and maximum refinement levels are set to

$$l_{\min} = 1, \qquad l_{\max} = 6;$$

and the corresponding cell widths are therefore

$$\Delta x_{\min} = \frac{100\,\mu\text{m}}{N_{\text{block}}\,\text{nxb}\,2^{l_{\min}-1}} = 3.12\,\mu\text{m},$$
$$\Delta x_{\max} = \frac{100\,\mu\text{m}}{N_{\text{block}}\,\text{nxb}\,2^{l_{\max}-1}} = 0.20\,\mu\text{m}.$$

Refinement is driven by gradients in pressure and density, using the variables `pres` and `dens`. The corresponding refinement and de-refinement thresholds are set to 0.01 and 0.005, respectively. This choice ensures that the grid is refined in regions where strong gradients develop, in particular across the shock front.

Time integration is controlled through a Courant-Friedrichs-Lewy (CFL) condition[10], with a Courant number set to

$$\text{CFL}_{max} = 0.8.$$

This value provides a stable time evolution while allowing efficient advancement of the simulation.

Output data are written at regular time intervals, with a plot-file interval that is adapted depending on the driver pressure. In practice, the output frequency is chosen such that approximately 5-6 snapshots are obtained for each simulation, uniformly spaced over the shock propagation time. This ensures a consistent temporal resolution of the flow evolution across all the simulated cases.

The physical parameters used in the simulations are consistent with the initial conditions described in the previous section. In particular, the right-state pressure is fixed at $P_R = 0.26\,\text{GPa}$, while the driver pressure P_L is varied according to the values reported in Table 3.1. The densities are set to $\rho = 2.65\,\frac{\text{g}}{\text{cm}^3}$ for quartz and $\rho = 0.26\,\frac{\text{g}}{\text{cm}^3}$ for the TMPTA foam [5].

The parameters $\bar{A}$ and $\bar{Z}$ are set to unity in all simulations. Within the present gamma-law and single-temperature (1T) framework, these quantities do not play a physical role, as the thermodynamic behavior is entirely determined by the equation of state through the parameters γ and ρ. They are therefore treated as formal inputs required by the numerical implementation [11].

Chapter 4

Results and Discussion

The results of the simulations are analyzed in terms of the main quantities characterizing shock propagation, namely the shock velocity U_s, the post-shock particle velocity u_p, the post-shock pressure and the temperature. These quantities are extracted from the spatial profiles obtained through the post-processing procedure and are used for comparison with the experimental data reported by Paddock et al.[5].

In particular, the shock velocity U_s is evaluated from the temporal evolution of the pressure profiles, by tracking the position of the shock front at different times. For each case, the shock position is identified from the pressure jump, and the velocity is estimated as

$$U_s = \frac{x_2 - x_1}{t_2 - t_1}. \tag{4.1}$$

For the quartz layer, the evaluation is performed using the first and last profiles in which the shock remains entirely within the quartz region. Similarly, for the TMPTA foam, the shock velocity is determined using profiles corresponding to its propagation within the foam layer.

All the quantities used for comparison with the experiment, including U_s, u_p, pressure and temperature, are extracted directly from the plotted profiles and therefore involve a degree of qualitative estimation. This approach is consistent with the level of approximation of the present model. In particular, the gamma-law equation of state provides a simplified description of the material response, and the objective of the analysis is to assess whether the simulations are able to reproduce the correct order of magnitude of the experimental observables.

In this context, the comparison with experimental data is not intended as a precise validation, but rather as a consistency check of the scaled gamma-law model against the reference results.

4.1 Post-Processing Methodology

The analysis of the simulation results is carried out through a dedicated post-processing procedure, aimed at extracting physically meaningful quantities from the numerical solution. The simulation outputs are stored in HDF5 format, which requires dedicated tools for data access and manipulation [12]. In addition, the hydrodynamic variables are expressed in code units, so that a conversion to physical units is necessary in order to enable a meaningful comparison with experimental data.

In particular, the post-processing focuses on the reconstruction of spatial profiles of the main fluid quantities and on the evaluation of derived variables, such as temperature, which is not directly available as a primary thermodynamic variable in the present framework. This procedure establishes the link between the numerical model and the physical interpretation of the results, and therefore plays a key role in the validation of the simulations against experimental measurements.

4.1.1 Data Extraction

The numerical results are post-processed using the `yt` analysis toolkit, which provides a flexible interface for reading and manipulating FLASH output files [14]. The post-processing workflow is developed starting from example Python utilities available within the FLASH distribution (in particular in `FLASH4.8/tools/python`), which are adapted to the specific requirements of the present problem.

The simulation data are stored in a sequence of plot-files, each corresponding to a different time instant of the evolution. For each snapshot, the dataset is loaded and the relevant fluid quantities are extracted over the entire computational domain. One-dimensional spatial profiles are then constructed along the direction of shock propagation (i.e. along the x-direction) by sampling the cell-centered data and sorting them according to their spatial coordinate. This procedure ensures a consistent representation of the solution, independently of the internal data layout of the simulation.

The set of variables to be analyzed is not hard-coded, but is instead read directly from the `flash.par` file. This allows the post-processing procedure to remain fully consistent with the simulation setup and easily adaptable to different configurations. The quantities considered in this work include density, pressure, velocity and specific internal energy, which constitute the fundamental variables for the analysis of shock propagation.

Since the simulation employs a multi-species formulation, the local material composition is described in terms of mass fractions [11]. These are used in the post-processing stage to consistently identify the material present in each computational cell. In particular, the two quartz slabs are treated as a single material by combining their respective mass fractions, while the third slab corresponds to the TMPTA foam. This allows a coherent interpretation of the spatial profiles also in the presence of mixed cells at the material interfaces. This information is then used to compute effective thermodynamic properties, required for the evaluation of derived quantities.

The resulting data consist of ordered spatial profiles of the selected variables, which form the basis for the subsequent conversion to physical units and for the evaluation of derived quantities.

4.1.2 Scaling to Physical Units and Derived Quantities

The quantities extracted from the simulation are expressed in code units and must be converted to physical units in order to enable a meaningful interpretation of the results. This conversion is performed consistently with the normalization adopted in the numerical model.

The reference scaling used in the present work is summarized as follows:

- Density:

$$\rho_{\text{phys}} = \rho_{\text{code}} \quad \frac{\text{g}}{\text{cm}^3}$$

- Pressure:
$$P_{\text{phys}} = P_{\text{code}} \quad \text{GPa}$$
- Velocity:
$$u_{\text{phys}} = u_{\text{code}} \quad \frac{\text{km}}{\text{s}}$$
- Spatial coordinate:
$$x_{\text{phys}} = 100\, x_{\text{code}}\, \mu\text{m}$$
- Time:
$$t_{\text{phys}} = 100\, t_{\text{code}}\, \text{ns}$$

A specific treatment is required for the internal energy. In the adopted normalization, the reference energy scale is defined as

$$e_0 = \frac{P_0}{\rho_0}, \tag{4.2}$$

with $P_0 = 1\,\text{GPa} = 10^{10}\,\frac{\text{dyn}}{\text{cm}^2}$ and $\rho_0 = 1\,\frac{\text{g}}{\text{cm}^3}$. This choice is consistent with the selected pressure and density units and ensures that the equation of state retains the correct physical scaling. As a result, the conversion between code and physical units is given by

$$e_{\text{phys}} = e_{\text{code}} \times 10^{10} \quad \frac{\text{erg}}{\text{g}}.$$

A derived quantity of primary interest is the temperature, which is reconstructed from the specific internal energy using the gamma-law equation of state 2.14. Under this assumption, the temperature is given by

$$T = \frac{e}{c_v}. \tag{4.3}$$

All thermodynamic calculations are performed in the CGS system. For this reason, the specific heat must be expressed in $\left[\frac{\text{erg}}{\text{g K}}\right]$. The material-dependent gas constants used in the present work are derived consistently with the same scaling approach adopted for the adiabatic index γ, as can be seen in Table 2.1, and take the values converted to CGS units:

$$R^*_{\text{quartz}} = 48.63 \times 10^4\ \frac{\text{J}}{\text{kg K}}, \quad R^*_{\text{TMPTA}} = 69.21 \times 10^4\ \frac{\text{J}}{\text{kg K}}.$$

The specific heats at constant volume are then computed using the ideal-gas relation

$$c_v = \frac{R^*}{\gamma - 1}, \tag{4.4}$$

which is consistent with the gamma-law equation of state adopted in the simulations.

In the multi-species formulation, the local thermodynamic properties depend on the material composition. The effective specific heat is therefore computed as a weighted average using the local mass fractions:

$$c_{v,\text{eff}} = Y_{\text{quartz}}\, c_{v,\text{quartz}} + Y_{\text{TMPTA}}\, c_{v,\text{TMPTA}}. \tag{4.5}$$

The temperature is then converted to eV using the relation between thermal energy and temperature,

$$E = k_B T, \tag{4.6}$$

where $k_B = 8.617 \times 10^{-5}\,\mathrm{eV\,K^{-1}}$ is the Boltzmann constant, which provides a direct conversion between Kelvin and electronvolts.

Finally, the processed quantities are used to generate spatial profiles of the relevant variables at different times. These profiles provide a direct representation of the shock structure and its evolution, and form the basis for the quantitative analysis presented in the following sections.

4.2 Flow Evolution

In order to illustrate the qualitative behavior of the solution, a representative case is selected corresponding to a driver pressure $P_L = 423$ GPa. This value lies approximately at the center of the experimental pressure range ($\sim$ 100-750 GPa), and therefore provides a meaningful description of the typical flow structure obtained in the simulations. The spatial profiles of density, pressure and velocity are reported at two representative times, corresponding to a phase in which the shock is still propagating within quartz and a later stage in which it has entered the TMPTA foam. The dashed vertical lines indicate the initial positions of the material interfaces.

The overall structure of the solution is consistent with the classical Sod problem. Starting from the initial pressure discontinuity between the two quartz slabs, the solution evolves into a characteristic three-wave pattern composed of a left-going rarefaction, a right-going shock, and a contact discontinuity.

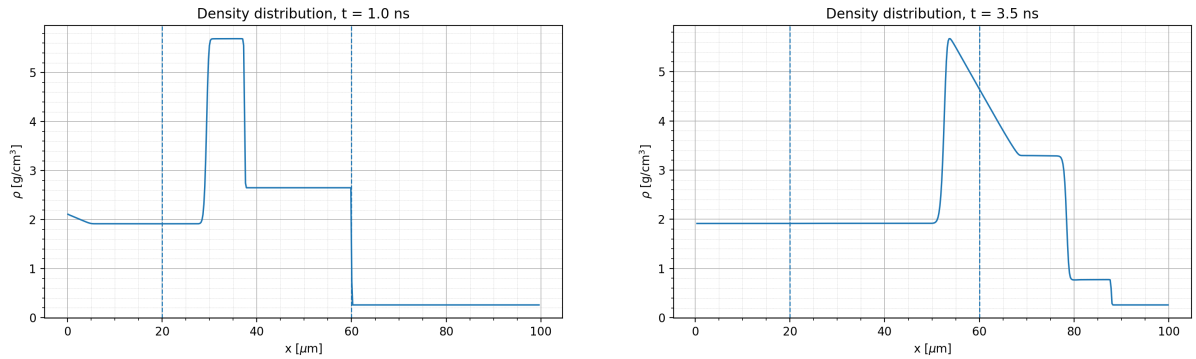

(a) Shock in quartz

(b) Shock in TMPTA

Figure 4.1: Spatial distribution of density at two representative times. The dashed vertical lines indicate the initial positions of the material interfaces.

Density evolution The density profiles clearly highlight the main wave structures. A sharp increase identifies the shock front, followed by a well-defined post-shock plateau, while the contact discontinuity appears as a jump in density without a corresponding pressure discontinuity.

The density distribution on the left-hand side of the shock in the early stage differs from the classical Sod case. This behavior originates from the initial configuration, in which the two quartz slabs have the same density but different pressures, and therefore

correspond to different thermodynamic states. Each slab is initially in its own equilibrium state, but the global configuration is non-uniform. When the discontinuity is released, the solution evolves such that the second slab is compressed by the shock, transitioning to a higher-pressure state. As a consequence of the compressive nature of the shock, both temperature and density increase in this region, consistently with the gamma-law equation of state.

In contrast, the first slab experiences a rarefaction wave, which leads to an expansion of the material and a corresponding decrease in density.

At later times, when the shock reaches the quartz-TMPTA interface, an additional density discontinuity is observed. This feature is associated with the location of the contact surface, which is characteristic of the Sod solution and is present at each state interface. In fact, both the quartz-quartz and quartz-TMPTA interfaces evolve as contact discontinuities and propagate through the domain.

The density jump is therefore a convenient indicator of its position. In the case of the quartz-TMPTA interface, the density decreases from left to right, reflecting the transition toward a lower-impedance material. Conversely, at the quartz-quartz interface, where both materials share the same initial density but evolve toward different thermodynamic states, the density exhibits an increase from left to right.

From Figure 4.1, the position of the contact surface at $t = 3.5\,\text{ns}$ can be estimated to be approximately $x \simeq 78\,\mu\,\text{m}$.

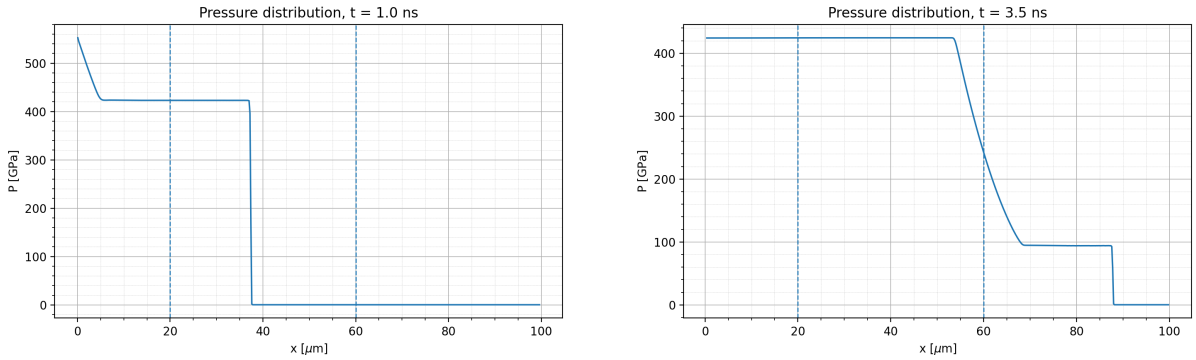

(a) Shock in quartz

(b) Shock in TMPTA

Figure 4.2: Spatial distribution of pressure at two representative times. The dashed vertical lines indicate the initial positions of the material interfaces.

Pressure evolution The pressure profiles show a continuous expansion fan on the left-hand side, corresponding to the rarefaction wave. Between the rarefaction and the shock front, a flat region is observed, corresponding to the uniform post-shock pressure (plateau). The shock itself is identified by a sharp discontinuity separating this plateau from the unperturbed region on the right.

In contrast to the density, no discontinuity is observed at the contact surface, confirming that pressure remains continuous across this interface, as required by mechanical equilibrium.

Velocity evolution The velocity profiles show the expected behavior associated with the wave structure. The rarefaction region is characterized by a smooth increase in velocity, while the region between the rarefaction and the shock exhibits a nearly constant

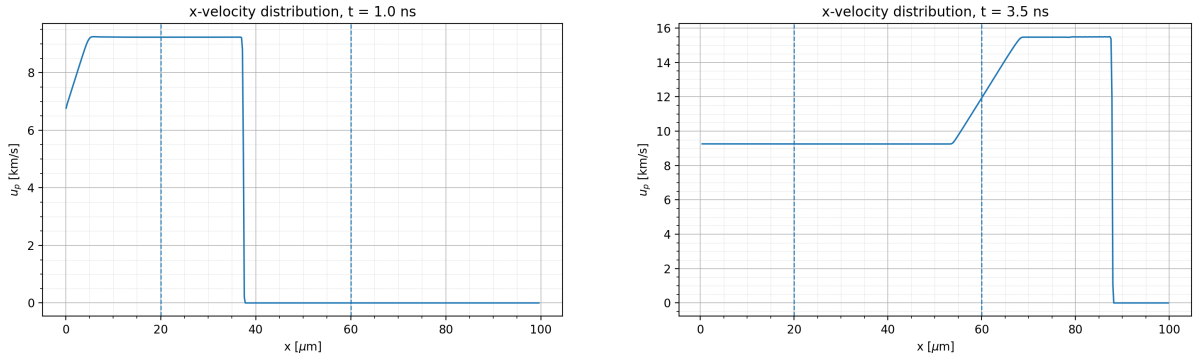

(a) Shock in quartz

(b) Shock in TMPTA

Figure 4.3: Spatial distribution of velocity at two representative times. The dashed vertical lines indicate the initial positions of the material interfaces.

particle velocity. The displacement of the velocity discontinuity between the two times clearly indicates the propagation of the shock front.

When the shock enters the TMPTA foam, an increase in the particle velocity is observed, consistent with the lower density and therefore lower impedance of the material. This effect is accompanied by a corresponding modification of the density jump, as previously discussed.

Overall, the spatial profiles confirm that the numerical setup correctly reproduces the expected wave pattern and the interaction between different materials. This qualitative agreement provides a first validation of the modeling approach and supports the subsequent quantitative analysis.

4.3 Pressure and Velocity Analysis

4.3.1 Quartz Layer

The analysis of the shock propagation is first carried out in the quartz region, corresponding to the second slab of the simulation. The first slab is used only as a driver to impose the desired shock conditions and is therefore not considered in the quantitative analysis.

For each simulation, the shock velocity U_s is evaluated by tracking the position of the pressure discontinuity over time, consistently with Eq. (4.1), while the post-shock particle velocity u_p is obtained from the plateau region behind the shock front. As discussed previously, these quantities are extracted directly from the spatial profiles and therefore involve a qualitative estimation.

Figure 4.4 shows the post-shock particle velocity as a function of the imposed driver pressure. The numerical results exhibit a clear increasing trend with pressure, in agreement with the experimental data. A good qualitative agreement is observed over the entire pressure range, with simulated values lying within the experimental uncertainty for most of the cases.

The corresponding results for the shock velocity are reported in Figure 4.5. Also in this case, the simulations reproduce the expected monotonic increase of U_s with pressure. The level of agreement with the experimental data is comparable to that observed for the particle velocity, with numerical values generally falling within the experimental uncertainty.

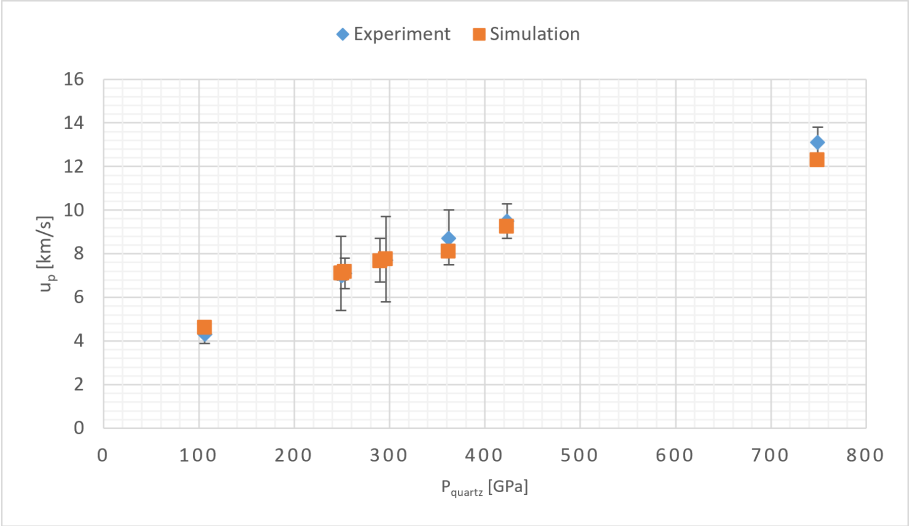

Figure 4.4: Post-shock particle velocity u_p in quartz as a function of the imposed driver pressure. Simulation results (orange) are compared with experimental data (blue) from Paddock et al. [5].

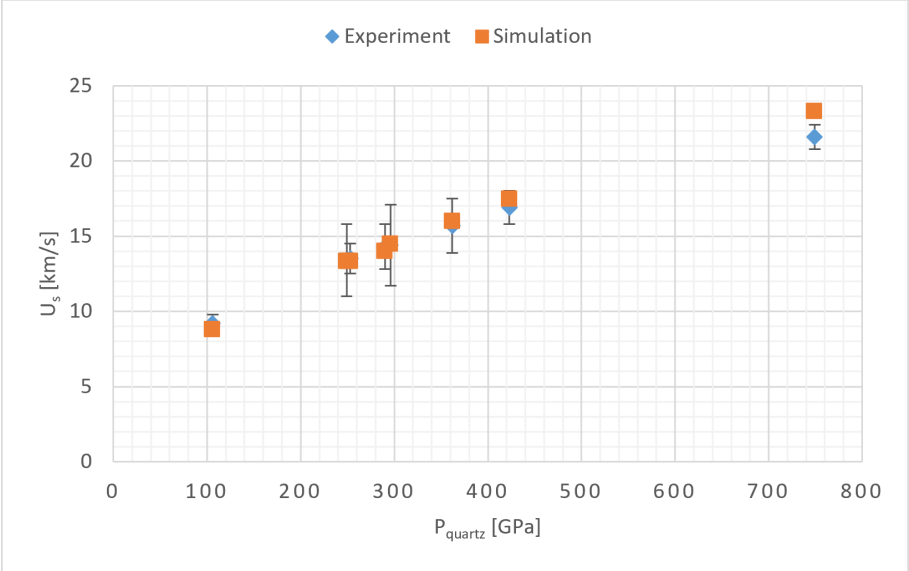

Figure 4.5: Shock velocity U_s in quartz as a function of the imposed driver pressure. Simulation results (orange) are compared with experimental data (blue) from Paddock et al. [5].

In order to provide a quantitative estimate of the agreement, the relative error is defined as

$$\varepsilon = \frac{|q_{\text{sim}} - q_{\text{exp}}|}{q_{\text{exp}}}. \tag{4.7}$$

The maximum relative errors obtained are 7.81% for the shock velocity and 6.98% for the particle velocity, confirming the overall consistency between simulation and experimental data.

The agreement observed for both U_s and u_p indicates that the simulations are able to reproduce the hydrodynamic response of the material under shock compression.

Since U_s and u_p are related through the Rankine-Hugoniot relations, their consistency provides a useful indication that the simulated states are compatible with the expected shock behavior. However, this agreement should be interpreted as a partial validation of the approach, limited to the hydrodynamic description.

It is important to emphasize that the equation of state adopted in the simulations is a gamma-law model, applied within a one-dimensional framework and neglecting several relevant physical effects, such as ionization and detailed material properties. Within this context, the objective of the analysis is limited to reproducing the correct order of magnitude of the experimental observables.

For this reason, the level of agreement obtained is considered satisfactory, and no further quantitative accuracy is expected from the present model. The results therefore support the use of the scaled gamma-law approach as a qualitative tool for describing shock propagation in quartz.

4.3.2 TMPTA Foam

The analysis is extended to the TMPTA foam, corresponding to the third slab of the simulation. In this region, the shock is not directly imposed, but results from its transmission through the quartz-foam interface. As a consequence, the shocked state in the foam depends on both the incoming shock conditions and the impedance mismatch between the two materials.

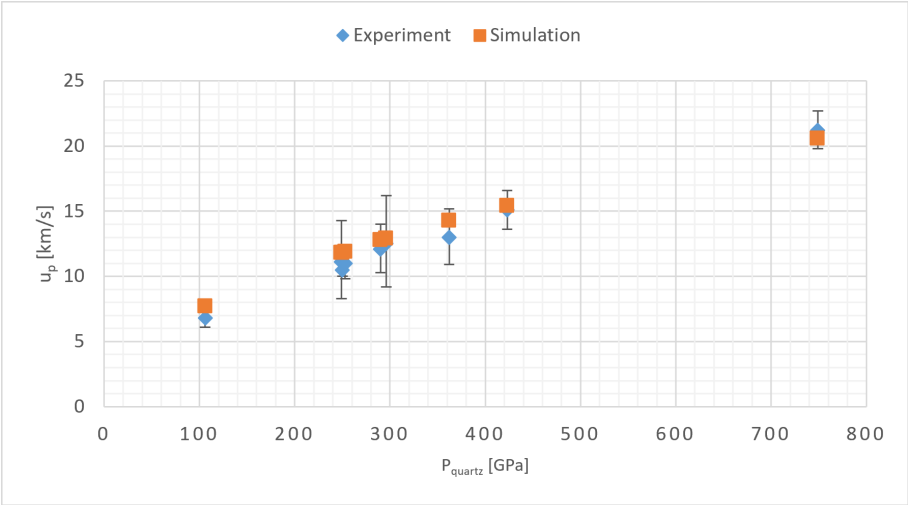

Figure 4.6: Post-shock particle velocity u_p in TMPTA foam as a function of the imposed driver pressure. Simulation results (orange) are compared with experimental data (blue) from Paddock et al. [5].

Figure 4.6 shows the post-shock particle velocity in the foam. As in the quartz case, the numerical results exhibit a clear increasing trend with the driver pressure. A good qualitative agreement with the experimental data is observed over the entire pressure range, with simulated values generally lying within the experimental uncertainty.

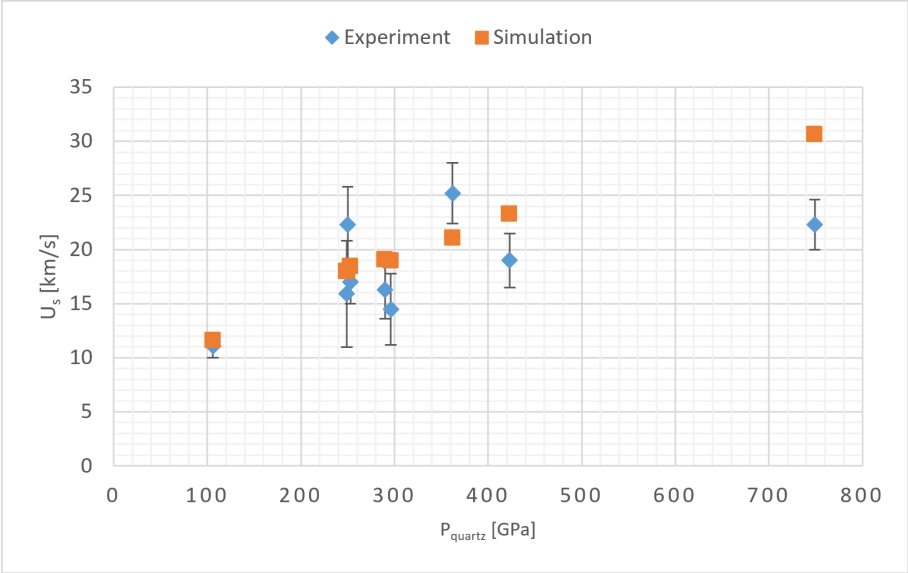

Figure 4.7: Shock velocity U_s in TMPTA foam as a function of the imposed driver pressure. Simulation results (orange) are compared with experimental data (blue) from Paddock et al. [5].

The corresponding results for the shock velocity are reported in Figure 4.7. While the overall increasing trend of U_s with pressure is correctly reproduced, noticeable deviations from the experimental data appear, especially at higher pressures. In this case, the agreement is qualitatively less accurate than for the particle velocity.

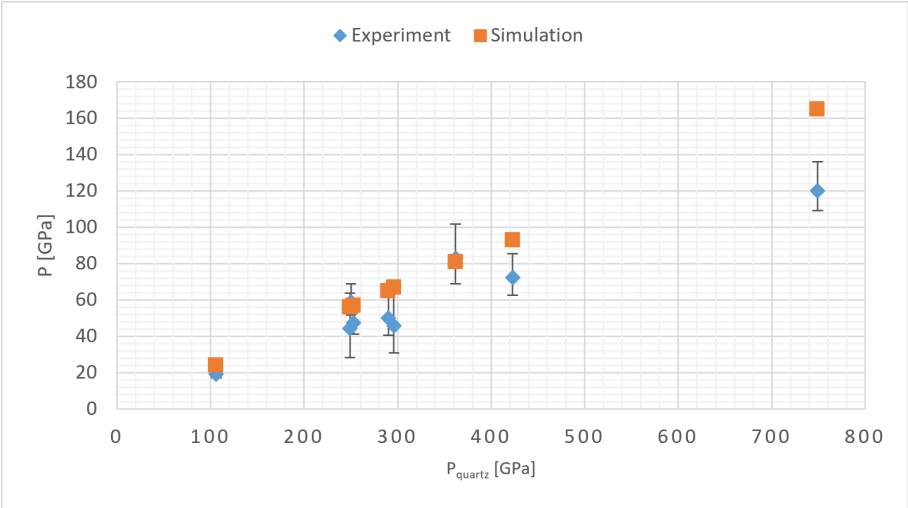

Figure 4.8: Post-shock pressure in TMPTA foam as a function of the imposed driver pressure. Simulation results (orange) are compared with experimental data (blue) from Paddock et al. [5].

The post-shock pressure in the foam is shown in Figure 4.8. The simulations reproduce the general trend with increasing driver pressure; however, significant discrepancies are observed, particularly at higher pressures; in a similar way of U_s.

Using Eq. (4.7), the maximum errors obtained in the foam are 37.34% for the shock velocity, 13.24% for the particle velocity, and 46.61% for the pressure.

The larger discrepancies observed for U_s and pressure can be attributed to the increased sensitivity of the transmitted shock to the approximations of the model, while u_p remains comparatively more consistent with the experimental data. In contrast to the quartz case, the foam response is not directly controlled by the imposed driver conditions, making it more dependent on the accuracy of the equation of state and on the simplified physical description.

Overall, the simulations reproduce the correct qualitative dependence of all the considered quantities on the driver pressure. In particular, the agreement obtained for u_p confirms that the order of magnitude of the hydrodynamic response is captured, while the deviations observed in U_s and pressure highlight the limitations of the present model in describing the transmitted shock in a low-impedance material.

These results indicate that the scaled gamma-law approach provides a consistent qualitative description of shock propagation across different materials, despite showing some limitations in configurations where the shock is not directly imposed but results from material interactions.

4.4 Temperature Evolution

4.4.1 Spatial Temperature Structure

The temperature profiles are analyzed using the post-processed data described in Section 3.5, where temperature is reconstructed from the internal energy (see Eq. (4.3)). The spatial distributions at two representative times are shown in Figure 4.9.

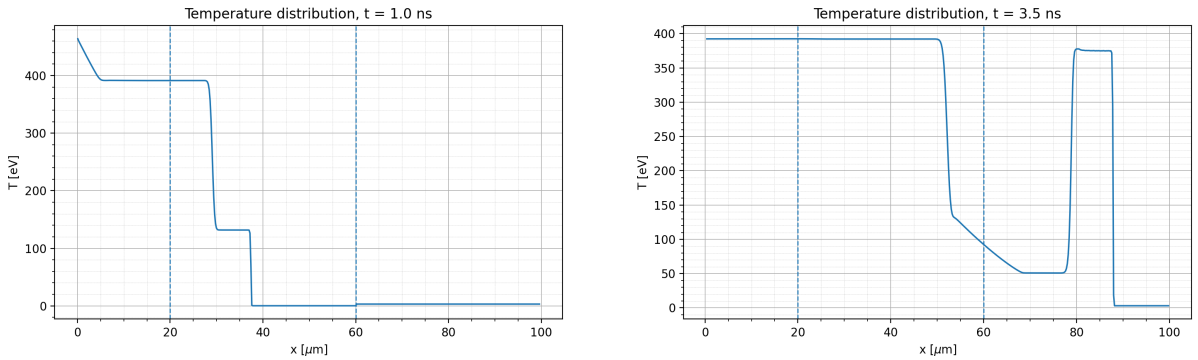

(a) Shock in quartz

(b) Shock in TMPTA

Figure 4.9: Spatial distribution of temperature at two representative times. The dashed vertical lines indicate the initial positions of the material interfaces.

The temperature profiles reflect the underlying hydrodynamic structure of the solution. A sharp increase identifies the shock front, followed by a nearly uniform post-shock plateau, while the rarefaction region is characterized by a gradual decrease in temperature due to expansion.

However, the behavior in the quartz region differs from the classical Sod problem. When the shock is still propagating within the second quartz slab, the temperature in this region remains lower than in the first slab, even after the passage of the shock. This feature is consistent with the interpretation already discussed for the density distribution in Section 4.1.

In the first slab, the pressure is initially very high while the density is fixed, which implies a correspondingly large internal energy in order to satisfy the gamma-law relation. In contrast, the second quartz slab is initialized at the same density but at a much lower pressure. When the shock propagates into this region, the increase in pressure is not entirely accommodated by an increase in internal energy, but is partially supported by material compression, i.e. by an increase in density. As a consequence, the post-shock internal energy, and therefore the temperature, remain lower than in the initial driver region.

It is worth noting that, in the quartz region, the temperature profiles may suggest the presence of a second shock when observed from right to left. This apparent discontinuity is not associated with the formation of an additional shock front, but instead corresponds to the interface between the first quartz slab (the driver) and the second quartz slab.

This interpretation is consistent with the behavior observed in the density profiles (see Section 4.1), where a secondary discontinuity is present downstream of the main shock plateau. Although both regions consist of the same material, they correspond to different initial thermodynamic states, characterized by identical densities but significantly different initial pressures.

As a consequence, even after the passage of the shock, the two regions retain different internal energy levels, which results in a discontinuity in temperature across the interface. At the same time, pressure and velocity remain continuous at this location, as required by the Sod solution for a contact discontinuity. This confirms that the observed feature is not a shock, but rather the material interface separating the two initial states.

At later times, when the shock reaches the quartz-TMPTA interface and enters the foam, the temperature distribution evolves toward a structure more consistent with the classical Sod solution. In this region, a clear post-shock plateau is observed, associated with a strong temperature increase across the shock front. This behavior is consistent with the lower density and lower adiabatic index of the foam, which make the temperature more sensitive to pressure variations. As a result, the shocked TMPTA exhibits a larger temperature increase, in agreement with the standard Sod configuration, where the right state is characterized by lower density and pressure compared to the left state.

4.4.2 Temperature as a Function of Driver Pressure

The dependence of the post-shock temperature on the imposed driver pressure is reported in Figure 4.10 for quartz and in Figure 4.11 for the TMPTA foam.

In both materials, the simulations exhibit a monotonic increase of the post-shock temperature with increasing driver pressure. This trend is consistent with the expected response of an ideal gas described by a gamma-law equation of state, where higher pressures correspond to higher internal energies and therefore higher temperatures.

Despite this qualitatively correct behavior, the comparison with experimental data shows that the simulated temperatures are significantly higher than the measured values, lying well outside the experimental range over the entire pressure domain. This indicates that the model does not provide a physically accurate description of the thermal state.

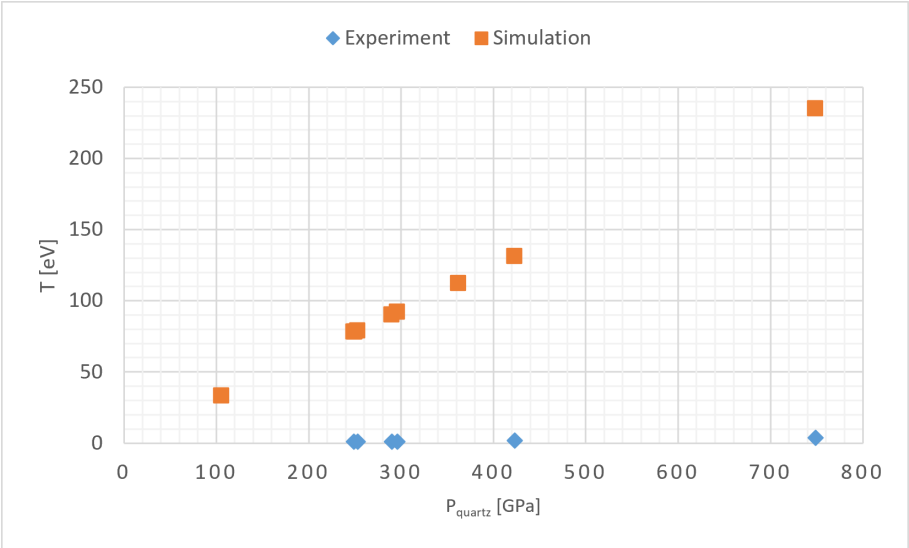

Figure 4.10: Post-shock temperature in quartz as a function of the imposed driver pressure. Simulation results (orange) are compared with experimental data (blue).

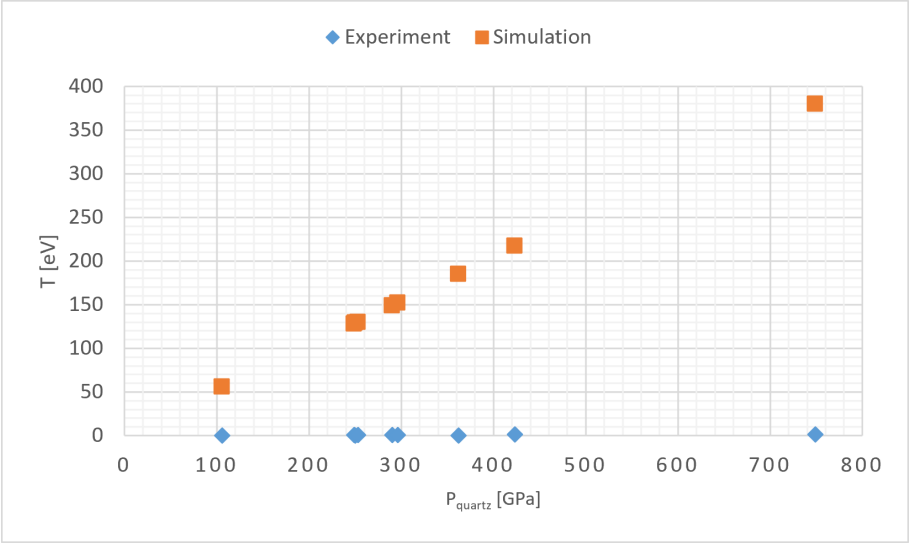

Figure 4.11: Post-shock temperature in TMPTA foam as a function of the imposed driver pressure. Simulation results (orange) are compared with experimental data (blue) from Paddock et al. [5].

Overall, the gamma-law model reproduces the qualitative trend of temperature with the driving conditions, but fails to capture the correct thermal scale. The implications of this discrepancy will be discussed in the following section.

4.5 Model Assessment and Further Improvements

4.5.1 Model Performance

The overall performance of the gamma-law model can be assessed by comparing the simulation results with the experimental data across the different observables considered in this work.

A summary of the maximum relative errors and of the number of simulation points lying within the experimental uncertainty bounds is reported in Table 4.1.

Quantity	**Quartz**		**TMPTA Foam**	
	Max Error	Within Bounds	Max Error	Within Bounds
Shock velocity U_s	7.81%	8/9	37.34%	4/9
Particle velocity u_p	6.98%	9/9	13.24%	9/9
Pressure	-	-	46.61%	5/9
Temperature	Out of scale	0/9	Out of scale	0/9

Table 4.1: Summary of the maximum relative errors and number of simulation points lying within the experimental uncertainty bounds.

The results show that the model reproduces the correct qualitative trends for all hydrodynamic quantities. In particular, both the shock velocity U_s and the particle velocity u_p exhibit a good level of agreement with the experimental data in quartz, with relative errors below 10%.

At the same time, Table 4.1 shows that most of the hydrodynamic results lie within the experimental uncertainty bounds, even in cases where the relative error is not negligible. This is particularly evident for the particle velocity, which lies within the experimental range for all simulated cases in both quartz and foam, and for the shock velocity in quartz, where 8 out of 9 points fall within the experimental uncertainty.

In the TMPTA foam, the agreement is generally worse, especially for the shock velocity and pressure, while the particle velocity remains comparatively closer to the experimental values. This indicates that the model is able to capture the order of magnitude of the hydrodynamic response, but its accuracy decreases in configurations where the shock is not directly imposed, but results from transmission across a material interface.

Nevertheless, a non-negligible fraction of the foam results still lies within the experimental uncertainty bounds, as shown in Table 4.1. This suggests that, despite larger deviations, the model retains a partial predictive capability for the hydrodynamic behavior even in the transmitted shock regime.

A markedly different behavior is observed for the temperature. As discussed in Section 4.3, the simulated temperatures are significantly higher than the experimental values, lying well outside the experimental range over the entire pressure domain. This indicates that, while the model provides a consistent hydrodynamic description, it fails to reproduce the correct thermodynamic scale, with no simulated point falling within the experimental uncertainty bounds.

Overall, the gamma-law model shows good hydrodynamic consistency, particularly in the quartz region, where most of the results lie within the experimental uncertainty bounds. At the same time, the larger deviations observed in the foam and the systematic discrepancy in temperature highlight the limitations of the model in capturing the full thermo-fluid dynamic behavior of the system.

4.5.2 Physical Interpretation and EOS Implications

The discrepancies observed in the results are not associated with numerical issues, but rather with the physical assumptions underlying the equation of state.

The gamma-law EOS provides a simplified description that is well suited for ideal gases, where the internal energy is directly associated with thermal motion. However, the materials considered in this work, such as quartz and TMPTA foam, belong to the condensed matter regime, where the thermodynamic response is governed by additional physical mechanisms.

In particular, in condensed matter a significant fraction of the internal energy is stored in forms that are not purely thermal. These include the elastic compression of the material (often described through a cold curve), lattice degrees of freedom, and electronic contributions at higher energies. As a consequence, the relation between pressure, density and internal energy cannot be reduced to a simple proportionality, and the conversion of internal energy into temperature is not straightforward.

This limitation is directly reflected in the temperature results, which are systematically overestimated by the model. However, the impact of the EOS approximation is not limited to thermodynamic quantities. The deviations observed in the foam region indicate that the transmitted shock and its interaction with material interfaces are also sensitive to the equation of state. In particular, the accuracy of the shock transmission at the quartz-TMPTA interface depends on the correct description of material compressibility and impedance, which are only approximately captured by the gamma-law model.

Therefore, a more realistic EOS is required not only to improve the thermodynamic description, but also to obtain a more accurate thermo-fluid dynamic representation of the experiment, especially in configurations involving multiple materials and interfaces.

An additional limitation of the present setup is the absence of the ablator and gold layers present in the experimental configuration of Paddock et al. These layers play a fundamental role in the generation and shaping of the shock. In the current model, they are not included, as no experimental data are available to calibrate the gamma-law parameters for these materials. As discussed in the previous chapters, the scaling procedure adopted in this work relies on experimental Hugoniot data, which are not available for these additional layers within the scope of the reference experiment.

Despite these limitations, the results show that the gamma-law model is able to reproduce the main qualitative features of the shock propagation. In particular, the overall hydrodynamic behavior, including the structure and evolution of the shock, is captured consistently. This suggests that the single-temperature (1T) approximation, at least at the level of macroscopic shock dynamics, may represent a reasonable first-order description of the problem.

Nevertheless, a more accurate modeling of the experiment requires the adoption of advanced EOS models capable of describing the behavior of condensed matter under compression. Examples include semi-empirical models such as the Mie-Grüneisen EOS [15], as well as tabulated equations of state, such as SESAME [16] or FEOS [17], which

incorporate experimental data and more detailed physical descriptions.

The adoption of such models would allow for a more reliable description of both the thermodynamic properties and the interaction of shocks with material interfaces, providing a more complete and physically accurate representation of the experimental configuration.

Part II

Full-Physics Laser-Driven Simulation

Chapter 5

Physical Model

5.1 Full-Physics HEDP Model

In this part of the work, a higher-fidelity model is adopted to investigate the laser-driven experiment of [5]. The gamma-law model discussed in the previous part provided a controlled hydrodynamic baseline, whose purpose was to simulate with a simplified implementation the propagation of a shock wave through the multilayer target. However, this description also introduced important differences with respect to the experimental configuration. In particular, the shock was generated by imposing an equivalent hydrodynamic pressure, so that the interaction between the laser and the ablator, the associated energy deposition, and the subsequent plasma formation were not explicitly described. Moreover, the model assumed a single-temperature fluid, corresponding to instantaneous thermal equilibrium between ions and electrons. Finally, although the effective values of γ and R_{spec} were chosen to mimic the material response in the pressure range of interest, the closure remained that of a gamma-law ideal gas and could not describe the thermodynamic behavior of real materials over a wide range of densities and temperatures.

The model now adopted is therefore intended to move closer to the physical chain occurring in high energy deposition physics (HEDP), particularly in the experiment under analysis. The main conceptual change is that the shock is no longer prescribed through an equivalent pressure drive. Instead, it is generated as a consequence of the laser energy deposition, plasma formation, ablator expansion, and ablation-pressure build-up. The laser is treated as an explicit energy source and the ablation pressure responsible for shock launch emerges from the response of the irradiated material. In this way, the simulation can describe the sequence of laser energy deposition, plasma formation, ablator expansion, shock generation, and shock propagation through the multilayer target. In addition, the use of tabulated equations of state provides a more realistic description of the material properties, since pressure, internal energy, temperature, and density are no longer constrained by an ideal-gas relation. Finally, the model is no longer restricted to a one-dimensional shock-tube-like configuration, but can be applied to multidimensional geometries. This is particularly relevant for the present experiment, where the target is not purely one-dimensional because of the finite transverse extent of the laser spot and the geometry of the TMPTA foam layer. The same framework also allows different target geometries and material arrangements to be explored.

In this context, the term full-physics does not indicate a complete microscopic description of the laser-matter interaction, but rather refers to the radiation-hydrodynamic HEDP capabilities available in FLASH and used in this work. These capabilities are

distributed among several code units: the Hydro unit performs the three-temperature hydrodynamic update, the EOS unit provides the corresponding material closure, the "HeatExchange" unit accounts for ion-electron equilibration, the "Diffuse" and "Conductivity" units describe electron thermal conduction, the "RadTrans" and "Opacity" units model multi-group radiation diffusion, and the "EnergyDeposition" unit computes the laser energy deposition. The adopted model therefore includes the main macroscopic processes required to describe a laser-driven HEDP experiment within the FLASH framework [11].

However, this full-physics model remains a continuum radiation-hydrodynamic model. The plasma is described in terms of macroscopic fields, such as density, velocity, pressure, internal energy, and separate ion, electron, and radiation temperatures. Kinetic effects, non-Maxwellian particle distributions, microscopic particle acceleration, and kinetic laser-plasma instabilities are not explicitly resolved. Furthermore, the laser propagation and absorption are also treated within a ray-tracing/geometrical-optics approximation, rather than by solving the full electromagnetic wave dynamics. These approximations are acceptable for the present work, which is focused on macroscopic hydrodynamic observables such as shock position, shock velocity, post-shock pressure, temperature, and particle velocity. In addition, the TMPTA foam is represented as a homogeneous material with its average density, so that the internal microstructure of the foam slab is not resolved. This assumption avoids the need to explicitly model the inherently three-dimensional porous morphology of the material and is consistent with the two-dimensional hydrodynamic description adopted in this work.

5.2 Three Temperature Model

Fluid models, such as the one used in FLASH, provide a suitable framework for the present simulation not only because their variables are directly related to the experimental observables, but also because they avoid the complexity of a fully kinetic description. A kinetic treatment would require the evolution of particle distribution functions in phase space, increasing the dimensionality of the problem from physical space to phase space. In contrast, a fluid model describes the system in terms of macroscopic fields, such as density, velocity, pressure and energy. This approach is consistent with the fluid-like behavior of the target materials already assumed in Chapter 2, and it can also be applied to the plasma generated by the laser energy deposition. Indeed, the rapid heating of the ablator produces a dense laser-induced plasma that can be treated as highly collisional, making a fluid description appropriate [18].

In a general plasma fluid description, the ionized nature of the medium and the different response times of electrons and ions can be represented by treating electrons and ions as two coupled fluids. In this case, separate sets of conservation equations are introduced for the electron and ion components, with coupling terms accounting for electron-ion collisions. In Section [9], the fluid equations for a laser-induced plasma are presented under the following assumptions:

- The electron fluid is coupled to the ion fluid through electron-ion collisions, described by a term proportional to $(T_{\text{ele}} - T_{\text{ion}})$.
- The volume force is given only by the electric field in the plasma, $\mathbf{E}$.
- The external source term, denoted by q_L and having dimensions of energy per unit volume per unit time, contributes only to the electron fluid. In other words, the electrons absorb the laser energy.
- Since ions are much heavier than electrons, heat transport is assumed to be carried only by the electrons.
- Ideal gas equations of state are assumed for both fluids.

Apart from the explicit electric-field force and the ideal-gas closure, the same physical ideas are also present in the FLASH HEDP model. However, FLASH does not use a two-fluid hydrodynamic description for the simulations considered in this work. Instead, the three-temperature model is hydrodynamically a single-fluid model: the plasma is described by one mass density, one velocity field, and one momentum equation. The separation between ions and electrons; radiation is introduced only at the level of the energy balance. Therefore, the internal energy is divided into ion, electron, and radiation components, allowing the corresponding temperatures to evolve independently.

The 3T model used in FLASH can therefore be interpreted as a single-fluid plasma model with a multi-temperature treatment of the internal energy [11]. The equations are written as follows:

$$\frac{\partial \rho}{\partial t} + \nabla \cdot (\rho \mathbf{v}) = 0, \tag{5.1}$$

$$\frac{\partial}{\partial t}(\rho \mathbf{v}) + \nabla \cdot (\rho \mathbf{v}\mathbf{v}) + \nabla P_{\text{tot}} = 0, \tag{5.2}$$

$$\frac{\partial}{\partial t}(\rho E_{\text{tot}}) + \nabla \cdot [(\rho E_{\text{tot}} + P_{\text{tot}})\,\mathbf{v}] = Q_{\text{las}} - \nabla \cdot \mathbf{q}, \tag{5.3}$$

$$P_{\text{tot}} = P_{\text{ion}} + P_{\text{ele}} + P_{\text{rad}}, \qquad E_{\text{tot}} = e_{\text{ion}} + e_{\text{ele}} + e_{\text{rad}} + \frac{1}{2}\mathbf{v} \cdot \mathbf{v}, \qquad \mathbf{q} = \mathbf{q}_{\text{ele}} + \mathbf{q}_{\text{rad}}. \tag{5.4}$$

$$\frac{\partial}{\partial t}(\rho e_{\text{ion}}) + \nabla \cdot (\rho e_{\text{ion}} \mathbf{v}) + P_{\text{ion}} \nabla \cdot \mathbf{v} = \rho \frac{c_{v,\text{ele}}}{\tau_{ei}} (T_{\text{ele}} - T_{\text{ion}}), \tag{5.5}$$

$$\frac{\partial}{\partial t}(\rho e_{\text{ele}}) + \nabla \cdot (\rho e_{\text{ele}} \mathbf{v}) + P_{\text{ele}} \nabla \cdot \mathbf{v} = \rho \frac{c_{v,\text{ele}}}{\tau_{ei}} (T_{\text{ion}} - T_{\text{ele}}) - \nabla \cdot \mathbf{q}_{\text{ele}} + Q_{\text{abs}} - Q_{\text{emis}} + Q_{\text{las}}, \tag{5.6}$$

$$\frac{\partial}{\partial t}(\rho e_{\text{rad}}) + \nabla \cdot (\rho e_{\text{rad}} \mathbf{v}) + P_{\text{rad}} \nabla \cdot \mathbf{v} = -\nabla \cdot \mathbf{q}_{\text{rad}} - Q_{\text{abs}} + Q_{\text{emis}}. \tag{5.7}$$

The three temperatures are obtained from the corresponding energy components through the material closures used by the code. In particular, the ion and electron temperatures are determined from the ion and electron internal energies through the equation of state, while the radiation temperature is related to the radiation energy density. Therefore, the separation of e_{ion}, e_{ele}, and e_{rad} allows the model to represent different thermodynamic states for ions, electrons, and radiation within the same hydrodynamic fluid.

The single-temperature limit is recovered when the three components are in instantaneous thermal equilibrium, namely when

$$T_{\text{ion}} = T_{\text{ele}} = T_{\text{rad}}.$$

In that case, the internal energy can be interpreted as a single thermal reservoir. The 3T formulation used here relaxes this assumption and allows the three temperatures to differ during the evolution, which is particularly important in a laser-driven problem where the deposited energy is initially coupled mainly to the electrons and is only subsequently transferred to the other components.

The first three equations, namely mass conservation Eq. 5.1, momentum conservation Eq. 5.2, and total energy conservation Eq. 5.3, correspond to the generalized version of the Euler equations for compressible flow introduced in Subsection 2.2. As in the previous hydrodynamic model, viscous and gravitational forces are neglected, consistently with the inviscid approximation commonly adopted for supersonic flow regimes. Electromagnetic forces acting on the plasma are also not included explicitly in the momentum equation. The laser, which is the only external electromagnetic field applied to the target, is accounted only for its energy deposition. For this reason, it appears as a power density source term, Q_{las}, in the total energy equation and, more specifically, in the electron internal energy equation Eq. 5.6. This reflects the fact that, because of their much smaller mass, electrons are the plasma component that interacts most directly with the laser electromagnetic wave and therefore are assumed to be the only channel for laser energy deposition.

Equation 5.4 shows how the total pressure, total specific energy, and total heat flux are constructed from the ion, electron, and radiation contributions. The total pressure is given by the sum of the ion, electron, and radiation pressures, while the total specific energy includes the three internal energy components plus the kinetic energy of the single hydrodynamic fluid. The heat flux is written as the sum of an electron contribution, $\mathbf{q}_{\text{ele}}$, and a radiation contribution, $\mathbf{q}_{\text{rad}}$. In the present model, these terms represent the macroscopic transport of energy by electron thermal conduction and radiation diffusion, respectively.

The ion internal energy equation, Eq. 5.5, contains only one source term associated with electron-ion thermal equilibration. This term represents the collisional transfer of energy from the hotter electronic part to the colder ionic one and drives the two temperatures toward equilibrium. In the present formulation, the strength of this coupling is determined by the electron specific heat, $c_{v,\text{ele}}$, and by the electron-ion equilibration time, τ_{ei}, which defines the characteristic time scale over which thermal equilibrium between electrons and ions is approached. The same term appears with opposite sign in the electron internal energy equation, Eq. 5.6, ensuring that the energy exchanged between ions and electrons is conserved within the components.

The electron internal energy equation also contains the laser source term Q_{las}, the divergence of the electron heat flux, and the radiation-matter coupling terms. The quantities Q_{abs} and Q_{emis} represent, respectively, the radiative energy absorbed by the electrons

and the radiative energy emitted by them. These terms couple the electron energy balance to the radiation energy equation Eq. 5.7, where they appear with opposite sign. Therefore, radiation absorption acts as a source for the material energy and as a sink for the radiation field, while emission has the opposite effect. In this way, the model accounts for energy exchange between electrons, ions, and radiation while preserving a single-fluid hydrodynamic description.

As in the previous model, the system must be closed by an equation of state. In the present 3T formulation, however, the closure must provide separate thermodynamic relations for the ion and electron components, since their internal energies and pressures are evolved independently. For this reason, the ideal-gas closure is replaced by tabulated equations of state, which are used to obtain the material response of each component consistently with the local density and temperature.

5.3 Laser Energy Deposition

In FLASH, it is assumed that the laser energy is deposited only through the inverse Bremsstrahlung (IB) process [11], which consists of electrons gaining electromagnetic energy from the laser electromagnetic wave while interacting with ions through coulomb collisions. This process is one of the most efficient and common energy absorption mechanisms for not too intense lasers ($I \ll 10^{18} W/cm^2$) and sufficiently long pulses, longer than 1 ns [3]. Therefore, it is well suited to simulate the experimental range considered in this work: pulses between 2 and 9 ns and intensities $3 \times 10^{13}\mathrm{W\,cm^{-2}} < I < 2 \times 10^{14}\mathrm{W\,cm^{-2}}$ [5]. It is also important to notice that, since IB acts on electrons, it is consistent with placing the laser source term only in the electron internal energy equation, Eq. 5.6; the electrons then redistribute this energy to the other components.

The governing equation of the power loss P is an ordinary differential equation:

$$\frac{dP}{dt} = -\nu_{ib}(t)P. \tag{5.8}$$

where ν_{ib} is the IB frequency factor:

$$\nu_{ib} = \frac{n_{\mathrm{ele}}}{n_c}\nu_{ei}. \tag{5.9}$$

By expanding the last term of Eq. 5.9, which is the ion-electron collision frequency, it is possible to identify the main dependencies of IB and therefore of the energy deposition:

$$\nu_{ib} = \frac{n_{\mathrm{ele}}}{n_c}\frac{4}{3}\frac{(2\pi)^{1/2} Z_{\mathrm{ion}} e^4 n_{\mathrm{ele}} \ln\Lambda}{(k_B T_{\mathrm{ele}})^{3/2} m_{\mathrm{ele}}^{1/2}} \propto \frac{n_{\mathrm{ele}}^2(\mathbf{r}) \ln\Lambda(\mathbf{r})}{n_c T_{\mathrm{ele}}^{3/2}(\mathbf{r})} \tag{5.10}$$

In the case of this work, which simulates long laser pulses and intensities for the most part of the order of 10^{14} $\mathrm{W\,cm^{-2}}$, the most relevant parameter is the electron density n_{ele}. Therefore, the laser deposits more energy in denser plasma regions. However, there is a strong limit to this deposition, which is defined by the critical density n_c. In fact, a laser can propagate in a plasma as long as its frequency satisfies $\omega_L > \omega_P$. When these two frequencies become equal, the laser propagation stops and the wave is either reflected back or suddenly absorbed near the critical region [3]. In terms of electron density[9]:

$$n_c = \frac{m_{\mathrm{ele}}\omega_L^2}{4\pi e^2} \tag{5.11}$$

This feature defines two separate regions inside the ablator, as can be seen in Fig. 5.1. The first one is the corona, where the ablator has expanded enough to have an electron density below the critical one. The second one is the energy-transport region, where the deposited energy is converted into ablation pressure and generates the compressive shock wave.

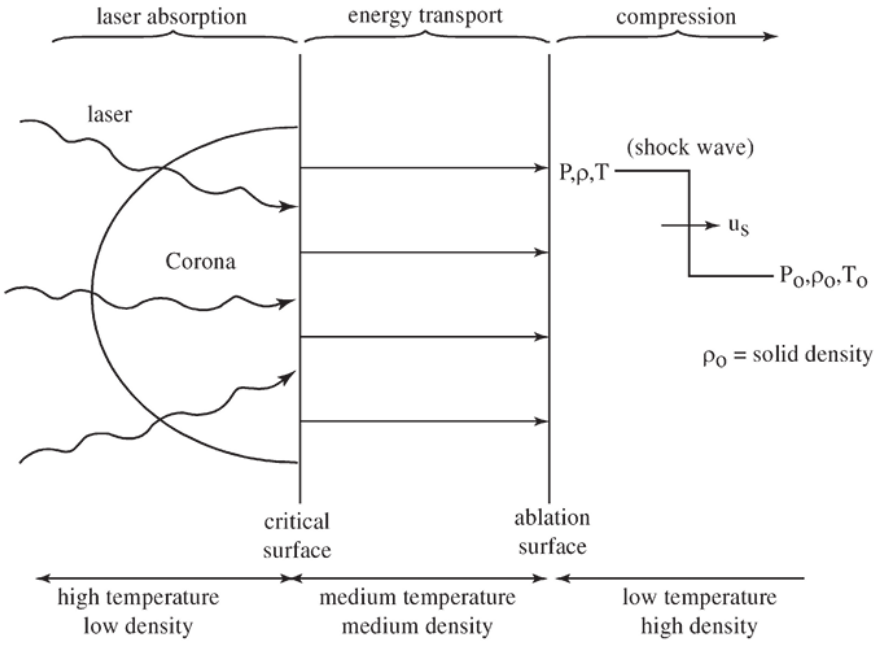

Figure 5.1: Schematic description of laser-plasma interaction from [9].

The critical surface moves toward the laser during the expansion at the same time, the opposite side of the ablator generates the shock wave.

In FLASH, the laser propagation is not handled by resolving the complete electromagnetic field generated by the laser in the previously unmagnetized plasma. Instead, it uses a method called ray tracing, where the laser is divided into many unit-mass rays that travel in a potential field [11]. To each ray is assigned a percentage of the total laser power, and its evolution during the simulation is governed by Eq. 5.8. The potential field is defined as

$$V(r) = \frac{c^2}{2}\eta(r)^2. \tag{5.12}$$

where $\eta(r)$ is the refractive index, which is material dependent and defines, within the geometrical-optics approximation, the trajectory of the ray through each cell, and therefore also the possible refraction and reflection.

The laser source term is finally computed cell by cell from the rays crossing each zone. In each cell, the deposited energy depends on the number of rays passing through the cell and on the time each ray spends inside it, during which Eq. 5.8 is integrated. In this way, the ray-tracing model converts the external laser beam into the volumetric energy source term Q_{las} used in the electron internal energy equation.

5.4 Tabulated Equations of State

To close the 3T model, an equation of state (EOS) is required. In FLASH, the hydrodynamic solver treats a general EOS through two effective thermodynamic indices [11]. The first one is the first adiabatic index,

$$\gamma_1 = \frac{\rho}{P}\left(\frac{\partial P}{\partial \rho}\right)_s, \tag{5.13}$$

which is related to the adiabatic sound speed through

$$c_s^2 = \gamma_1 \frac{P}{\rho}. \tag{5.14}$$

The second one is an effective gamma associated with the local relation between pressure and internal energy,

$$\gamma_e = 1 + \frac{P}{\rho\varepsilon}. \tag{5.15}$$

For a gamma-law ideal gas this quantity coincides with the constant adiabatic index introduced in Eq. 2.14. In the general case, however, these two indices are not necessarily equal and vary with the local thermodynamic state.

These effective indices can be used only to treat the Euler thermodynamic update with a general, non-gamma-law material response. In addition, because the 3T formulation evolves the ion and electron internal energies separately, the material closure must also provide the corresponding thermodynamic relations for the two components. In particular, the ion and electron energy equations require the ion and electron pressures and the relation between internal energy and temperature for each component. The radiation component is not described by the same material-dependent EOS; instead, it follows its own radiative closure, discussed in the radiation transport section.

In this work, the material closure is provided by the SESAME tabulated equation-of-state database of Los Alamos National Laboratory [19]. The use of well-characterized tabulated EOS represents a significant improvement over the ideal-gas gamma-law assumption adopted in the previous model. This improvement is relevant both for the initially solid target materials and for the laser-produced plasma generated during the interaction.

The first improvement concerns the description of solid materials. In an ideal gas, pressure and internal energy are essentially associated with the thermal motion of particles. In a solid or condensed material, instead, the response to compression cannot be described by thermal motion alone. A temperature-independent contribution is also present, associated with the interaction forces between the atoms of the material under compression. This contribution is usually referred to as the cold component of the EOS. When the material is heated, additional thermal contributions arise from the atomic or ionic motion and from the electronic excitations[9]. Therefore, the total pressure and internal energy can be written schematically as

$$\begin{aligned} P(V,T) &= P_c(V) + P_a(V,T) + P_{\mathrm{ele}}(V,T), \\ E(V,T) &= E_c(V) + E_a(V,T) + E_{\mathrm{ele}}(V,T). \end{aligned} \tag{5.16}$$

Here, the subscripts c, a, and ele denote, respectively, the cold component, the atomic or ionic thermal contribution, and the electronic thermal contribution. In shock propagation

through solid targets, the cold component is especially relevant because it accounts for the mechanical response of the compressed atomic structure, which would be absent in a purely ideal-gas description.

The second improvement concerns the description of the laser-produced plasma. The ablated material cannot in general be treated as an ideal plasma over the whole thermodynamic evolution. During the laser-matter interaction, the material can pass through regimes of partial ionization, electronic excitation, strong compression, and non-ideal plasma behavior before complete ionization is reached. In these conditions, pressure and internal energy can vary in a complex way with density and temperature, and a single constant gamma cannot represent the full thermodynamic trajectory.

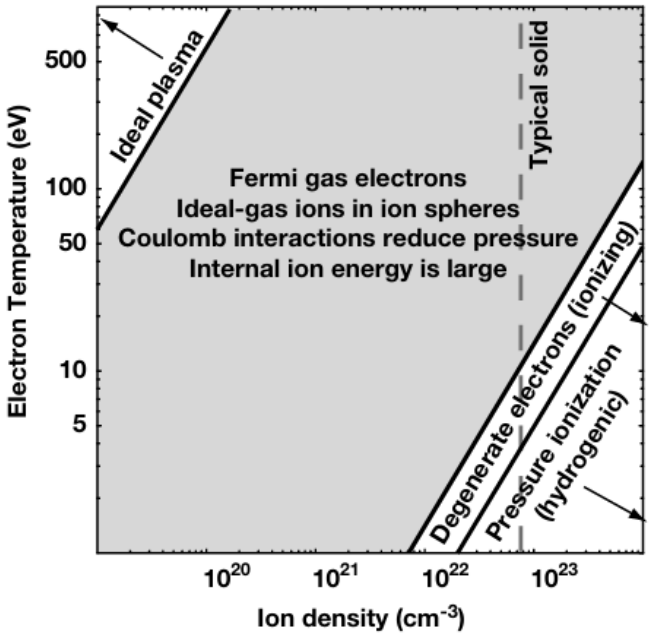

Figure 5.2: Relevant plasma regimes in HEDP [2].

As shown in Fig. 5.2, many HEDP experiments lie in regimes where ideal-plasma assumptions are not sufficient. Below the ideal-plasma region, several additional physical effects may become relevant, including electron degeneracy, strong coupling, partial ionization, and pressure ionization. These effects can be important in strong-shock regimes such as the one investigated in this work. For this reason, the use of a database such as SESAME, based on a combination of physical models and experimental constraints, is crucial to describe not only the plasma generated in the ablator, but also the shock response of the following target materials.

The SESAME data are stored in density-temperature space. In this space, the Helmholtz free energy is tabulated as the thermodynamic potential from which the other thermodynamic quantities can be obtained [16]. A simplified representation of the free-energy model used in SESAME can be written as the sum of cold and thermal contributions:

$$F(\rho, T) = \phi_0(\rho) + F_{\text{nuc}}(\rho, T) + F_{\text{ele}}(\rho, T). \tag{5.17}$$

Here, the three terms represent, respectively, the temperature-independent cold contribution, the nuclear or ionic thermal contribution, and the electronic thermal contribution.

The database is organized into different table series. The material EOS information is contained in the 300 series, with the main tables defined as follows:

301: tables built from the total free energy $F(\rho, T)$.

303: tables built from the cold plus nuclear/ionic contribution, $\phi_0(\rho) + F_{\text{nuc}}(\rho, T)$.

304: tables built from the electronic contribution, $F_{\text{ele}}(\rho, T)$.

305: tables built from the nuclear/ionic contribution, $F_{\text{nuc}}(\rho, T)$.

306: tables built from the cold contribution, $\phi_0(\rho)$.

321: mass-fraction tables defining multiphase regions.

In the present work, only tables 303 and 304 are considered, since these are the tables required by the FLASH implementation used here. Nevertheless, because the Helmholtz free energy is additive, the superposition of these two contributions allows the code to reconstruct the global material response when needed.

This tabulated approach allows FLASH to close both the hydrodynamic part of the 3T model and the ion and electron energy equations, while accounting for the complex thermodynamic behavior that characterizes HEDP regimes. However, this approach also has some limitations. These are mainly related to the level of experimental validation of the thermodynamic region explored during the simulation, to the possible reliance on theoretical models in poorly constrained regions, and to the interpolation procedures used by the code when accessing the tabulated data. In the present work, the most important limitation is the absence of explicit EOS data for porous materials such as foams. As a consequence, the TMPTA foam must be treated as a homogenized material with its average density, as done in this simulation.

5.5 Thermal Coupling and Diffusive Energy Transport

In the 3T formulation introduced above, the equations can be separated into a hydrodynamic part and a set of non-advective energy processes. The left-hand side of the equations contains the hydrodynamic evolution of the fluid, namely the advection of mass, momentum, and energy, together with the compressional work terms appearing in the internal energy equations. This part is responsible for the motion of the material, the compression and expansion of the fluid, and the propagation of shock waves. In FLASH, it is handled by the `Hydro` unit, which evolves the conservative hydrodynamic variables and provides the shock-capturing update of the flow.

The right-hand side of the 3T energy equations contains instead the processes that modify the internal energy distribution without directly advecting mass or momentum. These include electron thermal conduction, radiation diffusion, radiation emission and absorption, laser energy deposition and electron-ion thermal equilibration. The laser source term has already been discussed in the previous section 5.3.

During each time-step, FLASH treats these contributions through an operator-split approach. First, the hydrodynamic update advances the advective part of the problem, giving a new distribution of density, velocity, pressure, and energy. Then, the non-advective processes are applied to this updated state. Laser energy is deposited, electron

thermal conduction redistributes electron energy in space, radiation diffusion transports radiative energy, emission and absorption exchange energy between matter and radiation, and electron-ion equilibration transfers energy locally between the electron and ion components. After these updates, the solution advances to the next time-step.

The radiation component, associated with the third temperature of the model, is relevant in many HEDP experiments and contributes to both the total energy and the total pressure of the system. In some low-density regions, the radiative flux can even become comparable to, or exceed, the material heat fluxes. In general, radiation transport describes the evolution of the radiation intensity I in the phase space $(\mathbf{r}, \nu, t, \mathbf{\Omega})$:

$$\frac{1}{c}\frac{\partial I}{\partial t} + \mathbf{\Omega} \cdot \nabla I + \rho\kappa I = \eta. \tag{5.18}$$

Here, η and κ are, respectively, the emissivity and the total opacity of the material. They account for the gain and loss of intensity at a given point of the radiation phase space, due to emitted, absorbed, and scattered radiation.

As discussed above the advective evolution of the radiative energy is included in the hydrodynamic update, while the remaining non-advective radiation transport and matter-radiation coupling terms are solved separately. In this non-advective radiation update, FLASH does not solve the full transport equation, Eq. 5.18, in terms of the radiation intensity $I(\mathbf{r}, \nu, t, \mathbf{\Omega})$. Instead, it adopts a multi-group diffusion approximation. The frequency dependence is discretized by dividing the photon spectrum into a finite number of energy groups, while the angular dependence is removed by replacing the intensity with the radiation energy density of each group. In this way, the non-advective radiation transport problem is reduced to a set of diffusion equations, one for each radiation energy group. The equation solved for a single group is

$$\frac{1}{c}\frac{\partial u_g}{\partial t} - \nabla \cdot \left(\frac{1}{3\sigma_{t,g}}\nabla u_g\right) + \sigma_{a,g} u_g = \sigma_{e,g} a T_{\text{ele}}^4 \frac{15}{\pi^4}\left[P(x_{g+1}) - P(x_g)\right]. \tag{5.19}$$

Here, u_g is the radiation energy density of a single energy group, $P(x_g)$ is the Planck integral evaluated at the group boundary, and $\sigma_{a,g}$, $\sigma_{e,g}$, and $\sigma_{t,g}$ are the absorption, emission, and transport opacities, respectively [11].

Since the plasma emission is assumed to follow a Planck spectrum, the difference between the two Planck integrals at the group boundaries determines how much of the emitted energy falls inside the energy interval of group g. Therefore, the factor

$$P(x_{g+1}) - P(x_g)$$

represents the fraction of the total emitted radiation assigned to that group.

In Eq. 5.19, the term containing the transport opacity controls the spatial diffusion of the group radiation energy density. It defines the radiative heat flux as the sum of the diffusive fluxes over all groups:

$$\mathbf{q}_{\text{rad}} = \sum_g \left(-\frac{1}{3\sigma_{t,g}}\nabla u_g\right). \tag{5.20}$$

The remaining terms represent absorption and emission. Absorption acts as a sink for the radiation field and as a source for the electron internal energy, while emission acts in the opposite way. These terms therefore provide the coupling between the multi-group radiation equations and the non-advective part of the electron energy equation.

In the multi-group treatment, the radiative contribution to the electron energy is first computed separately for each radiation group and then summed over all groups. The total net source term entering the electron internal energy equation is

$$Q_{\text{abs}} - Q_{\text{emis}} = \sum_g \left\{ \sigma_{a,g} u_g - \sigma_{e,g} a T_{\text{ele}}^4 \frac{15}{\pi^4} \left[P(x_{g+1}) - P(x_g) \right] \right\}. \tag{5.21}$$

In this way, the radiation field is evolved group by group, while the electrons remain a single thermal reservoir. The summed quantity in Eq. 5.21 is the radiative source term that enters the electron energy equation as $Q_{\text{abs}} - Q_{\text{emis}}$.

The resolution of the radiation and electron energy distributions is physically important for laser-induced plasmas that generate shock waves. As shown in Fig. 5.1, beyond the critical density the laser cannot directly propagate and deposit energy into the material. Therefore, the energy deposited in the corona plasma must be transported toward the ablation region, where the ablation pressure responsible for shock formation is generated. This transport is carried both by electrons and by radiation [9]. In highly collisional regions, the electron heat transport range is reduced by electron-ion energy exchange; however, in laser-generated shocks, electron heat transport can still represent a relevant path for energy redistribution.

In fact electrons play a central role in the energy balance of the system: they absorb the laser energy, exchange energy with the radiation field, contribute together with radiation to the diffusive heat flux, and finally transfer part of their energy to the ions through electron-ion equilibration. These last two contributions are solved separately by FLASH in the non-advective update of the electron internal energy equation, in order to compute their contribution to the total specific electronic internal energy.

The diffusive electron heat flux can be modeled in a simple form through Fourier's law:

$$\rho \frac{\partial e_{\text{ele}}}{\partial t} = -\nabla \cdot \mathbf{q}_{\text{ele}} = \nabla \cdot \left(K_{\text{ele}} \nabla T_{\text{ele}} \right). \tag{5.22}$$

It is important to notice that the diffusion approximation for electron heat transport in laser-plasma systems is valid only when the temperature gradient is not too steep. In this case, heat transport is mainly driven by thermal electrons whose distribution is close to Maxwellian, with only a small asymmetry induced by the temperature gradient. This produces a conductive heat flux that tends to restore thermal equilibrium.

This condition is satisfied when the electron mean free path is much smaller than the temperature scale length,

$$\lambda_{\text{ele}} \ll L_T, \qquad L_T = \frac{T_{\text{ele}}}{|\nabla T_{\text{ele}}|},$$

or, more quantitatively, when $\lambda_{\text{ele}}/L_T < 10^{-2}$ [9]. In this regime, most electrons behave as thermal particles and transport heat diffusively, while the fraction of fast electrons able to penetrate deeper into the target and produce non-diffusive heat transport is negligible. In laser-plasma interactions, non-diffusive transport can become important for laser intensities $I_L > 10^{15}\,\text{W}\,\text{cm}^{-2}$ or for laser wavelengths longer than the ultraviolet range [2][9]. In the experiment simulated in this work [5], the diffusive condition is not always fully satisfied. For this reason, FLASH allows the use of a flux limiter, which reduces the conductive heat flux to a fraction f of the free-streaming limit,

$$Q_{\text{FS}} = f n_{\text{ele}} k_B T_{\text{ele}} v_{\text{th}}. \tag{5.23}$$

The last non-advective term is the thermal equilibration between electrons and ions, described by the system

$$\begin{aligned} \frac{\partial e_{\text{ion}}}{\partial t} &= \frac{c_{v,\text{ele}}}{\tau_{ei}} \left(T_{\text{ele}} - T_{\text{ion}} \right), \\ \frac{\partial e_{\text{ele}}}{\partial t} &= \frac{c_{v,\text{ele}}}{\tau_{ei}} \left(T_{\text{ion}} - T_{\text{ele}} \right). \end{aligned} \tag{5.24}$$

Its role is to transfer, on the proper timescale, the energy transported by electrons and radiation, and absorbed by the electrons, to the ions. When this happens, the matter as a whole has acquired part of the laser energy, allowing the mechanical response of the material and the formation of the shock.

The most relevant parameter in this process is the electron-ion equilibration time τ_{ei}, which is the characteristic timescale of the transient [11]. In FLASH, it is expressed as

$$\tau_{ei} = \frac{3 k_B^{3/2}}{8\sqrt{2\pi} e^4} \frac{\left(m_{\text{ion}} T_{\text{ele}} + m_{\text{ele}} T_{\text{ion}} \right)^{3/2}}{\left(m_{\text{ele}} m_{\text{ion}} \right)^{1/2} \bar{z}^{\,2} n_{\text{ion}} \ln \Lambda_{ei}}. \tag{5.25}$$

Different models for this process mainly affect the value of $\ln \Lambda_{ei}$, the Coulomb logarithm associated with electron-ion collisions. This quantity contains information about the maximum and minimum impact parameters of the possible collisions in the system.

Chapter 6

Simulation Setup

6.1 Domain Configuration

The full-physics simulation is designed to reproduce, within a numerical framework, the laser-driven target configuration shown in Fig. 1.1. Since laser irradiation is directly simulated in this case, the setup must not only represent the layered experimental target, but also describe the physical processes leading to shock formation. In particular, laser energy deposition, plasma formation and ablation dynamics have to be included, because they determine the pressure drive that launches the shock. Therefore, the purpose of the computational setup is to follow the generation and propagation of the shock through the quartz reference layer and the TMPTA foam, while also representing the ablated target layers required to generate the shock self-consistently.

The simulation is performed in a two-dimensional Cartesian geometry. The laser propagates along the x-direction, while the y-direction represents the transverse direction of both the target and the laser spot. In order to reduce the computational cost, only the lower half of the transverse domain is simulated. This half-domain approximation exploits the transverse symmetry of the laser irradiation. However, it does not reproduce one geometrical feature of the experimental target, namely the reduced height of the TMPTA slab, which was introduced to allow the VISAR diagnostic to detect the shock also in the quartz reference layer. In the simulation, the TMPTA foam is instead treated as a full-height slab, like the other target layers. This approximation is acceptable for the quantities compared with the experimental data in Ref. [5], since the laser drive generates a shock whose main propagation direction is along x. Therefore, the reduced transverse height of the foam slab is not expected to significantly affect the shock dynamics at the quartz-TMPTA interface in the region considered for the analysis.

The resulting half-domain is defined as

$$x \in [0, 143]\ \mu\text{m}, \qquad y \in [0, 300]\ \mu\text{m},$$

with x corresponding to the laser propagation direction and y to the transverse direction.

The target is represented as a sequence of planar slabs along the x-direction. From left to right, the domain contains a low-density helium region, a CH ablator, a thin gold layer, an α-quartz reference layer and the TMPTA foam sample. Each layer is initialized as a distinct FLASH species, so that a different density and material model can be assigned to each region. The material layout used in the simulation is summarized in Table 6.1.

The internal microstructure of the TMPTA foam is not explicitly resolved. Instead, the foam is homogenized and treated as a continuum material at its average density. This

Region	Material	FLASH species	x-range [μm]	ρ_0 $\left[\frac{\mathrm{g}}{\mathrm{cm}^3}\right]$
Ambient chamber	He	amb	$0-20$	1.0×10^{-3}
Ablator	CH	ch	$20-60$	1.2
Metal layer	Au	au	$60-63$	19.3
Reference layer	α-quartz	quartz	$63-103$	2.65
Foam sample	TMPTA	tmpta	$103-143$	0.26

Table 6.1: Layered material configuration adopted in the FLASH simulation.

approximation avoids introducing very different spatial scales in the same simulation, which would require a multi-scale treatment of both the pore-scale foam structure and the hydrodynamic evolution of the target. For the material description, both the CH ablator and the TMPTA foam are modeled using a polystyrene tabulated material. This choice is motivated by their plastic, hydrocarbon-based composition and by the availability of a polystyrene table in the FLASH database. Their different role in the target is therefore represented mainly through their different initial densities.

The thermodynamic response of the materials is described using SESAME tabulated equations of state, as already introduced in Sec. 5.4. Radiation transport requires opacity information, which is obtained from the tabulated data of the LANL TOPS opacity database. This database provides mixture opacities calculated from ATOMIC or LEDCOP elemental opacity data [20].

Gold is treated differently only for the opacity model. Its thermodynamic response is still described through the tabulated EOS, but constant opacity coefficients are imposed for radiation absorption, emission and transport. This choice was adopted due to the absences of gold in the LANL TOPS opacity database. Since the gold layer is very thin and is not the material of final interest in the post-shock analysis, this approximation provides a controlled treatment of its radiative interaction without introducing additional table-related complications.

The constant gold opacity coefficients used in the simulation are

$$\kappa_{\mathrm{abs}} = 11972\ \frac{\mathrm{cm}^2}{\mathrm{g}}, \qquad \kappa_{\mathrm{emis}} = 11972\ \frac{\mathrm{cm}^2}{\mathrm{g}}, \qquad \kappa_{\mathrm{trans}} = 7434\ \frac{\mathrm{cm}^2}{\mathrm{g}}.$$

The same Planck mean value is used for absorption and emission, while the Rosseland mean value is used for radiative transport [21]. These values were computed for gold at the reference density $\rho_0 = 19.3\,\frac{\mathrm{g}}{\mathrm{cm}^3}$ and at $T = 100\,\mathrm{eV}$, which is the lowest temperature available in the data.

6.2 Initial and Boundary Conditions

The boundary conditions adopted for the hydrodynamic variables, radiation transport and electron thermal conduction are summarized in Table 6.2. The hydrodynamic boundaries are chosen to allow the laser-produced plasma and the resulting waves to leave the domain along the open sides, while preserving the symmetry of the half-domain configuration. The radiation and electron-conduction boundary conditions constrain only the diffusive part of the corresponding energy transport equations, since the advective components are evolved by the hydrodynamic unit, as discussed in Chapter 5.

For radiation transport, vacuum boundary conditions are imposed on the open boundaries. This choice allows radiation energy to leave the computational domain without

Boundary	Hydrodynamics	Radiation transport	Electron conduction
xl ($x = 0$ μm)	Outflow	Vacuum	Neumann
xr ($x = 143$ μm)	Outflow	Vacuum	Neumann
yl ($y = 0$ μm)	Outflow	Vacuum	Neumann
yr ($y = 300$ μm)	Reflecting	Reflecting/Neumann	Neumann

Table 6.2: Boundary conditions used for the hydrodynamic variables, radiation transport and electron thermal conduction [11].

being artificially reflected or re-emitted into the solution. On the symmetry boundary, instead, a zero normal radiative flux is imposed in order to preserve the symmetry of the radiation temperature field. In FLASH this condition can be specified as either reflecting or Neumann for the diffusive radiation variable, since both correspond to the same zero-flux closure in this context.

For electron thermal conduction, Neumann boundary conditions are used. This corresponds to imposing a zero normal temperature gradient, and therefore no conductive heat flux through the boundary. Although this does not represent a truly open thermal boundary, it is less invasive for the present problem than imposing a fixed low temperature through a Dirichlet condition, which would artificially cool the target and introduce a strong numerical heat sink at the domain boundaries.

The ideal physical initial condition corresponds to a target at rest, in thermal and mechanical equilibrium before the arrival of the laser. The ambient region must not perturb the thermodynamic state of the target and should interact only weakly with the incoming rays, in order to avoid a significant depletion of the laser energy before it reaches the target surface. For this reason, the helium chamber is initialized in a low density condition at ambient temperature. The corresponding low pressure gives an initial density $\rho_0 = 1.0 \times 10^{-3}\ \frac{\mathrm{g}}{\mathrm{cm}^3}$, leading to a very low electron density and therefore to a strongly reduced inverse Bremsstrahlung absorption before the target, as quantified by Eq. 5.9.

Mechanical equilibrium is obtained by assigning the same chamber pressure to the target slabs, which are initialized with the material densities listed in Table 6.1. Thermal equilibrium is imposed by setting the electron, ion and radiation temperatures equal to the ambient value.

However, the use of tabulated EOS data introduces an additional numerical constraint. In the cold solid-density region, the EOS tables may return negative pressures and/or internal energies, from which FLASH can compute non-physical wave speeds and eventually causing the simulation to crash. To avoid this issue, the FLASH User Guide recommends using the EOS tables only above a suitable minimum temperature [11]. For this reason, in the present work the initial temperature floor is set to

$$T_0 = T_{\mathrm{ele},0} = T_{\mathrm{ion},0} = T_{\mathrm{rad},0} = 20000\ \mathrm{K} \simeq 1.72\ \mathrm{eV}.$$

Since the pressure is not imposed independently, but is computed by the EOS from the local density and temperature, this numerical initialization produces different initial pressures in the different materials. As a result, the target would no longer be in mechanical equilibrium, and spurious expansion waves could be generated before the arrival of the laser-driven shock wave. To prevent this artificial early-time dynamics, a pressure-offset technique is applied.

This pressure-offset technique consists in subtracting the artificial initial material pressure produced by the increased initialization temperature. The pressure returned by the EOS can be written as

$$P_{\mathrm{EOS}} = P_{\mathrm{sim}} + P_0, \tag{6.1}$$

where P_{EOS} is the material pressure returned by the tabulated EOS for the local values of $\rho(t)$ and $T(t)$, P_{sim} is the effective material pressure used in the simulation, and P_0 is the material-dependent reference pressure to be subtracted.

For each material, P_0 is computed from the EOS output at the initial state, namely from the corresponding values of ρ_0 and T_0. The pressure offsets adopted in the simulation are reported in Table 6.3.

Material	P_0 [GPa]
He ambient	4.25×10^{-2}
CH	31.21
Au	81.32
α-quartz	86.52
TMPTA foam	6.89

Table 6.3: Pressure offsets used to reduce the effective material pressure at initialization.

These values were obtained from the initial-condition plot-file of a simulation performed with the pressure-offset correction turned off. The correction is implemented through a scaling factor λ, which rescales the ion and electron pressure contributions returned by the EOS:

$$\lambda = \frac{\max\left(P_{\mathrm{EOS}} - P_0,\, P_{\mathrm{floor}}\right)}{P_{\mathrm{EOS}}}, \tag{6.2}$$

so that the material pressure used by the hydrodynamic solver becomes

$$P_{\mathrm{sim}} = \lambda P_{\mathrm{EOS}} = \lambda \left(P_{i,\mathrm{EOS}} + P_{e,\mathrm{EOS}}\right). \tag{6.3}$$

The pressure floor $P_{\mathrm{floor}} = 0.1$ Pa is introduced to avoid zero or negative effective material pressures.

The radiation pressure is not included in the offset correction. This choice is justified by the fact that, at the initial temperature used in the simulation, the radiation pressure is negligible compared to the material pressure offsets listed in Table 6.3. Therefore, the radiation pressure is kept unchanged and remains treated as a separate contribution to the total pressure.

6.3 Implementation in FLASH

Starting from the standard FLASH `LaserSlab` example presented in [11], a custom simulation unit is developed within the standard FLASH simulation-tree structure,

`FLASH4.8/source/Simulation/SimulationMain/<setup_folder>`.

Only the files defining the problem-specific setup are modified within the setup directory, while the remaining structure of the `LaserSlab` test problem is conserved. The aim of these modifications is to replace the original chamber-target configuration with a laser-driven, multilayer target representative of the reference experiment. In addition, the EOS wrapper generated during the setup stage is patched to include the pressure-offset correction.

Problem Definition The `Config` file is modified to define the new target, while the required FLASH units for hydrodynamics, diffusion, electron-ion heat exchange and electron thermal conductivity are inherited from the base `LaserSlab` structure.

The original two-material chamber-target description is replaced by a five-species target:

$$\texttt{amb}, \quad \texttt{ch}, \quad \texttt{au}, \quad \texttt{quartz}, \quad \texttt{tmpta}.$$

These species correspond, respectively, to the helium ambient gas, the plastic ablator, the gold layer, the quartz reference layer and the reduced-density TMPTA foam. The corresponding material tables, including EOS and opacity data, are declared in this file. In particular, CH tables are used both for the solid plastic layer and for the reduced-density TMPTA foam, since the foam is treated as a homogeneous material with the same base composition but lower average density.

The geometrical parameters of the multilayer target are also declared in `Config` and stored in `Simulation_data.F90`. The target is defined by the positions of the slab interfaces along the laser-propagation direction:

$$x_{\mathrm{He}}, \quad x_{\mathrm{CH}}, \quad x_{\mathrm{Au}}, \quad x_{\mathrm{quartz}}, \quad x_{\mathrm{TMPTA}},$$

which delimit the helium, CH, gold, quartz and TMPTA regions. Additional parameters define the transverse extent of the computational domain, the transverse extent of the TMPTA foam and the transverse interval of the laser top-hat profile. This parametrization allows the same setup to represent both the half-domain configuration, $y = 0$-$300\,\mu$m, and the full transverse domain, $y = 0$-$600\,\mu$m. In both cases, the TMPTA foam is restricted to $y = 0$-$300\,\mu$m, reproducing the step-like geometrical feature of the experimental target. In the half-domain case, the foam occupies the full simulated transverse extent; in the full-domain case, the region above the foam remains filled by the ambient material.

The file `Simulation_data.F90` is extended to collect the setup-level quantities required by the initialization routines. In addition to the geometrical parameters and material initial states, it defines the internal identifiers used to distinguish gamma-law and tabulated EOS treatments.

Finally, the `Config` file introduces the parameters associated with the pressure-offset initialization. These include a logical switch controlling the activation of the correction, one reference pressure for each material and a minimum effective-pressure floor. These quantities are declared at setup level and later used by the patched EOS wrapper.

Two-Dimensional Multilayer Initialization The initialization of the multilayer target is split between `Simulation_init.F90` and `Simulation_initBlock.F90`. The first routine reads the setup parameters and stores them in the shared variables defined in `Simulation_data.F90`, while the second routine applies this information cell by cell to construct the initial material map.

The main geometrical modification is contained in `Simulation_initBlock.F90`. In the original laser-slab setup, each cell was assigned either to the chamber or to a single target region. In the modified version, the cell-centered coordinates are used to construct the multilayer target map. For each cell, helium is first assigned as the default material. The position along the laser-propagation direction is then compared with the prescribed interface positions in order to identify the corresponding layer: helium ambient, CH ablator, gold, quartz or TMPTA foam. In the TMPTA region, the transverse coordinate is also checked, so that the foam occupies only its prescribed vertical extent.

Once the material region has been identified, the corresponding density and the initial electron, ion and radiation temperatures are assigned independently, consistently with the three-temperature model. The initial velocity field is set to zero. The material composition is initialized through the multi-species framework by assigning a dominant mass fraction to the selected material and a small background fraction to the remaining species. This provides a consistent mapping between the geometrical target regions and the species variables used by the EOS and material-property units.

Material tables and Equation of State Part of the tabulated material data is already available from the original `LaserSlab` example. In particular, the helium and polystyrene IONMIX4 table are maintained and used for the ambient gas, the plastic ablator and the TMPTA foam. The use of the same table for both the solid plastic layer and the foam is consistent with the homogeneous-foam approximation adopted in this work.

Additional tables are required for the gold and quartz layers. These EOS data are obtained from SESAME tables through a pre-processing procedure. First, EOSPAC6 was used to convert the original SESAME ASCII2 files into the standard ASCII representation [22]. The resulting tables are then processed with OPACPLOT2 in order to obtain the IONMIX4 `.cn4` format required by FLASH [23]. During this conversion, the low-temperature portion of the EOS tables below the limit, $T_{\mathrm{min,limit}} = 1.53\,\mathrm{eV}$, is removed. This value is slightly below the minimum temperature used in the simulation, $T_{\mathrm{min,sim}} = 1.72\,\mathrm{eV}$, so that the tabulated range remains consistent with the initial thermodynamic state while still retaining a small safety margin against possible numerical temperature undershoots.

For quartz, the opacity data are taken from TOPS tables and converted separately to the IONMIX4 `.cn4` format using OPACPLOT2. The resulting EOS and opacity tables are included among the material data made available to the FLASH setup.

The pressure-offset correction presented in the previous section is numerically implemented after the FLASH setup stage. Once the setup command has generated the `object` directory, the generated file `Eos_wrapped.F90` is patched before compilation. This file acts as the interface between the block-based storage used by the grid and the vector data structure passed to the EOS unit: it gathers the thermodynamic variables and mass fractions from the selected block region, calls the EOS routine, and then writes the updated quantities back to the grid variables. This correction is applied at this wrapper level, after the EOS has returned the thermodynamic state. In this way, the excess material pressure associated with the finite-temperature tabulated initialization is removed during the EOS update without replacing the underlying tabulated EOS.

Setup Command and Legion Build Configuration After defining the custom setup files, the executable is generated through the FLASH setup command:

```
./setup <directory_setup_folder> \
        -auto -2d -nxb=32 -nyb=16 +hdf5TypeIO\
        species=amb,ch,au,quartz,tmpta +mtmmmt +laser +uhd3t +mgd\
        mgd_meshgroups=6 -site=Legion
```

This command collects the problem-specific setup into a two-dimensional FLASH configuration, includes the laser and multi-temperature physics required by the full-physics model, and fixes the five material species used in the target initialization. The number of

cells per block are also specified at this stage, consistently with the AMR structure used in the simulation.

The option `-site=Legion` selects the machine-specific build configuration stored in

`FLASH4.8/sites/Legion/Makefile.h`.

This file provides the compiler and library paths required on the Legion cluster. In particular, it links the executable against the local MPI, HDF5 [12] and HYPRE [24] installations, which are needed for parallel execution, HDF5-based output and the implicit solvers used by the diffusive physics units.

The `Makefile.h` used for this full-physics configuration differs from the one adopted for the gamma-law simulation, since the additional physics units required by the laser-driven, multi-temperature setup depend on external libraries that were not needed in the purely hydrodynamic case.

6.4 Simulation Parameters

Through the setup procedure briefly discussed in the previous section, the executable `flash4` is generated. As in the gamma-law case, the interaction with this executable is controlled through the runtime parameter file `flash.par`, which is placed in the same run directory. The starting point for this file is again taken from the FLASH `LaserSlab` example, more specifically from the `coldstart_2d_3lasers.par` file, since it already corresponds to a two-dimensional laser-driven run starting from the initial, unperturbed target configuration.

Not all the parameters contained in `flash.par` are discussed here. The following section focuses only on the runtime choices most relevant to the full-physics simulation and not already described in the previous sections.

6.4.1 Physical Parameters

Laser Starting from the laser pulse, the beam is modeled as a single top-hat profile along the transverse y direction at the left boundary. A perfectly sharp top-hat beam is, of course, an idealized representation: in a real laser system, the transition between the uniform central region and the outer low-intensity region is continuous and generally includes a tail-like decay. In the present work, this tail is not represented, for example through a super-Gaussian profile, because no quantitative information on its characteristic length is provided by the reference experiment [5]. Since the transverse extent of the uniform-intensity region is fixed by the experimental geometry, an ideal top-hat profile is preferred in order to preserve the prescribed central intensity without introducing an arbitrary additional tail.

n° pulses	Semi-axis	λ	n° beams	Lens (x, y)	Target (x, y)
1	$100\,\mu$m	$0.527\,\mu$m	1	$(-100\,\mu$m, $200\,\mu$m$)$	$(20\,\mu$m, $200\,\mu$m$)$

Table 6.4: Fixed laser-beam parameters used in the full-physics FLASH simulations.

Table 6.4 reports the laser parameters that are kept fixed for all the shots simulated with the setup used in this work. Since only the half-domain is simulated, only half of the transverse flat-top distribution is included in the computational domain. The

illuminated interval therefore spans $y \in [100, 300]\,\mu$m. The lens position defines where FLASH launches the laser rays, while the target position fixes their initial propagation direction. The lens is placed outside the computational domain so that it is not affected by the evolution of the solution or by the boundary condition imposed at x_l.

For each simulated shot, the laser drive is specified by imposing a time-dependent linear power P_{2D} over the pulse duration Δt. The pulse is always divided into three stages: an initial linear rise, a constant-power plateau and a final linear decay. The rise and decay times are kept fixed at 0.5 ns, while the plateau duration and the peak power are varied according to the desired laser intensity and total injected energy. In `flash.par`, the temporal profile is defined through pairs of runtime parameters, `ed_time_1_*` and `ed_power_1_*`, which specify the time breakpoints and the corresponding linear power values. If two consecutive power values differ, FLASH linearly interpolates the laser power between the two time boundaries.

It is important to note that the experimental laser energy refers to a three-dimensional beam, while this FLASH simulation is performed in two dimensions. Therefore, the experimental laser intensity and pulse duration must be converted into an equivalent two-dimensional power per unit depth. Following the conversion suggested in [11], the three-dimensional peak power is first computed as

$$P_{3D} = I\pi r^2, \tag{6.4}$$

where I is the laser intensity and r is the beam radius. For a pulse with a linear rise and decay of 0.5 ns, the corresponding three-dimensional energy is

$$E_{3D} = P_{3D}\,(\Delta t - 0.5\,\text{ns})\,. \tag{6.5}$$

The equivalent two-dimensional peak power for the full transverse domain is then

$$P_{2D,\text{full}} = \frac{2P_{3D}}{\pi r}, \tag{6.6}$$

and, since only the half-domain is simulated, the power actually imposed in the simulation is

$$P_{2D} = \frac{P_{2D,\text{full}}}{2} = \frac{P_{3D}}{\pi r}. \tag{6.7}$$

Here P_{2D} has units of $\frac{\text{W}}{\text{cm}}$, consistently with the two-dimensional Cartesian geometry.

Two additional laser-deposition parameters are kept fixed in all simulated shots: the number of laser rays and the approximation order used for the electron number density and electron temperature inside each cell.

The first parameter defines the discretization of the beam into rays. Each ray carries a fraction of the total beam power; therefore, increasing the number of rays improves the representation of the continuous transverse intensity distribution. In the present case,

$$\texttt{ed\_numberOfRays\_1} = 4096.$$

For a transverse beam width of 200 μm, the nominal spacing between neighbouring rays is

$$\Delta y_{\text{ray}} = \frac{\text{beam width}}{\texttt{ed\_numberOfRays\_1}} = \frac{200\,\mu\text{m}}{4096} \simeq 4.88 \times 10^{-2}\,\mu\text{m}.$$

This spacing is much smaller than the finest cell width in the transverse direction. As a result, each refined cell is crossed by several laser rays (around 12), reducing discretization effects in the deposited energy distribution.

The second parameter is specified in `flash.par` as

$$\texttt{ed\_gradOrder} = 2.$$

This choice enables a second-order in-cell reconstruction of the laser ray. Recalling Eqs. 5.12 and 5.10, the refractive term can be written as

$$\eta(\mathbf{r}) = 1 - \frac{n_{\text{ele}}(\mathbf{r})}{n_c}. \tag{6.8}$$

A higher-order reconstruction of n_{ele} and T_{ele} inside the cell improves both the evaluation of the refractive-index profile, which affects the ray trajectory, and the inverse-Bremsstrahlung absorption factor, which determines the energy deposited by the ray in the cell [11].

Radiation and Electron Diffusion The radiation parameters mainly define the opacity treatment, through either tabulated or constant coefficients, as discussed previously. They also specify the energy groups used in the multi-group diffusion treatment of the non-advective part of the radiation energy transport equation. As shown by the setup command presented in the previous section, the number of radiation groups is kept equal to that of the base `LaserSlab` problem, namely six groups. The same energy boundaries are also conserved:

$$\left[10^{-1}, 10^{0}, 10^{1}, 10^{2}, 10^{3}, 10^{4}, 10^{5}\right] \text{ eV}.$$

This energy range is expected to cover the radiation spectrum relevant to the laser-driven conditions considered in this work. However, a sensitivity study on this parameter could be useful in future work, in order to assess whether increasing the number of groups, and therefore the computational cost, or reducing the resolved spectral range has a significant effect on the solution.

Since both the radiative and electronic non-advective transport terms are solved under a diffusion approximation, they are both controlled by flux-limited diffusion parameters. For radiation, the relevant runtime parameters are `rt_mgdFlMode` and `rt_mgdFlCoef`; for electron thermal conduction, they are `diff_eleFlMode` and `diff_eleFlCoef`. The values adopted in the simulation are reported in the following table.

	Flux mode	Flux coefficient
Radiation	`fl_harmonic`	1
Electrons	`fl_larsen`	0.06

Table 6.5: Flux limiter modes and coefficients used in the full-physics FLASH simulations.

The parameters reported in Table 6.5 define the functional form and the coefficient used to compute the flux limiter f introduced in Eq. 5.23.Its role is to prevent the diffusion approximation from overestimating the diffusive heat fluxes.

As for the radiation energy groups, these flux-limiter parameters are not changed with respect to the base `LaserSlab` `flash.par`. Nevertheless, they remain important numerical parameters for this class of simulations. Radiation transport and electron heat transport are the main mechanisms by which the laser-deposited energy is redistributed toward the ablation region [9]. Their treatment can therefore influence the formation of the ablation pressure and, consequently, the generation of the shock. A sensitivity analysis on the flux-limiter coefficients, especially in the range of laser intensities and pulse durations considered here, would be useful to quantify this effect.

Hydrodynamic, Heat-Exchange, and EOS Runtime Controls The hydrodynamic and electron-ion heat-exchange runtime controls are also kept consistent with the base `LaserSlab` parameter file. The heat-exchange unit is simply activated through `useHeatexchange = .true.`, without introducing additional problem-specific runtime parameters. For the hydrodynamic evolution, the simulation uses the unsplit hydrodynamic solver selected at setup level, with third-order reconstruction, the `minmod` slope limiter, characteristic limiting, HLLC Riemann solver, artificial viscosity with $c_{\mathrm{visc}} = 0.1$, flattening and hybrid-order control. These choices are retained because they provide a robust shock-capturing configuration for the laser-driven target while avoiding additional tuning of the hydrodynamic solver.

The EOS runtime controls are also mostly kept unchanged with respect to the base setup. The initialization mode is set to `eosModeInit = "dens_temp_gather"`, consistently with the density-temperature initialization used for the tabulated EOS materials. The temperature floor is set to `smallt = 20000.0`, so that the initial thermodynamic state remains safely inside the temperature range of the adopted IONMIX4 tables.

A specific modification is introduced in the Newton-Raphson inversion used by the tabulated EOS. During the evolution, FLASH recovers the temperature from the internal energy obtained at the previous step, so that the tables can be interrogated in density-temperature mode. In the thermodynamic range explored during the simulation, some EOS calls may fail because of non-convergence of this iterative procedure. To improve robustness, the maximum number of Newton-Raphson iterations, controlled by `eos_maxNewton`, is increased from 50 to 200. At the same time, the relative tolerance on the internal energy, controlled by `eos_tolerance`, is relaxed from 10^{-8} to 10^{-7}. These changes are not expected to significantly affect the solution, since the convergence issue is observed only in a limited number of EOS calls and is mainly associated with very small relative ion-energy residuals in localized regions.

6.4.2 Space and Time Discretization

As in the simulations presented in the first part of this work, the computational grid is managed through the `PARAMESH` grid unit with adaptive mesh refinement (AMR).

The initial domain decomposition is defined by

$$N_{\mathrm{block},x} = 2, \qquad N_{\mathrm{block},y} = 4,$$

corresponding to a total of eight parent blocks. Each block contains

$$N_{\mathrm{cells,block}} = \mathrm{nxb} \times \mathrm{nyb} = 32 \times 16 = 512 \text{ cells}.$$

The parameters nxb and nyb are fixed through the setup command presented in Section 6.3, as required by the selected `FIXEDBLOCKSIZE` mode.

The choice nxb = 32 and nyb = 16 provides a finer block-level resolution along the x direction. This is the main direction of shock propagation and also the direction along which the material interfaces are arranged. However, since the transverse extent of the domain is larger,

$$L_y = 300\,\mu\mathrm{m} > L_x = 143\,\mu\mathrm{m},$$

the number of initial blocks along y is increased to four. This choice preserves a sufficient transverse resolution for representing the laser deposited energy distribution, which varies along the y direction, despite the smaller number of cells per block in this direction.

The simulation does not use the coarsest available mesh. To provide an adequate resolution throughout the domain, particularly at the initial material interfaces and during the subsequent hydrodynamic evolution, the minimum refinement level is set to

$$l_{\min} = 3.$$

The AMR capability is then used to further resolve the transient laser-energy-deposition region, which provides the driving mechanism for the shock evolution. The maximum refinement level is therefore set to

$$l_{\max} = 4,$$

and the only refinement variable adopted in the final configuration is `depo`, representing the laser-energy-deposition field. The refinement and de-refinement cut-offs are set to 0.6 and 0.15, respectively.

These thresholds, and therefore the activation of AMR, are based on Löhner's error estimator, which detects the presence of strong local gradients [11]. Therefore refinement is triggered only in regions characterized by sufficiently strong gradients in the laser-energy-deposition field, whereas de-refinement occurs once the corresponding indicator decreases below the lower threshold. The separation between the two cut-off values prevents small, unintended fluctuations from causing repeated refinement and de-refinement of the same blocks. Avoiding such unnecessary changes in the mesh is important because it introduces an additional computational cost that would otherwise reduce the resources available for advancing the simulation in time.

The possibility of driving refinement through hydrodynamic variables, such as pressure, velocity or density, was also investigated. These criteria, however, generally caused most of the domain to reach the maximum refinement level, effectively eliminating the computational advantage of AMR. In particular, no single set of cut-offs was found to adequately distinguish the physically relevant waves from small velocity oscillations that were negligible for the solution but still sufficient to trigger refinement.

Using Eq. 3.8, the cell dimensions associated with the two refinement levels are reported below.

	$l_{\min}$	$l_{\max}$
Δx	$0.56\,\mu$m	$0.28\,\mu$m
Δy	$1.17\,\mu$m	$0.59\,\mu$m

Table 6.6: Cell dimension at the two different refinement levels l

As shown in Table 6.6, a sub-micrometer resolution is maintained along the x direction throughout the entire domain. Consequently, even the $3\,\mu$m-thick gold layer is represented by some computational cells. Along the y direction, a sub-micrometer resolution is reached only where the laser-energy-deposition criterion activates the maximum refinement level. This AMR configuration is intended to capture the main physical features required for a qualitative comparison with the reference experiment, while also allowing the performance of the full-physics model to be assessed without requiring excessively large computational resources.

The computational cost is also strongly affected by the time discretization. To ensure numerical stability, the Courant-Friedrichs-Lewy condition [10] is imposed with

$$\mathrm{CFL} = 0.8,$$

as in the simulations presented in the first part of this work. In the present case, however, the helium heated by the expanding plasma can reach very high velocities u and sound speeds c_s, often making the ambient region the limiting one for the hydrodynamic time-step. The CFL number scales as

$$\mathrm{CFL} \propto \frac{(|u| + c_s)\,\Delta t}{\Delta \ell}, \tag{6.9}$$

where $\Delta\ell$ is the local cell size. Therefore, both the high characteristic velocities in the heated helium and the smaller cells introduced by refinement reduce the admissible time-step. This increases the number of iterations required to cover a given physical time interval and hence the overall computational cost.

Limiting the computational requirements is particularly important because the present model represents a first full-physics implementation in FLASH for this class of experiment. The primary objective is therefore to obtain a mutually compatible implementation of the active physical units and tabulated material properties, and to assess whether their combined response qualitatively reproduces the main features of the reference experiment.

At runtime, the allowed time-step range is defined as

$$\Delta t_{\min} = 1.0 \times 10^{-16}\,\mathrm{s},$$
$$\Delta t_{\max} = 1.0 \times 10^{-11}\,\mathrm{s}.$$

In addition, whenever permitted by the active time-step constraints, the time-step increase between two consecutive iterations is limited to 10% through `tstep_change_factor = 1.10`. This prevents excessively abrupt time-step variations during the evolution.

Chapter 7

Results and Discussion

7.1 Post-Processing Methodology

The simulation outputs are stored in HDF5 format [12] and provide two-dimensional fields for each output time step $dt = 0.1\,\mathrm{ns}$, whereas the reference experiment reports only one post-shock value for each shot for the local flow velocity, shock velocity, temperature, and pressure. Therefore, representative post-shock quantities must be extracted from the two-dimensional simulation results.

For this purpose, the following post-processing methodology is applied. First, a selected region of the two-dimensional domain is averaged to obtain one-dimensional profiles along the x direction. These profiles are then used to identify the position of the leading shock front. Finally, the post-shock value of each variable is obtained by averaging it over a suitably defined post-shock plateau. Since the variables in the region between the shock front and the following rarefaction wave are expected to remain approximately constant, the post-shock values extracted at the different simulation times are subsequently averaged over the entire time interval during which the shock propagates through a given slab. The resulting post-shock local flow velocity, pressure, and temperature for each slab can then be compared with the experimental values reported by Paddock et al [5].

As in the gamma-law analysis 4.1.1, the HDF5 files used in this post-processing stage are processed with the `yt` toolkit[14]. The shock velocity is then calculated from the shock positions and the corresponding times at which the front enters and exits each slab, using Eq. 4.1.

The one-dimensional profiles for each time step are constructed by using a volume-weighted average for the density ρ and mass-weighted averages for the remaining variables, here generically denoted by β:

$$\begin{aligned} \overline{\rho}(x) &= \frac{\sum_i \rho_i \Delta V_i}{\sum_i \Delta V_i}, \\ \overline{\beta}(x) &= \frac{\sum_i \beta_i \rho_i \Delta V_i}{\sum_i \rho_i \Delta V_i}. \end{aligned} \tag{7.1}$$

These sums include the cells contributing to the same position along x within the selected transverse band. The volume associated with each contribution is defined as

$$\Delta V_i = \Delta x_i \, \Delta y_i \, L_z,$$

where Δy_i denotes the portion of the i-th cell contained within the selected transverse band. Since the simulation is two-dimensional and Cartesian, a unit depth $L_z = 1\,\mathrm{cm}$ is assumed in the unresolved z direction; in any case its value does not affect the resulting one-dimensional profiles.

Because the resulting profiles are functions of x, the spatial averaging is performed along the transverse y direction. The position and width of the averaging band must be chosen so as to exclude the portion of the shock front significantly affected by lateral rarefaction waves. Within the unaffected central region, the shock front can be considered approximately planar and the flow can therefore be treated as one-dimensional along x. Consequently, at a given x, the selected cells are expected to belong to the same pre-shock or post-shock region, avoiding the simultaneous averaging of states located on opposite sides of a curved shock front.

For a laser beam with a uniform transverse profile of radius R_L, the radius R_g of the region in which the shock remains approximately one-dimensional can be estimated as [9]

$$R_g \leq R_L - d, \tag{7.2}$$

where d is target depth. Outside this region, lateral rarefaction waves have had sufficient time to reach the shock front, progressively producing the curved shape. The relative positions of the shock front and the lateral rarefaction waves are illustrated in Fig. 7.1.

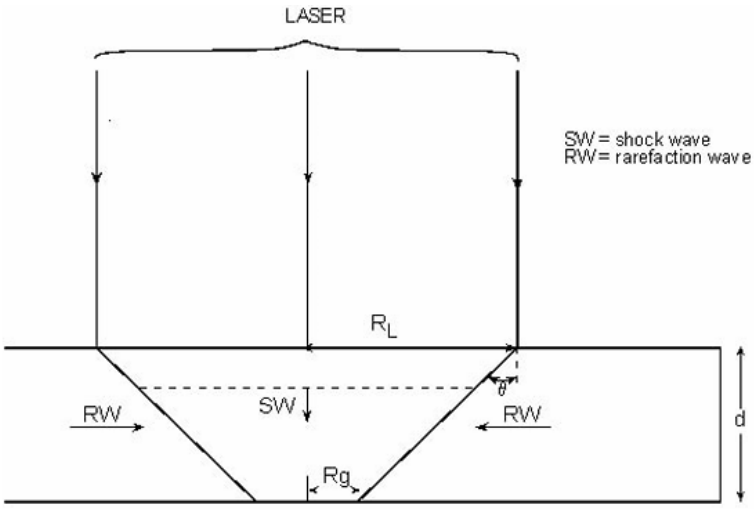

Figure 7.1: Shock front and lateral rarefaction waves produced during the two-dimensional interaction between a laser beam and a target, adapted from [9].

In the present configuration, the most suitable averaging region is therefore located close to the center of the irradiated area. For the two materials of primary interest, Eq. 7.2 gives

$$R_{g,\mathrm{quartz}} \leq R_L - (d_{\mathrm{CH}} + d_{\mathrm{Au}} + d_{\mathrm{quartz}}) = 117\,\mu\mathrm{m},$$
$$R_{g,\mathrm{TMPTA}} \leq R_L - (d_{\mathrm{CH}} + d_{\mathrm{Au}} + d_{\mathrm{quartz}} + d_{\mathrm{TMPTA}}) = 77\,\mu\mathrm{m}.$$

where $R_L = 200\,\mu\mathrm{m}$.

Accordingly, the transverse band adopted for the one-dimensional averaging is

$$y \in [230, 297]\,\mu\text{m}.$$

The center of the irradiated region coincides with the symmetry boundary y_r and is therefore not included directly in the averaging band, in order to reduce any possible influence of the boundary condition. Accordingly, the upper limit of the band is placed below the symmetry boundary by at least two cells at the minimum refinement level, as reported in Table 6.6.

The lower boundary of the averaging band is selected so that its maximum distance from the symmetry axis is $70,\mu$m. This value satisfies the most restrictive one-dimensionality condition, corresponding to the TMPTA slab, while retaining a conservative margin of $7,\mu$m with respect to the limit $R_{g,\text{TMPTA}} = 77,\mu$m. The resulting band has a total width of $67,\mu$m, which also provides a sufficiently large number of transverse samples for the averaging procedure:

$$\frac{\Delta y_{band}}{\Delta y_{l_{\min}}} \approx 57.$$

When a cell intersects only part of the selected band, just the overlapping portion of Δy contributes to its effective averaging volume.

Finally, the longitudinal cell width Δx_i defines the second spatial dimension of the control volume used in Eq. 7.1. To preserve the adaptive structure of the original solution, the cells are associated with their actual AMR intervals along x. Therefore, the resulting one-dimensional profile may retain a non-uniform longitudinal resolution, consistently with the refinement distribution of the original two-dimensional dataset.

The one-dimensional profiles are then used to detect the shock front. The shock of interest is the leading one, since the reference experiment measures the post-shock state of material that was initially unperturbed.

Density, pressure, and longitudinal velocity are all possible candidates for shock detection. The temperatures are less suitable in the present 3T model because electron thermal conduction and radiation transport may produce preheating ahead of the hydrodynamic shock, potentially leading to false detections. In this work, pressure is selected as the shock-detection variable because it is directly related to the compressive wave generated in the target by the ablation process. Moreover, unlike density, pressure does not exhibit initial discontinuities at the interfaces between different materials, thereby reducing the risk of identifying a material interface as a shock.

The pressure profile $P(x)$ is therefore analyzed at each output time, and its spatial derivative $\frac{\partial P}{\partial x}$ is computed. The shock-detection criterion is defined as

$$\frac{\partial P}{\partial x} \leq -G_s < 0, \tag{7.3}$$

where G_s is the minimum pressure decrease per unit length required for a region to be identified as a shock front. A negative pressure gradient is considered because the shock propagates from the left boundary x_l toward increasing x: when the profile is examined from left to right, the pressure decreases from the high-pressure post-shock state to the lower-pressure unperturbed state.

The points satisfying Eq. 7.3 are grouped into contiguous regions. Since the shock of interest is the leading one, the rightmost qualifying region is selected and identified as the numerical shock-front interval $[x_{s,L}, x_{s,R}]$. The shock position at each output time is then defined as the midpoint of this interval:

$$x_s = \frac{x_{s,L} + x_{s,R}}{2}.$$

Repeating this procedure for all the available output times makes it possible to reconstruct the evolution of the shock position, $x_s(t)$. The mean shock velocity within each slab can then be evaluated using Eq. 4.1.

Given the shock position as a function of time and the corresponding one-dimensional profiles, a representative post-shock value for each slab can be obtained by identifying its plateau. This represents the approximately uniform region located between the shock front and the following rarefaction wave, within which the post-shock state is established.

For each variable of interest β, the corresponding one-dimensional profile is analyzed from the shock position x_s toward decreasing x. Since the different variables may approach a nearly uniform post-shock state over slightly different spatial intervals, an independent averaging region is identified for each quantity. A cell i is considered part of this region when it satisfies the following condition:

$$\begin{aligned} \frac{\left|\frac{\partial \beta}{\partial x}\right|_i}{G_{\mathrm{s},\beta}} &\leq G_p, \\ G_{\mathrm{s},\beta} &= \frac{|\beta_{\mathrm{s,R}} - \beta_{\mathrm{s,L}}|}{x_{\mathrm{s,R}} - x_{\mathrm{s,L}}}. \end{aligned} \tag{7.4}$$

Here, $G_{\mathrm{s},\beta}$ is the average gradient of the variable β across the numerical shock front, whose boundaries were previously identified using the shock-detection criterion in Eq. 7.3. The quantities $\beta_{\mathrm{s,L}}$ and $\beta_{\mathrm{s,R}}$ are the values of the considered variable at the left and right boundaries of the front, respectively. Normalizing the local gradient by the average gradient across the shock makes the criterion dependent on the magnitude of the discontinuity for each variable. Consequently, a larger absolute gradient may be accepted when the shock jump is stronger, whereas a weaker discontinuity results in a more restrictive absolute tolerance. This formulation also allows small residual oscillations to be retained within the selected region and subsequently averaged.

The first continuous interval $[x_{L,p}, x_{R,p}]$ satisfying Eq. 7.4 behind the numerical shock front is regarded as a candidate post-shock region. Additional geometrical and uniformity requirements are then applied to prevent unrelated nearly uniform portions of the profile from being incorrectly selected.

First, to exclude regions located too far behind the shock to represent the immediate post-shock state, the distance between the cell containing the shock position and the closest boundary of the candidate interval must satisfy

$$i_s - i_{R,p} \leq N_s = 5, \tag{7.5}$$

where N_s is the maximum allowed number of cells between the shock-position cell i_s and the rightmost cell of the selected interval, $i_{R,p}$. Expressing this requirement in terms of cells rather than as a fixed physical distance makes it more suitable for the AMR mesh adopted in the simulation. In particular, the corresponding maximum physical separation decreases in more highly refined regions, making the condition locally more restrictive.

The spatial extension of the candidate interval is also constrained. It must contain at least two complete AMR cells,

$$N_{p,cells} \geq N_{p,min} = 2.$$

This prevents a single numerical value from being interpreted as a representative spatial average.

A maximum extension is also imposed to prevent an excessively permissive value of G_p in Eq. 7.4 from producing an unrealistically long averaging region:

$$L_p \leq 5\ \mu\text{m}.$$

If the initially detected continuous interval exceeds this limit, complete cells are progressively removed from its left boundary, namely from the side farthest from the shock. The portion closest to the shock is therefore retained. If this reduction leaves fewer than two cells, the candidate is rejected. At the finest longitudinal resolution used in the simulations, the maximum allowed extension corresponds approximately to

$$\frac{L_p}{\Delta x_{\text{cell}}} \approx 9 \text{ cells}$$

Finally, to avoid contamination from the transition between two materials when the shock has only recently entered a new slab, the final interval used for the average must not intersect the entrance interface:

$$x_{L,p} > x_{\text{interface}}.$$

The initially detected low-gradient region may extend across the interface if its length exceeds the maximum permitted value. The interface condition is therefore evaluated only after the interval has been reduced to retain the portion closest to the shock.

From these geometrical conditions, the penetration depth associated with an acceptable post-shock region can be expressed as

$$d_{\text{slab}} = L_p + d_s, \tag{7.6}$$

where d_s is the distance between the shock and the boundary of the selected region closest to it. Therefore, d_{slab} represents the resulting penetration that the shock must reach inside the slab for a sufficiently extended averaging interval to be available without crossing the entrance interface.

Once the interval $[x_{L,p}, x_{R,p}]$ has been identified, together with its actual length $L_{p,\text{slab}}$, the instantaneous post-shock value of the variable in the considered slab, $\overline{\beta}_{\text{slab}}(t)$, is calculated as a spatial average:

$$\overline{\beta}_{\text{slab}}(t) = \frac{\sum_i \beta_i \Delta x_{i,p}}{L_{p,\text{slab}}}, \tag{7.7}$$

where $\Delta x_{i,p}$ is the width of the i-th complete AMR cell included in the averaging interval and $L_{p,\text{slab}} = \sum_i \Delta x_{i,p}$ is its total length.

After computing $\overline{\beta}_{\text{slab}}(t)$, a final check is performed on the overall excursion of the variable:

$$R_{\beta,\text{p}} = \frac{|\beta_{\text{slab,p,max}} - \beta_{\text{slab,p,min}}|}{|\overline{\beta}_{\text{slab}}(t)|} \tag{7.8}$$

This criterion verifies that the total relative variation across the selected region remains acceptable. It complements the local-gradient condition by detecting, for example, a gradual monotonic increase or decrease that may satisfy Eq. 7.4 in every individual cell

while still producing an excessive overall excursion. If this requirement is not satisfied, the instantaneous value is rejected.

Repeating this procedure at all valid output times provides the temporal evolution of the post-shock variable while the shock propagates through the slab. A single representative value to be compared with the reference experiment is then obtained as

$$\overline{\beta}_{\mathrm{slab}} = \frac{\sum_{i=1}^{N_{\beta,\mathrm{slab}}} \overline{\beta}_{\mathrm{slab}}(t_i)}{N_{\beta,\mathrm{slab}}}, \tag{7.9}$$

where $N_{\beta,\mathrm{slab}}$ is the number of output times for which a valid averaging interval is identified for the considered variable while the shock is located inside the slab. This is an arithmetic average of the valid instantaneous values; therefore, each accepted output time is assigned the same weight, independently of the temporal separation between consecutive profiles.

Criterion	ρ	u_x	P	T_{ele}	T_{ion}	T_{rad}
G_p	0.10	0.10	0.10	0.05	0.05	0.05
$R_{\beta,\mathrm{p,max}}$	0.30	0.30	0.30	0.15	0.15	0.15

Table 7.1: Threshold values used for the normalized-gradient and relative-range criteria.

Table 7.1 summarizes the two criteria that depend on the considered variable rather than being common to all quantities. The same threshold values are used in quartz and TMPTA. They were selected to retain a sufficient number of valid output times and an adequate number of cells for the spatial averaging procedure, while still excluding regions that are not sufficiently uniform. The hydrodynamic variables are assigned less restrictive thresholds because, at some output times, the rarefaction wave approaches the shock front. More restrictive values would therefore prevent the construction of the sufficiently well-defined temporal distribution presented in the following section, ultimately leading to a poorly representative time-averaged value for comparison with the reference experiment.

7.2 Comparison with Reference Experiment

Six simulations were performed for comparison with the reference experimental results. Each case was designed to introduce a total laser energy between 300 J and 700 J, using intensities ranging from 3×10^{13} to 2×10^{14} W cm^{-2} and pulse durations between 2 and 9 ns, consistently with the ranges adopted in the reference experiment [5]. In all cases, the laser pulse was characterized by rise and decay times of 0.5 ns, matching the experimental configuration.

The fraction of laser energy deposited within the computational domain is calculated as

$$f_{\mathrm{dep}} = \frac{E_{\mathrm{in}}(t_{\mathrm{end}}) - E_{\mathrm{out}}(t_{\mathrm{end}})}{E_{\mathrm{in}}(t_{\mathrm{end}})} \times 100.$$

As shown in Table 7.2, not all the energy introduced during the laser pulse is deposited within the computational domain. Part of it is reflected or redirected outside the domain through the outflow boundaries. This behaviour depends on the optical properties of the helium ambient and of the ablating target surface, which determine the spatial distribution of the refractive index $\eta(\mathbf{r})$ and, consequently, the laser-ray trajectories described by Equation 5.12 [11].

$I\left[\frac{\mathrm{W}}{\mathrm{cm}^2}\right]$	$\Delta t_{\mathrm{plateau}}$ [ns]	$E_{\mathrm{in}}(t_{\mathrm{end}})$ [J]	$E_{\mathrm{out}}(t_{\mathrm{end}})$ [J]	f_{dep} [%]	$U_s\left[\frac{\mathrm{km}}{\mathrm{s}}\right]$
4×10^{13}	7	376.80	16.30	95.67	24.76
6×10^{13}	5.5	452.16	53.06	88.26	26.33
8×10^{13}	2.5	301.44	83.88	72.17	28.14
1.1×10^{14}	4.5	697.08	175.55	74.81	29.22
1.5×10^{14}	1.5	376.78	168.91	55.17	29.22
1.8×10^{14}	2	565.2	263.00	53.47	29.22

Table 7.2: Laser pulse parameters, energy entering and leaving the computational domain, deposited-energy fraction, and shock velocity for the simulations considered in the comparison with the experimental results.

The deposited fraction does not correspond entirely to the energy absorbed at the ablation surface and therefore available for driving the shock. A portion is spuriously deposited in the helium ambient, as discussed in Section 6.2. Furthermore, the analysis focuses on the leading shock, which propagates into the initially unperturbed material and is generated during the early stage of the laser drive. Its strength is therefore expected to depend more strongly on the laser intensity, which controls the initial ablation pressure, than on the total energy deposited over the complete pulse duration.

Laser intensity I and total input energy $E_{\mathrm{in}}(t_{\mathrm{end}})$ cannot be used to establish a direct correspondence between the simulated and experimental cases. As previously discussed, Paddock et al. report only the overall ranges of laser intensity, pulse duration, and energy employed during the experimental campaign, without specifying the parameters associated with each individual shot.

A qualitative connection can nevertheless be established between the laser intensity and the shock velocity. The experimental scaling

$$P_a \propto I^{0.8}$$

relates the ablation pressure P_a, generated by the expansion of the laser-produced plasma, to the incident laser intensity I [9]. As a first-order approximation, the ablation pressure can be regarded as setting the pressure level that drives the shock through the target. Assuming that this pressure is comparable to the post-shock pressure reached in quartz, the Rayleigh-line relation in Equation (2.13), together with the strong-shock approximation $P_1 \approx 0$, gives

$$\rho_1 U_{s,\mathrm{quartz}} u_{p,\mathrm{quartz}} \propto I^{0.8}. \tag{7.10}$$

The results reported in Table 7.2 show the same qualitative tendency, with larger laser intensities generally producing higher shock velocities in quartz.

For condensed materials, the shock velocity U_s and the post-shock particle velocity u_p are commonly related through the linear expression

$$U_s = c_0 + \alpha u_p, \tag{7.11}$$

where c_0 is the bulk sound speed under standard conditions and α is a material-dependent constant [9]. Therefore, an increase in U_s is also associated with a larger particle velocity and, through the Rayleigh line, with a higher post-shock pressure.

The same reasoning can be extended to the increase in internal energy across the shock. Using the Hugoniot relation in Equation (2.8) and assuming strong shock $P_1,\ e_1 \approx 0$, the following equation is obtained

$$e_2 = \frac{1}{2}\left(\frac{1}{\rho_1} - \frac{1}{\rho_2}\right) P_2 \propto \frac{1}{2}\left(\frac{1}{\rho_1} - \frac{1}{\rho_2}\right) \rho_1 U_s u_p. \tag{7.12}$$

Since u_p increases with U_s, a higher shock velocity corresponds to a larger increase in internal energy and, consequently, to a higher post-shock temperature, although the precise relation depends on the material equation of state.

These relations show that the quantities considered in the experimental comparison can all be interpreted in relation to the shock velocity in quartz. Moreover, $U_{s,\text{quartz}}$ provides an indirect measure of the effective strength of the laser-driven leading shock, which is primarily controlled by the laser intensity during the initial stage of the drive.

For these reasons, the quartz shock velocity $U_{s,\text{quartz}}$ is adopted as the independent variable of the comparison. This choice allows the thermofluid-dynamic response of quartz and TMPTA foam to be evaluated as a function of the effective strength of the shock propagating through the quartz layer.

The quartz shock velocities obtained in all the simulations, as shown in Table 7.2, exceed the range measured by Paddock et al. [5]. Consequently, the numerical cases cannot be directly associated with individual experimental shots, and their quantitative agreement with the experimental data cannot be assessed at corresponding values of $U_{s,\text{quartz}}$.

This systematic overestimation may indicate that the simulated laser drive generates stronger shocks than those represented in the available experimental dataset. However, it may also be influenced by the imposed initial temperature, $T_0 = 1.72\,\text{eV}$. In particular, this choice modifies the initial thermodynamic state of the CH ablator and may therefore affect shock generation. It also alters the initial conditions of the gold and quartz layers, potentially influencing shock transmission and the resulting propagation velocity. Indeed, as discussed in Section 2.2, the shock velocity is constrained by the Rankine-Hugoniot relations, which connect the post-shock state to the corresponding pre-shock conditions. In the simulations, these initial conditions do not correspond to ambient temperature, as is instead expected for the reference experiment.

The comparison is therefore reformulated to assess whether the simulations reproduce at least the experimentally observed relationships between the quartz shock velocity and the other post-shock quantities. Since the simulated values of $U_{s,\text{quartz}}$ lie outside the experimental interval, the analysis necessarily relies on an extrapolation of the trends derived from the experimental data. The results must therefore be interpreted as an evaluation of the consistency of the simulated material response with the continuation of these trends, rather than as a direct quantitative validation against specific experimental shots.

7.2.1 Quartz Post-Shock Quantities

Because only a limited number of experimental points is available for each quantity, all datasets are represented using linear trends. Higher-order polynomials may reduce the residuals within the measured interval, but their curvature would be poorly constrained and could lead to unreliable extrapolations beyond the experimental range.

The root mean square error (RMSE) is used to quantify how closely each linear fit reproduces the experimental central values:

$$\mathrm{RMSE} = \sqrt{\frac{1}{N_{\mathrm{exp}}} \sum_{i=1}^{N_{\mathrm{exp}}} \left[\beta_{\mathrm{exp},i} - \beta_{\mathrm{trend}}\left(U_{s,\mathrm{quartz},i}\right)\right]^2}.$$

The consistency of the simulations with the extrapolated experimental relations is assessed through their relative deviations from the corresponding trend values, using Eq. (4.7). A deviation of 10% is adopted as a practical threshold for good agreement. A dataset is therefore considered well reproduced when all, or nearly all, simulated points remain within this limit.

Pressure The post-shock pressure in quartz, shown in Figure 7.2, is compared with the linear relation

$$P_{\mathrm{quartz}} = 52.806\, U_{s,\mathrm{quartz}} - 445.94,$$

where P_{quartz} is expressed in GPa and $U_{s,\mathrm{quartz}}$ in $\frac{\mathrm{km}}{\mathrm{s}}$.

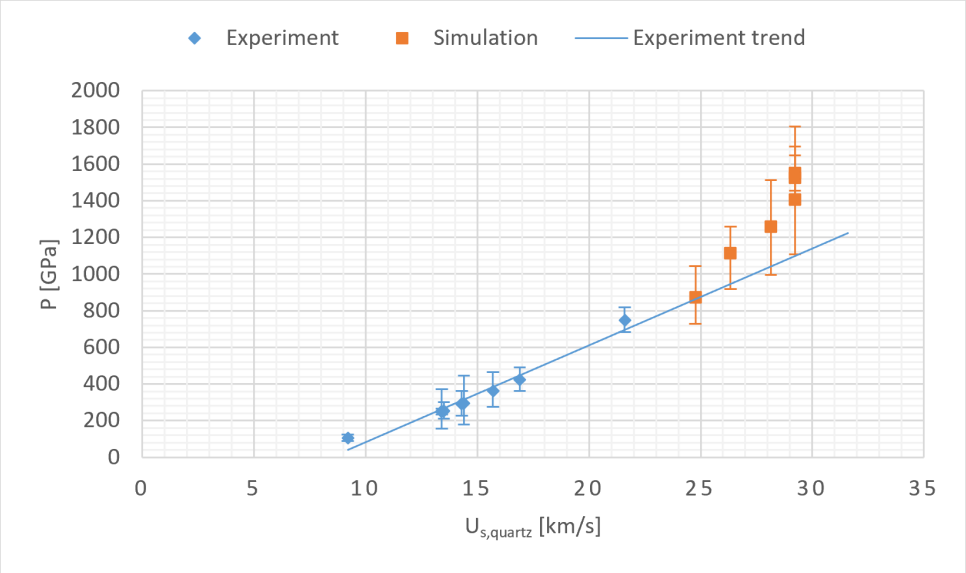

Figure 7.2: Post-shock pressure in quartz as a function of the quartz shock velocity. The experimental values reported by Paddock et al. [5] are shown with their uncertainties, while the simulated points represent the time-averaged post-shock pressures and their temporal dispersion. The linear trend fitted to the experimental data is extrapolated over the range covered by the simulations.

The fit gives RMSE = 32 GPa. The maximum relative deviation between the extrapolated relation and the numerical results is $\varepsilon_{\mathrm{max}} = 41.4\%$. Only the simulated point at $U_{s,\mathrm{quartz}} = 24.76\,\frac{\mathrm{km}}{\mathrm{s}}$ remains within the 10% threshold, whereas the other five cases exceed it. The simulations therefore reproduce the increase in pressure with quartz shock velocity only qualitatively, while their quantitative agreement with the experimental linear trend is limited.

Flow Velocity The post-shock particle velocity in quartz, shown in Figure 7.3, is compared with

$$u_{p,\text{quartz}} = 0.7145\, U_{s,\text{quartz}} - 2.5006,$$

where both $u_{p,\text{quartz}}$ and $U_{s,\text{quartz}}$ are expressed in $\frac{\text{km}}{\text{s}}$.

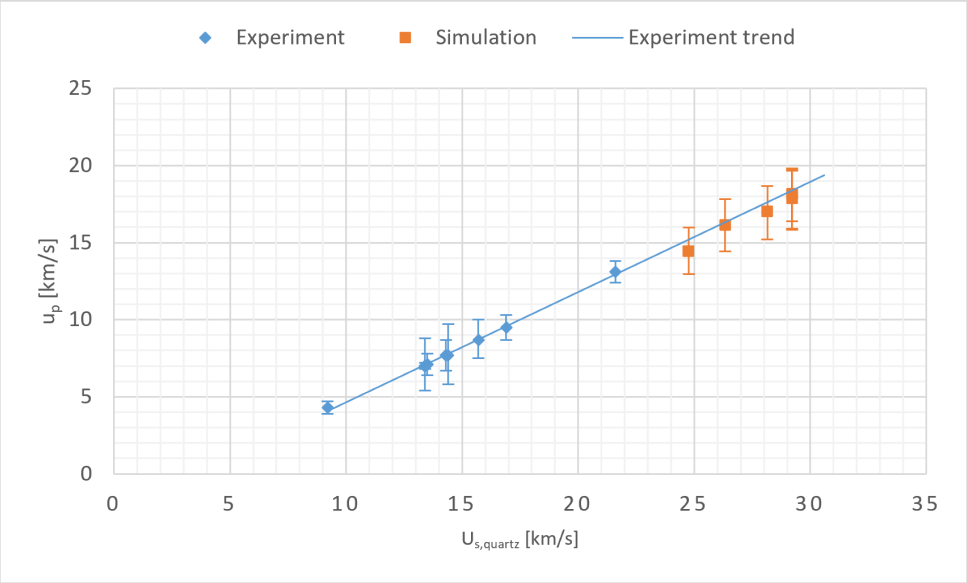

Figure 7.3: Post-shock particle velocity in quartz as a function of the quartz shock velocity. The experimental values reported by Paddock et al. [5] are shown with their uncertainties, while the simulated points represent the time-averaged post-shock particle velocities and their temporal dispersion. The linear trend fitted to the experimental data is extrapolated over the range covered by the simulations.

For this quantity, the linear fit yields RMSE $= 0.10875\,\frac{\text{km}}{\text{s}}$. The largest relative deviation is only $\varepsilon_{\max} = 4.90\%$, and all six simulated values remain within 10% of the extrapolated relation. The numerical results therefore show excellent agreement with the experimental particle-velocity trend.

Temperature The post-shock temperature in quartz, shown in Figure 7.4, is compared with

$$T_{\text{quartz}} = 0.3235\, U_{s,\text{quartz}} - 3.4641,$$

where T_{quartz} is expressed in eV and $U_{s,\text{quartz}}$ in $\frac{\text{km}}{\text{s}}$.

The corresponding RMSE is RMSE $= 0.1077\,\text{eV}$, indicating that the linear relation closely represents the six experimental central values within the measured interval. Its extrapolation, however, shows poor consistency with the simulations. The maximum relative deviation reaches $\varepsilon_{\max} = 34.7\%$, and all six numerical temperatures lie outside the adopted 10% threshold.

The low RMSE and the large simulation-to-trend deviations describe two different aspects of the comparison. The former concerns the representation of the available measurements, whereas the latter shows that the simulated temperatures do not follow their linear extrapolation. The agreement with the experimental temperature trend must therefore be regarded as poor. This result should nevertheless be interpreted considering that

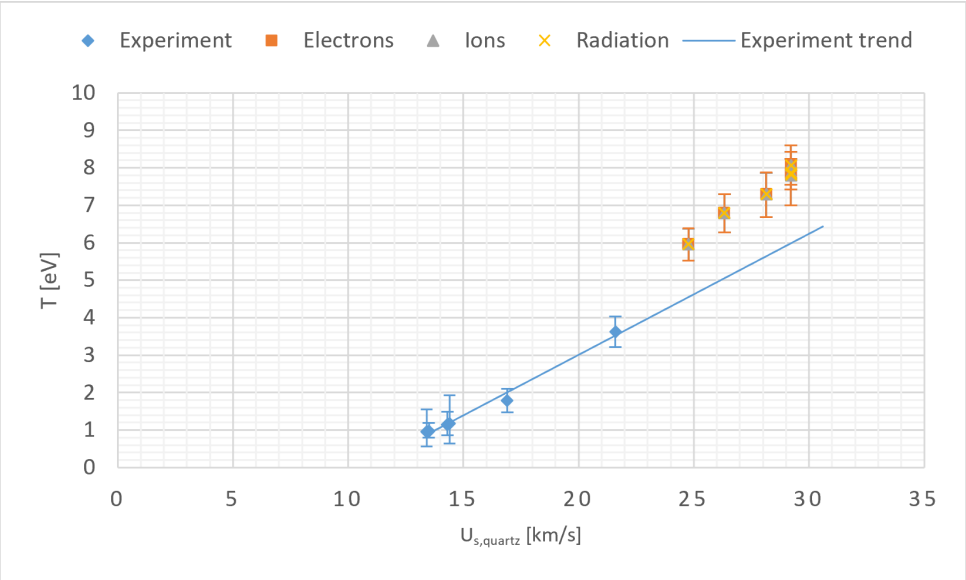

Figure 7.4: Post-shock temperature in quartz as a function of the quartz shock velocity. The experimental values reported by Paddock et al. [5] are shown with their uncertainties, while the simulated points represent the time-averaged electron, ion, and radiation temperatures and their temporal dispersion. The linear trend fitted to the experimental data is extrapolated over the range covered by the simulations.

only six temperature measurements are available and that the SOP diagnostic is affected by considerable uncertainty. In particular, the diagnostic was not absolutely calibrated, and the inferred values depend on the relations adopted for quartz temperature and reflectivity [5].

Finally, the electron, ion, and radiation temperatures are nearly coincident in all the simulated cases, as shown by the overlapping points in Figure 7.4. A separate analysis of the three components is therefore unnecessary. The quartz is not directly heated or ablated by the laser, and the temperature increase in the selected region is primarily produced by shock compression. The post-shock state is consequently close to thermal equilibrium, with $T_\mathrm{e} \simeq T_\mathrm{i} \simeq T_\mathrm{r}$.

7.2.2 TMPTA Post-Shock Quantities

Pressure The post-shock pressure in the TMPTA foam, shown in Figure 7.5, is compared with

$$P_\mathrm{TMPTA} = 8.2612\, U_{s,\mathrm{quartz}} - 61.432,$$

where P_TMPTA is expressed in GPa and $U_{s,\mathrm{quartz}}$ in $\frac{\mathrm{km}}{\mathrm{s}}$.

The fit gives RMSE $= 8.0937\,\mathrm{GPa}$. Most of the simulated pressure values lie below its extrapolation. The maximum relative deviation is $\varepsilon_\mathrm{max} = 18.1\%$, corresponding to the point at $U_{s,\mathrm{quartz}} = 24.76\,\frac{\mathrm{km}}{\mathrm{s}}$. This is the only case outside the 10% threshold, while the remaining five results satisfy the adopted criterion.

The simulations therefore show overall good agreement with the experimental pressure trend in the TMPTA foam, although the correspondence is not uniform because of the larger deviation associated with the lowest simulated quartz shock velocity.

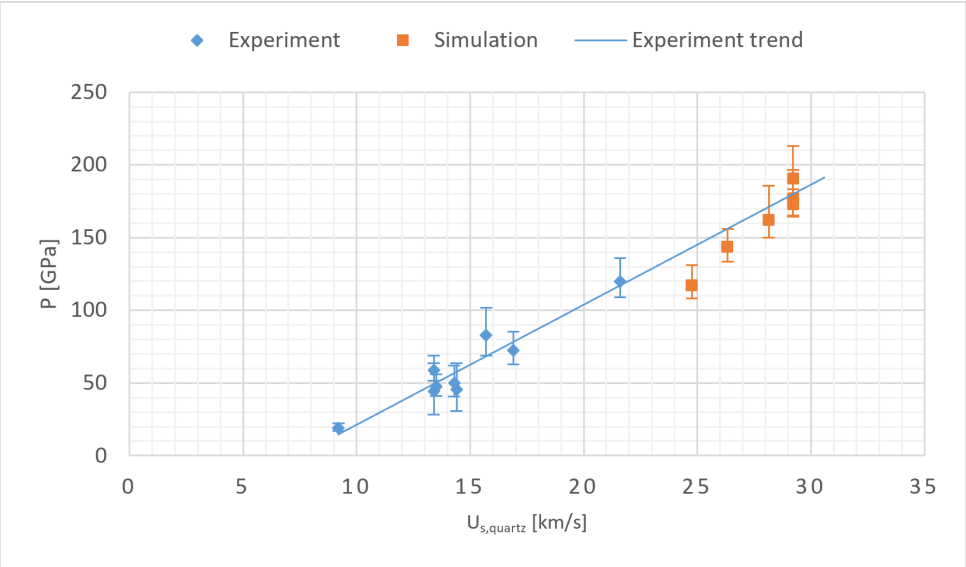

Figure 7.5: Post-shock pressure in the TMPTA foam as a function of the quartz shock velocity. The experimental values reported by Paddock et al. [5] are shown with their uncertainties, while the simulated points represent the time-averaged post-shock pressures and their temporal dispersion. The linear trend fitted to the experimental data is extrapolated over the range covered by the simulations.

Flow Velocity The post-shock particle velocity in the TMPTA foam, shown in Figure 7.6, is compared with the linear relation

$$u_{p,\mathrm{TMPTA}} = 1.1713\, U_{s,\mathrm{quartz}} - 4.6416,$$

where both $u_{p,\mathrm{TMPTA}}$ and $U_{s,\mathrm{quartz}}$ are expressed in $\frac{\mathrm{km}}{\mathrm{s}}$.

The linear fit gives RMSE $= 0.436\,\frac{\mathrm{km}}{\mathrm{s}}$. The simulated particle velocities systematically underestimate the values predicted by its extrapolation, with a maximum relative deviation of $\varepsilon_{\max} = 18.7\%$. Since all six numerical results lie outside the adopted 10% threshold, the quantitative agreement with the experimental trend is poor. Nevertheless, the simulations qualitatively reproduce the increase in the TMPTA particle velocity with increasing $U_{s,\mathrm{quartz}}$.

Temperature The post-shock temperature in the TMPTA foam, shown in Figure 7.7, is compared with the linear relation

$$T_{\mathrm{TMPTA}} = 0.1095\, U_{s,\mathrm{quartz}} - 0.8331,$$

where T_{TMPTA} is expressed in eV and $U_{s,\mathrm{quartz}}$ in $\frac{\mathrm{km}}{\mathrm{s}}$.

The linear fit gives RMSE $= 0.124\,\mathrm{eV}$, indicating that it closely represents the experimental central values within the measured interval. Its extrapolation, however, is completely inconsistent with the simulated temperatures. The maximum relative deviation reaches $\varepsilon_{\max} = 398\%$, and none of the numerical results lies within the adopted 10% threshold. Even the minimum deviations are approximately 189% for the electron and ion temperatures and 299% for the radiation temperature. The simulations therefore strongly overestimate the experimental temperature trend, and the agreement must be regarded as poor.

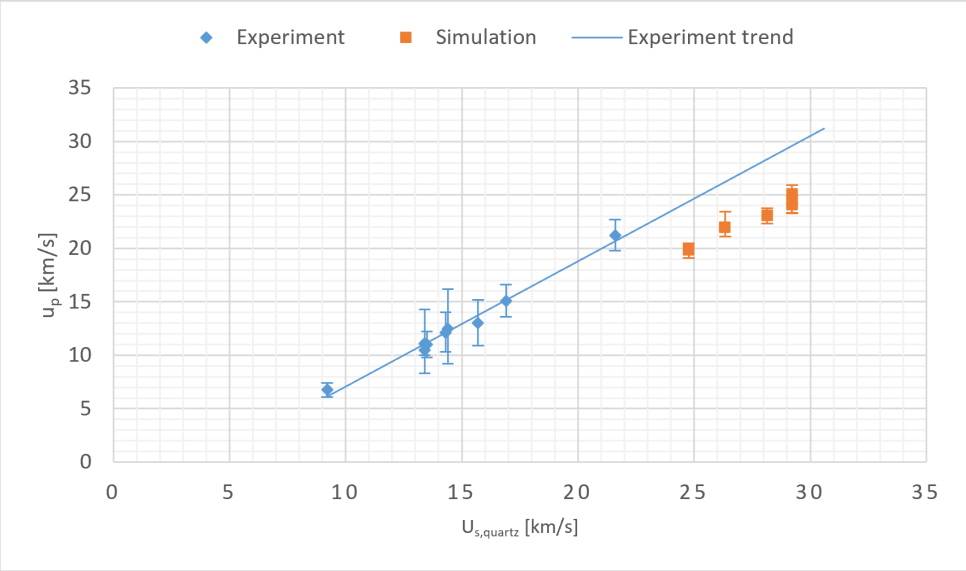

Figure 7.6: Post-shock particle velocity in the TMPTA foam as a function of the quartz shock velocity. The experimental values reported by Paddock et al. [5] are shown with their uncertainties, while the simulated points represent the time-averaged post-shock particle velocities and their temporal dispersion. The linear trend fitted to the experimental data is extrapolated over the range covered by the simulations.

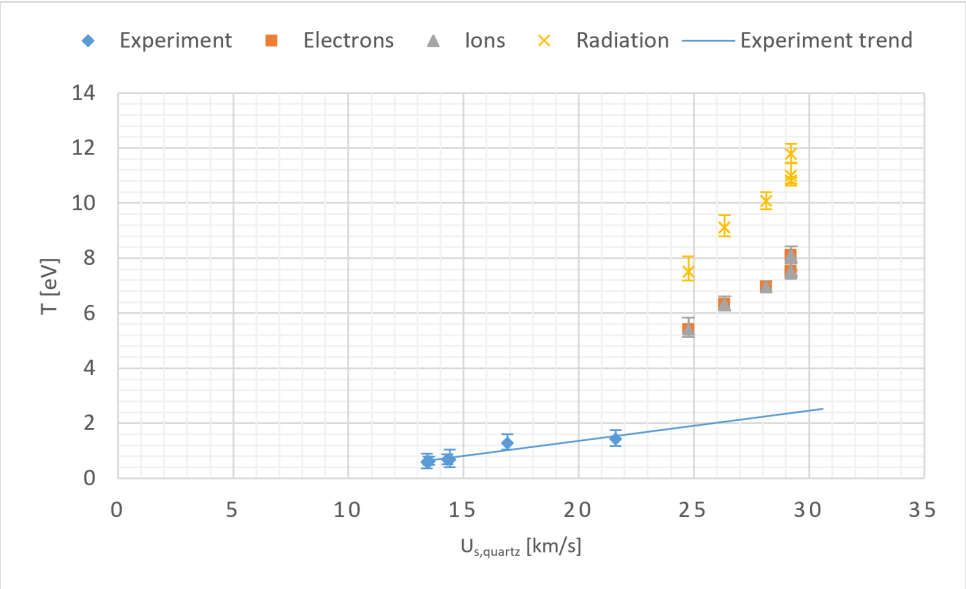

Figure 7.7: Post-shock temperature in the TMPTA foam as a function of the quartz shock velocity. The experimental values reported by Paddock et al. [5] are shown with their uncertainties, while the simulated points represent the time-averaged electron, ion, and radiation temperatures and their temporal dispersion. The linear trend fitted to the experimental data is extrapolated over the range covered by the simulations.

Unlike the quartz results, the three thermal components do not reach a common post-shock temperature in the TMPTA foam. The electron and ion temperatures remain approximately equilibrated, whereas the radiation temperature is systematically higher, indicating that matter and radiation are not in local thermal equilibrium within the selected region. This behavior may indicate that the adopted opacity treatment is not sufficiently representative of the experimental TMPTA foam. The foam is modeled using polystyrene at the prescribed reduced density, therefore the corresponding opacity data may not accurately reproduce the radiative properties of the actual porous material along its post-shock thermodynamic path. Consequently, the calculated emission, absorption, and matter-radiation coupling may differ from those occurring in the experiment.

Shock Velocity The shock velocity in the TMPTA foam, shown in Figure 7.8, is compared with the linear relation

$$U_{s,\mathrm{TMPTA}} = 0.8682\, U_{s,\mathrm{quartz}} + 5.4051,$$

where both $U_{s,\mathrm{TMPTA}}$ and $U_{s,\mathrm{quartz}}$ are expressed in $\frac{\mathrm{km}}{\mathrm{s}}$.

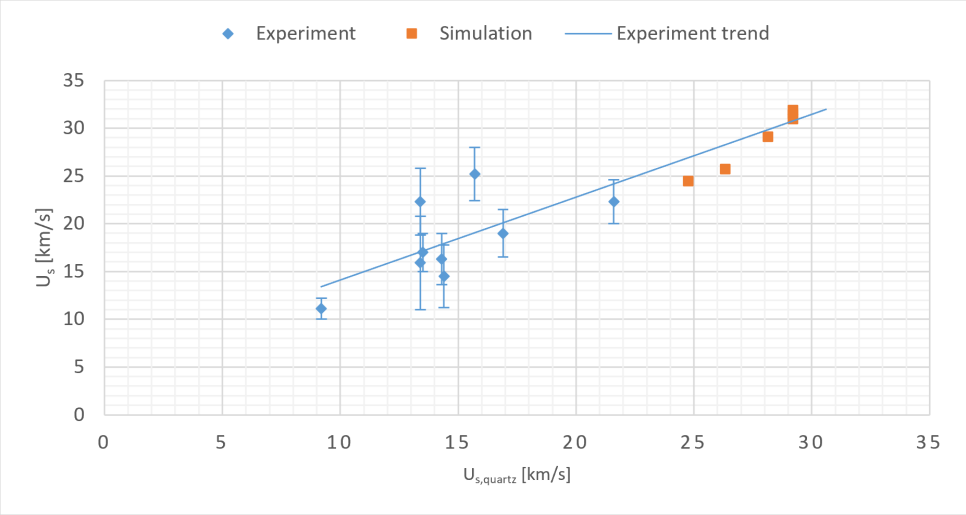

Figure 7.8: Shock velocity in the TMPTA foam as a function of the quartz shock velocity. The experimental values reported by Paddock et al. [5] are shown with their uncertainties, while the simulated results are compared with the linear trend fitted to the experimental data and extrapolated over the range covered by the simulations.

The linear fit gives RMSE $= 3.176\, \frac{\mathrm{km}}{\mathrm{s}}$. The maximum relative deviation between the extrapolated relation and the simulated results is $\varepsilon_{\max} = 9.17\%$. Since all six numerical values remain within the adopted 10% threshold, the simulations show good quantitative agreement with the continuation of the experimental relation between the shock velocities in quartz and in the TMPTA foam.

7.3 Temporal and One Dimensional Structures

To describe the main one-dimensional flow features of the simulated laser-target interaction, which are qualitatively common to all the investigated irradiation conditions, a single representative shot is considered throughout this section. The selected shot is characterized by

$$I = 8 \times 10^{13}\ \mathrm{W\,cm^{-2}},$$
$$\Delta t_{\mathrm{plateau}} = 2.5\ \mathrm{ns}.$$

7.3.1 Leading Shock Location and Velocity

The evolution of the leading-shock position $x_s(t)$ is shown in Fig. 7.9. The initial positions of the He-CH, CH-Au, Au-quartz, and quartz-TMPTA interfaces are located at $x = 20\ \mu$m, $x = 60\ \mu$m, $x = 63\ \mu$m, and $x = 103\ \mu$m, respectively. The intersections between the shock trajectory and these interface positions identify the time intervals during which the leading front propagates through each material.

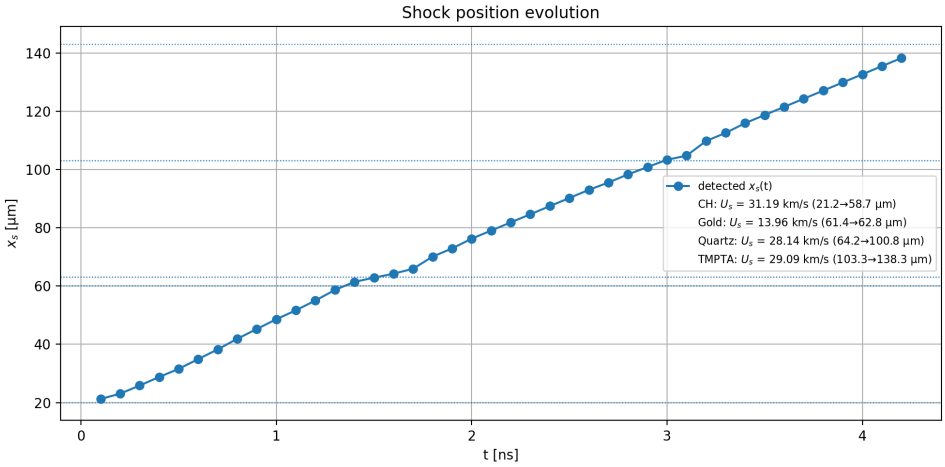

Figure 7.9: Position of the leading shock as a function of time for the representative laser shot. The horizontal blue segments indicate the initial spatial extent of the material layers: helium occupies the region up to $x = 20\ \mu$m, followed by CH, gold, quartz, and TMPTA.

The slope of the shock-position curve $x_s(t)$ provides a qualitative indication of the leading-shock velocity. Within the CH layer, the shock propagation is primarily controlled by the laser-driven ablation pressure and therefore by the imposed laser intensity. After the shock exits the directly ablated region, its propagation is instead governed by the interaction between the incoming wave and the thermodynamic response of each material. The pre and post-shock states, and consequently the transmitted shock velocity, are constrained by the material equation of state and by the Rankine-Hugoniot relations.

The changes in slope observed at the interfaces therefore reflect the transmission of the shock between materials characterized by different initial states and shock impedances. In the present simulation, the propagation velocity generally decreases as the front crosses the denser gold and quartz layers. Although the TMPTA foam has a lower initial density than CH, the shock reaches it only after propagating through the intermediate gold and quartz slabs and after the laser-driven loading has progressively evolved. Consequently,

the leading-shock velocity in the TMPTA foam remains lower than that observed in the CH layer. Nevertheless, it increases with respect to the value measured in quartz, consistently with the experimental relationship between post-shock particle velocity and shock velocity given by Eq. 7.11.

Since $x_s(t)$ is available only at the output times of the plot-files, the shock-position curve is discretely sampled. Small local variations in its slope should therefore not be interpreted as instantaneous accelerations or decelerations of the front. The position evolution is instead used to identify the time interval during which the shock propagates within each slab and to evaluate the corresponding average shock velocity U_s, previously employed in the comparison with the experimental results.

7.3.2 Plateau Temporal Evolution

The temporal evolution of the post-shock state is analyzed only in quartz and TMPTA foam, since these are the two materials for which the plateau values were extracted and used in the comparison with the experimental results. The analysis refers to the same representative laser shot considered in the previous paragraph. The simulation plot-files were written at intervals of 0.1 ns; consequently, consecutive data points are separated by this time interval whenever a valid plateau is detected in successive outputs.

Figure 7.10 shows the evolution of the post-shock density. In quartz, the density decreases almost monotonically from approximately 7.4 $\mathrm{g\,cm^{-3}}$ to 6.6 $\mathrm{g\,cm^{-3}}$ while the leading shock propagates through the slab. A similar, although less pronounced, trend is observed in the TMPTA foam, where the density decreases from approximately 1.48 $\mathrm{g\,cm^{-3}}$ to 1.42 $\mathrm{g\,cm^{-3}}$.

The pressure exhibits a more marked temporal decrease, as shown in Fig. 7.11. In quartz, the post-shock pressure falls from approximately 1510 GPa, shortly after the shock enters the slab, to about 1000 GPa before the front reaches the quartz-TMPTA interface. After transmission into the foam, a new post-shock state is established at a substantially lower pressure. The first values in TMPTA are close to 185 GPa, after which the pressure progressively decreases to approximately 150 GPa.

Fig. 7.12 presents the corresponding particle velocity. In quartz, it decreases from approximately 18.7 $\mathrm{km\,s^{-1}}$ to 15.2 $\mathrm{km\,s^{-1}}$. In the TMPTA foam, the particle velocity is higher than in quartz despite the lower post-shock pressure, consistently with the different Hugoniot response of the two materials. The first values obtained after transmission through the interface exhibit greater variability because the post-shock region is still being established. After this initial transient, the particle velocity gradually decreases from approximately 23.8 $\mathrm{km\,s^{-1}}$ to 22.3 $\mathrm{km\,s^{-1}}$.

The thermal evolution is shown in Fig. 7.13. In quartz, the electron, ion, and radiation temperatures are nearly coincident throughout the analyzed interval and decrease from approximately 7.9 eV to 6.7 eV. The shocked quartz can therefore be regarded as being close to thermal equilibrium among the three energy components over the considered timescale.

A different behavior is observed in the TMPTA foam. The electron and ion temperatures remain approximately equal and decrease from about 7.1 eV to 6.8 eV, indicating rapid equilibration between the two material components. The radiation temperature instead remains distinctly higher, decreasing from approximately 10.4 eV to 9.8 eV, consistently with what was previously observed in the comparison with the experimental results. The shocked foam is therefore in electron-ion thermal equilibrium, but not in

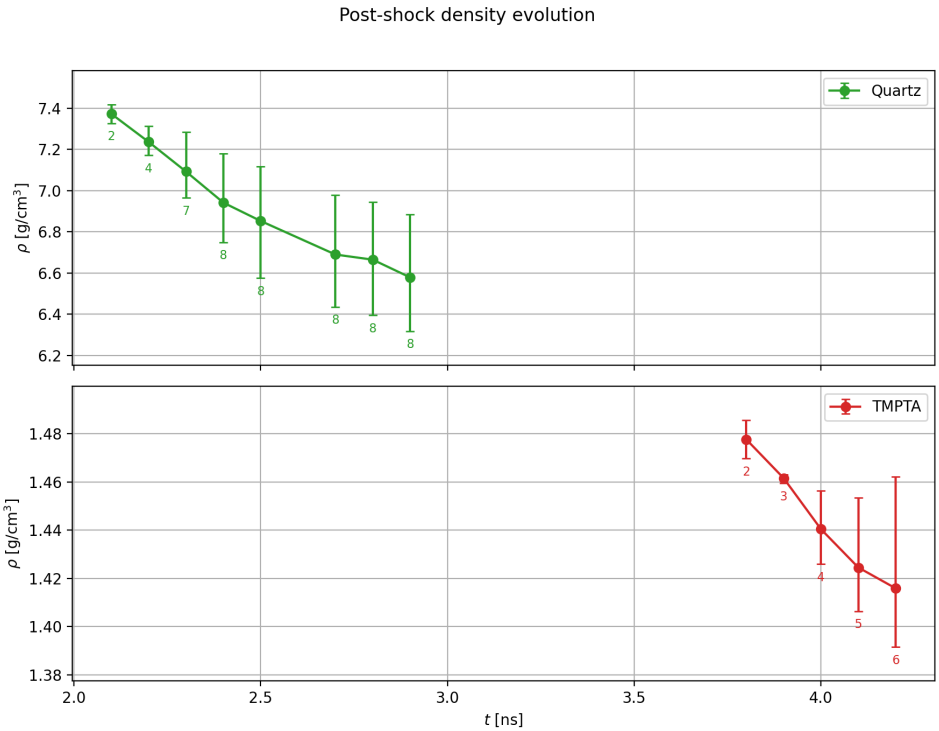

Figure 7.10: Temporal evolution of the post-shock density in quartz and TMPTA foam for the representative laser shot. Only the times for which a valid post-shock plateau is identified are reported. The error bars indicate the minimum and maximum density values within the detected plateau, while the number below each point gives the number of cells included in the spatial average.

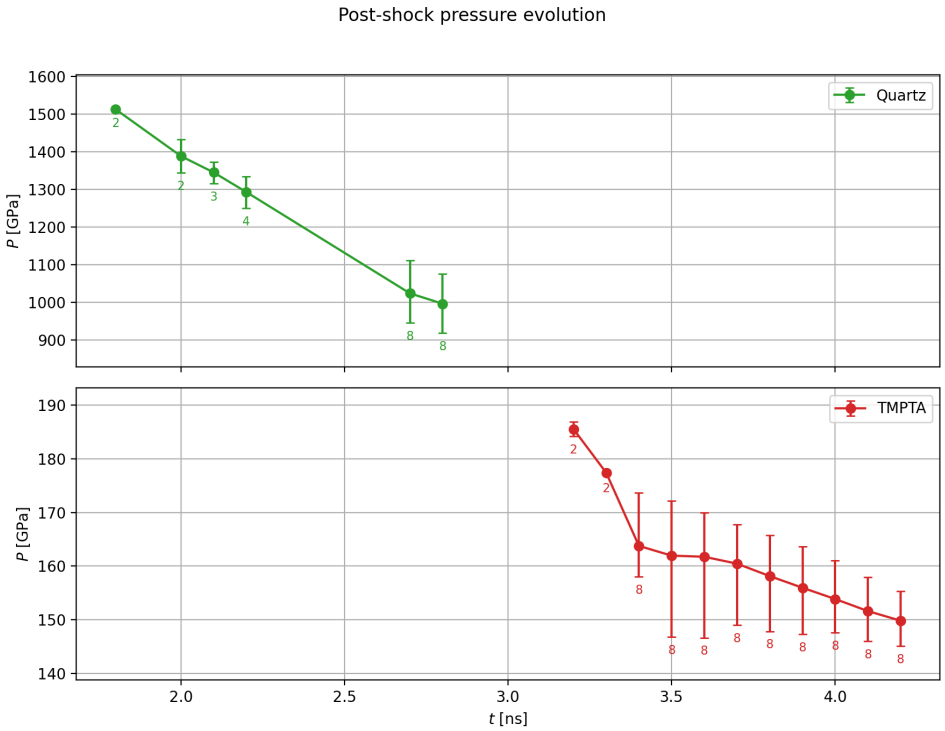

Figure 7.11: Temporal evolution of the post-shock pressure in quartz and TMPTA foam for the representative laser shot. The error bars indicate the minimum and maximum pressure values within the detected plateau, while the number below each point gives the number of cells included in the spatial average.

complete equilibrium with the radiation field.

The discontinuities between the quartz and TMPTA distributions should not be interpreted as the continuous evolution of the same thermodynamic state. When the leading shock crosses the quartz-TMPTA interface, the change in material properties and shock impedance produces a different transmitted shock and, consequently, a new post-shock state. The resulting conditions are determined by the initial state and equation of state of the foam, together with the Rankine-Hugoniot relations given in Eq. 2.8.

Within each material, however, pressure, density, particle velocity, and temperature all decrease while the leading front continues to propagate through the same slab. The post-shock state must therefore be regarded as an evolving condition rather than as a stationary plateau. Accordingly, the values used in the comparison with the experiment represent temporal averages over the valid post-shock distributions. Since this gradual reduction occurs while the shock remains within the same material, it cannot be attributed directly to the crossing of an interface. A possible explanation is the progressive influence of the global rarefaction developing behind the leading shock as the ablated and shocked target expands towards the left outflow boundary. As this rarefaction approaches the region immediately behind the shock, it may reduce both the spatial extent of the plateau and the thermodynamic state established within it.

7.3.3 One Dimensional structures

To represents the most relevant 1D spatial flow features, some representative time instants are chosen in order to have the shock front and plateau for each slabs. The shock

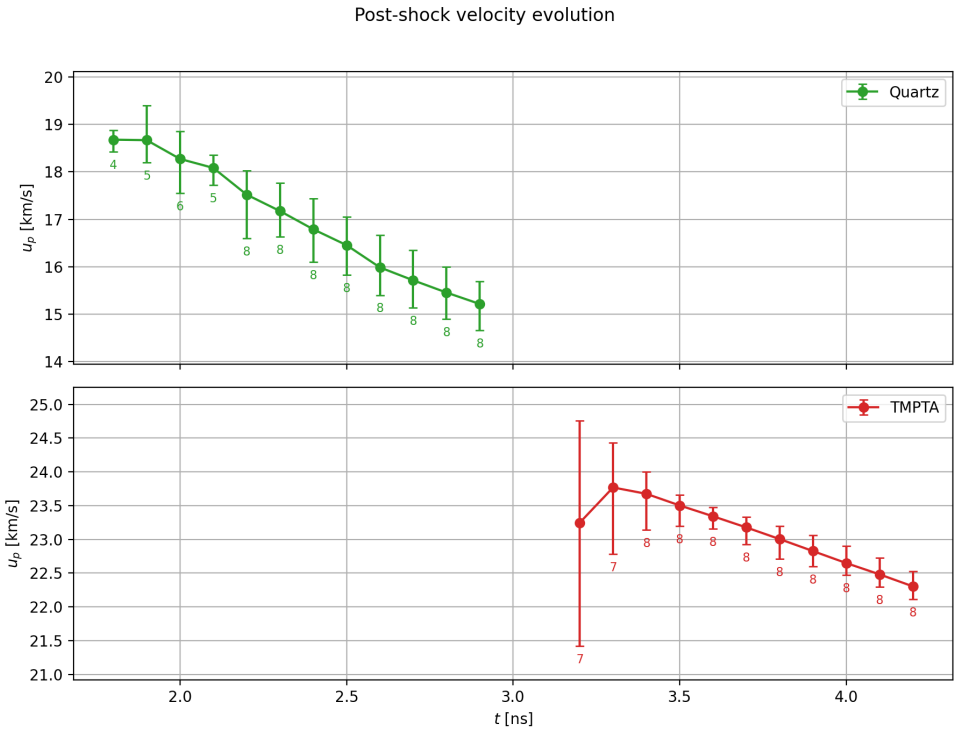

Figure 7.12: Temporal evolution of the post-shock particle velocity in quartz and TMPTA foam for the representative laser shot. The error bars indicate the minimum and maximum particle-velocity values within the detected plateau, while the number below each point gives the number of cells included in the spatial average.

front is the first discontinuity starting from the right side of the plots and, as expected, corresponds to the same position for all flow variables.

Starting from the plastic CH ablator (Figure 7.14), the shock front is located at $x \approx 55$ μm. Behind it, the material undergoes rarefaction as the irradiated CH surface expands towards the low-density helium region. This region includes both the ordinary post-shock rarefaction and, closer to the left boundary, the expanding laser-produced plasma. Accordingly, it is characterized by a strong outflow, as indicated by the large negative longitudinal velocity and by the pronounced decrease in pressure and density relative to the post-shock plateau. Within this broader rarefaction region, the subregion where the temperatures exceed 40 eV corresponds specifically to the laser-produced plasma, in which the electron and ion temperatures are not in thermal equilibrium.

At this instant $t = 1.1$ ns, it is important to consider not only the generation of the shock within the CH ablator, but also the differences among the ion, electron and radiation temperatures. In the shock-compressed CH, these first two temperatures are approximately equal. This differs from the laser-heated plasma region, where the electrons reach higher temperatures because the laser energy is deposited directly into the electronic component and electron-ion thermal equilibration is not instantaneous. In the shocked material, instead, ions and electrons respond together to the sudden increase in pressure and density, producing a temperature jump to approximately 11 eV. This increase is associated with the compression of the material and with its thermodynamic response through the EOS, rather than with direct laser heating, as occurs in the ablated region.

The radiation temperature shows a markedly different behavior. It has already increased in regions that have not yet been reached by the hydrodynamic shock, but it

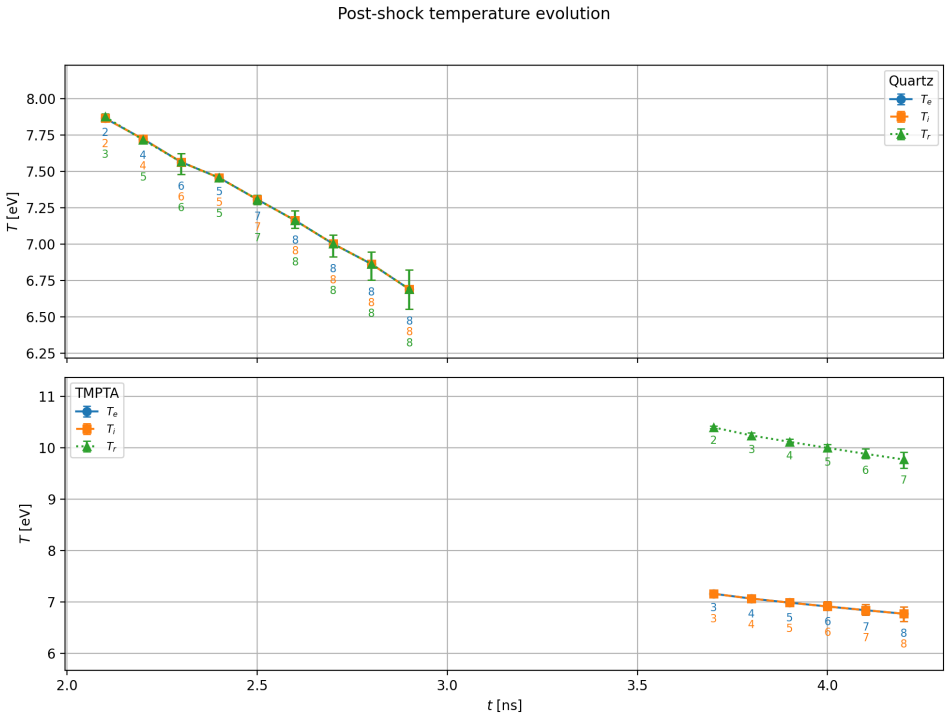

Figure 7.13: Temporal evolution of the post-shock electron, ion, and radiation temperatures in quartz and TMPTA foam for the representative laser shot. For each temperature, the error bars indicate the minimum and maximum values within the detected plateau, while the number below each point gives the number of cells included in the corresponding spatial average.

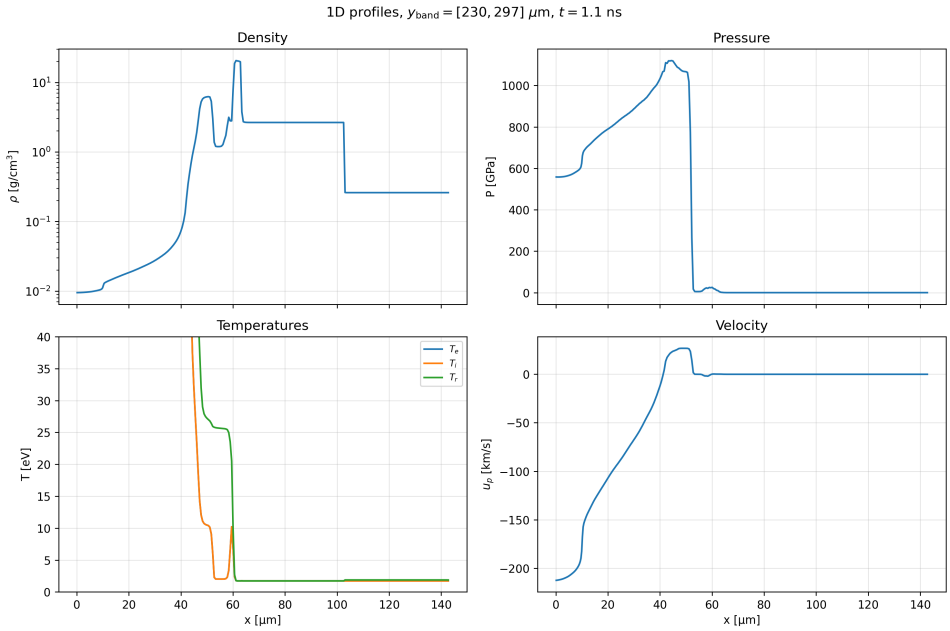

Figure 7.14: One dimensional distribution of the main flow variables at time $t = 1.1\,\text{ns}$, when the shock front is in the CH slab

rapidly falls back towards its initial value at the Au layer. This behavior is consistent with the purpose of the gold foil in the reference experiment, namely to reduce radiative preheating of the quartz and TMPTA layers under investigation [5]. Radiative energy propagates through the CH much more rapidly than the hydrodynamic shock, thereby heating the ablator ahead of the shock front. Its propagation is then strongly attenuated at the Au layer because of the high opacity of gold, presented in Section 6.1. The strong absorption of radiation within the Au foil may nevertheless produce some local energy deposition before the arrival of the main shock. This effect could explain the ion-temperature peak observed near $x \approx 60$ μm. The resulting local pressure increase generates a weak compression wave that propagates back into the lower-density CH. However, its amplitude is small compared with that of the main laser-driven shock, and its influence on the overall shock evolution can therefore be considered negligible.

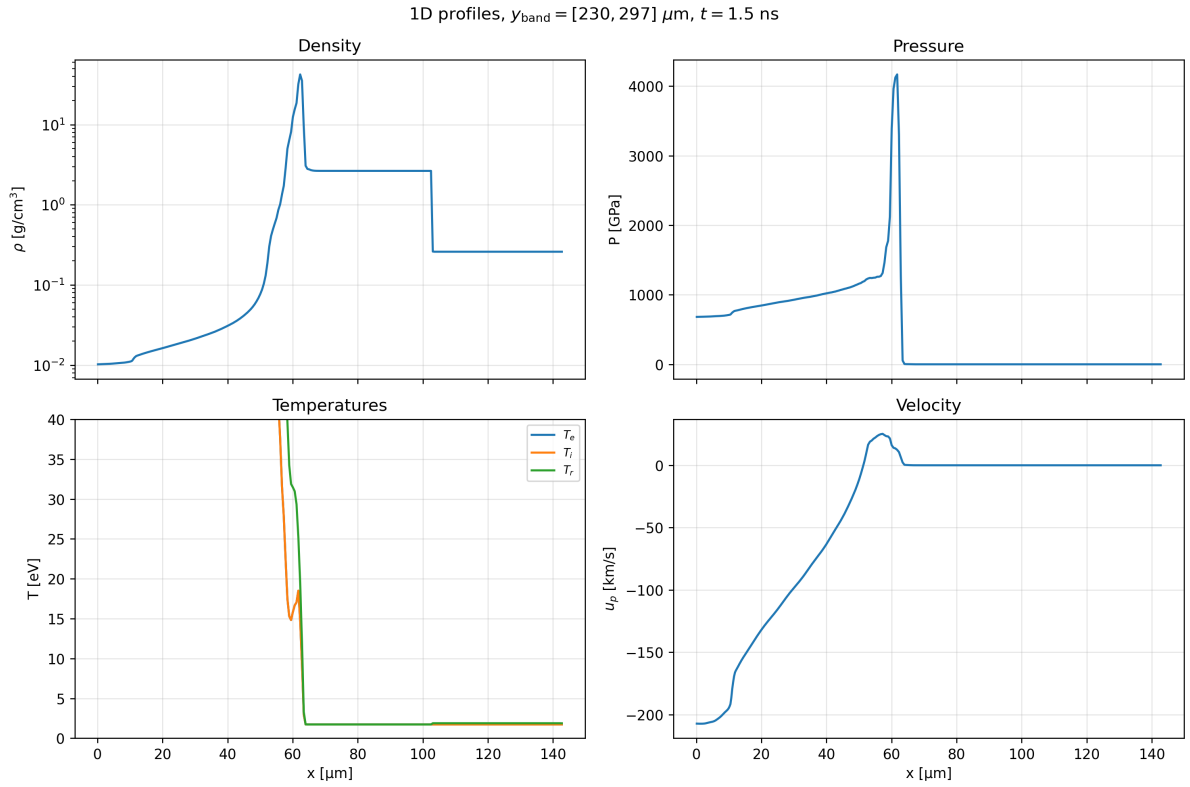

Figure 7.15: One dimensional distribution of the main flow variables at time $t = 1.5$ ns, when the shock front is in the gold slab

When the shock enters the Au foil, the increase in shock impedance relative to the CH ablator produces a marked rise in the pressure jump associated with the transmitted wave. Since gold also has the highest shock impedance among all the target materials, the shocked Au layer reaches the highest post-shock compression state observed throughout the target.

A further indication of the heat-shielding function of the Au foil is provided by the radiation-temperature profile. The radiation front does not propagate significantly beyond the gold layer, thereby limiting the radiative preheating of the downstream quartz and TMPTA slabs.

At the Au-quartz interface, the shock propagates from a higher to a lower material impedance Z:

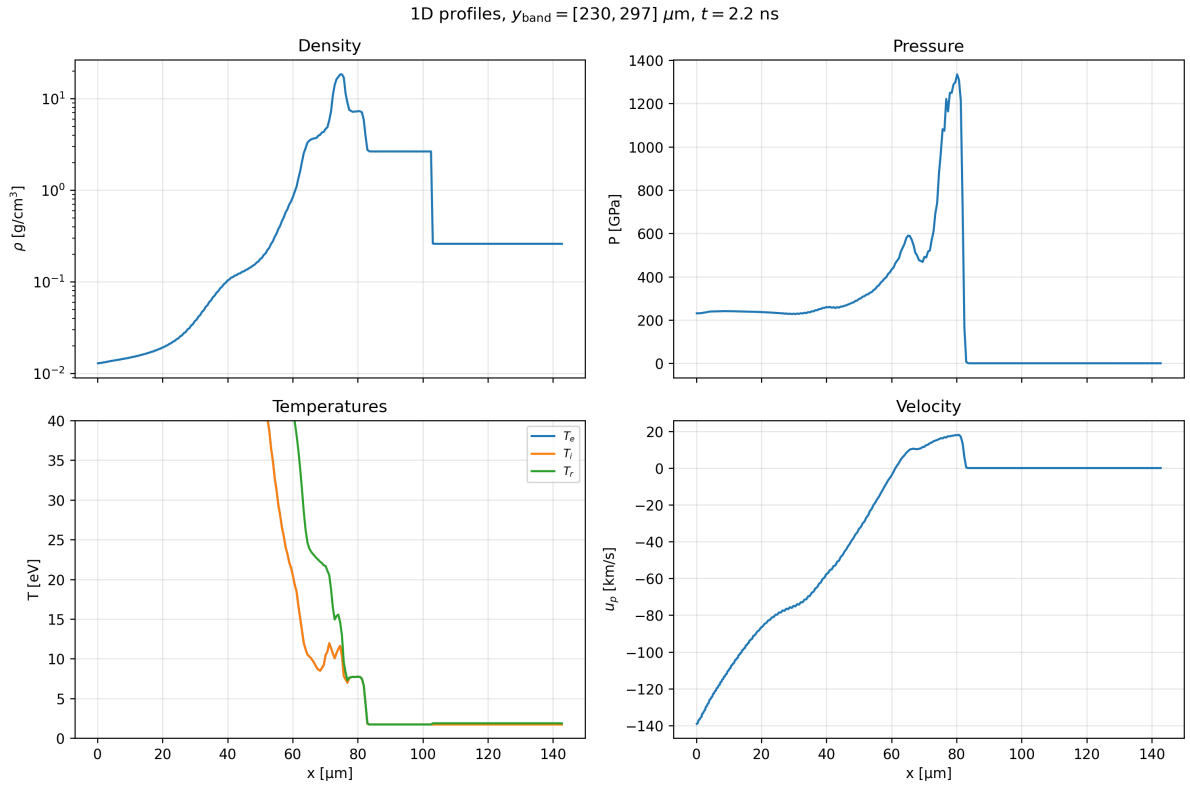

Figure 7.16: One-dimensional distribution of the main flow variables at time $t = 2.2\,\text{ns}$, when the shock front is located inside the quartz slab.

$$Z_{\text{Au}} = 27 \times 10^6 \,\frac{\text{g}}{\text{cm}^2\,\text{s}} \;\longrightarrow\; Z_{\text{quartz}} = 7.46 \times 10^6 \,\frac{\text{g}}{\text{cm}^2\,\text{s}}.$$

The two impedances are calculated using Equation 2.11, with the initial density of each material and the corresponding average shock velocity evaluated within the slab, as shown in Figure 7.9. This reduction is associated with the sudden decrease in the shock state transmitted into the quartz while the an increment in particle longitudinal velocity as expected from theory presented in Figure 2.3.

The rarefaction wave that would normally connect the shocked states in the Au and quartz is not clearly distinguishable in the profile. The expansion towards the left boundary is sufficiently strong that the narrow shocked plateau within the thin Au foil has already been largely eroded. The transient evolution of the average plateau quantities in the quartz, shown in the previous subsection, indicates that the same rarefaction also progressively affects the shocked-quartz region, causing its pressure and the other post-shock quantities to decrease with time.

Another relevant feature of Figure 7.16 is the presence of a second compressive structure behind the leading shock. This structure may correspond to the reflected shock generated at the CH-Au interface, as expected when the incident shock encounters the higher-impedance Au layer, with

$$Z_{\text{Au}} > Z_{\text{CH}} = 3.74 \times 10^6 \frac{\text{g}}{\text{cm}^2\,\text{s}}.$$

The pressure plateau associated with this reflected wave is also progressively eroded by the overall rarefaction of the target towards the left boundary. Nevertheless, cor-

responding plateau-like structures are visible in both the density and velocity profiles at approximately the same position, supporting the interpretation of this feature as a reflected compressive wave.

Regarding the thermal behavior, the electron, ion and radiation temperatures approximately coincide within the shocked quartz. This indicates that the three components are close to local thermal equilibrium in this region. Therefore, the observed temperature increase is associated with shock compression and with the transition from the initially unperturbed material to the shocked state, which gives another confirmation that the quartz and foam are not preheated by radiation.

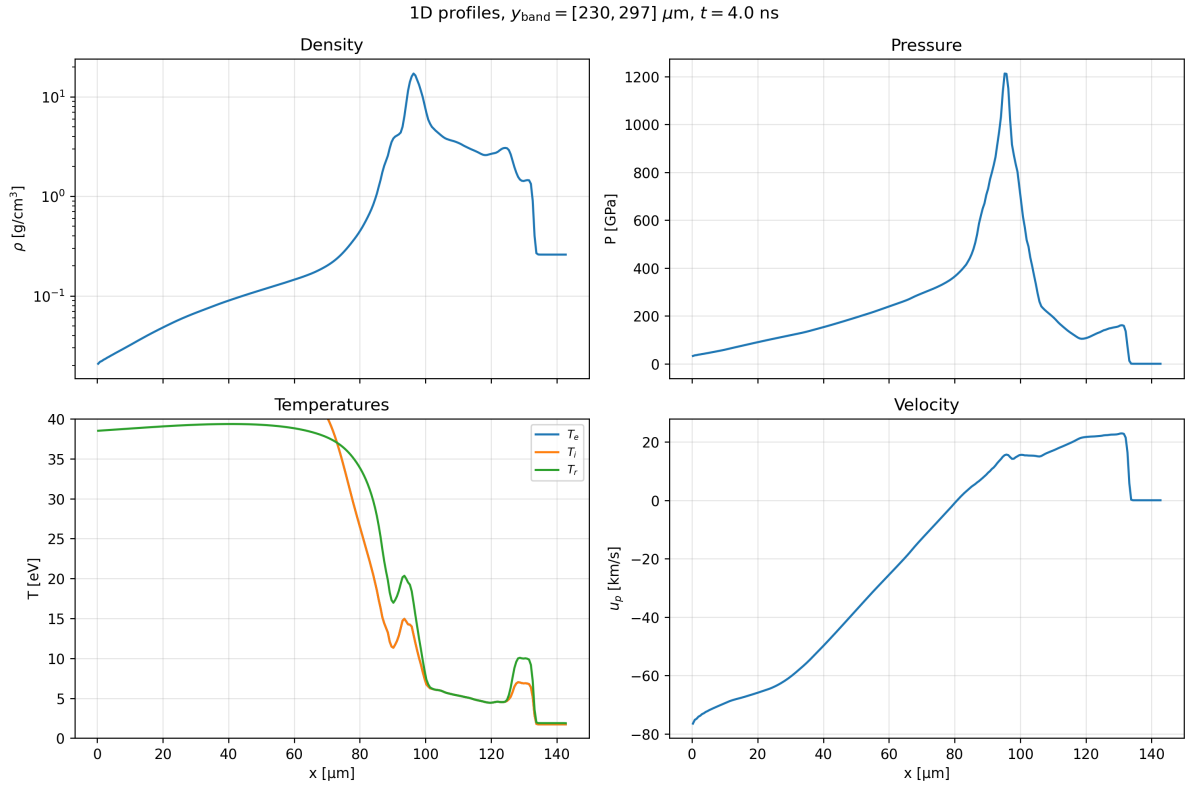

Figure 7.17: One dimensional distribution of the main flow variables at time $t = 4\,\text{ns}$, when the shock front is in the foam slab

The propagation of the shock into the TMPTA foam exhibits features similar to those observed at the Au-quartz interface. In this case, the shock again passes from a higher-impedance material to a lower-impedance one:

$$Z_{\text{quartz}} \longrightarrow Z_{\text{TMPTA}} = 0.76 \times 10^6 \, \frac{\text{g}}{\text{cm}^2\,\text{s}}.$$

As in the quartz profile, Figure 7.17 shows a characteristic density step behind the leading shock, corresponding to the quartz-TMPTA interface. At this stage, the shock is sufficiently far from the laser-produced plasma that the temperature profiles are no longer dominated by the extremely high values associated with the ablation region. This makes it possible to distinguish more clearly the characteristic increase in post-shock temperature that occurs when the shock is transmitted from a higher-impedance material into a lower-impedance one. This behavior is expected because it was already observed in the purely hydrodynamic ideal-gas reference case presented in Figure 2.2 and discussed

in Section 2.2. In fact, although the materials considered here are described by tabulated equations of state rather than by an ideal-gas model, the qualitative interpretation based on shock impedance remains applicable to both fluids and solids [9].

The ion and electron temperatures are approximately equal throughout the shocked region, indicating that the material is close to thermal equilibrium. The radiation temperature, however, remains distinct from both T_{ion} and T_{ele}, consistently with the trend previously identified in the temporal profiles.

7.4 Two Dimensional Structures

7.4.1 Flow Variables Distributions

The one-dimensional profiles discussed previously were obtained by averaging the two-dimensional simulation fields over the transverse interval $y \in [230\,,\,297]$ μm. The complete two-dimensional fields are then post-processed using the VisIt software [25]. This analysis is used to identify the geometrical features lost in the one-dimensional reduction and to verify that the selected averaging region provides a representative description of the longitudinal shock propagation. The same representative simulation and time instants previously considered in the one-dimensional profiles are analyzed. At $t = 2.2$ ns, the leading shock is propagating through the quartz slab, whereas at $t = 4.0$ ns it has entered the TMPTA foam.

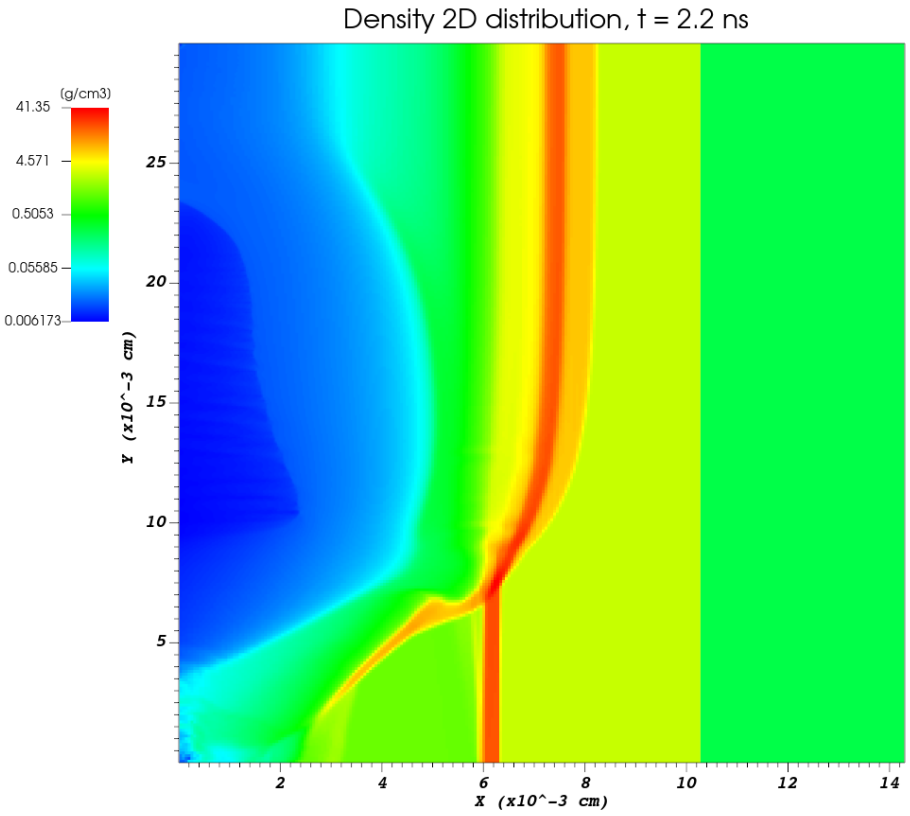

Figure 7.18: Two-dimensional density distribution at $t = 2.2$ ns for the simulation with $I = 8 \times 10^{13}$ $\frac{\text{W}}{\text{cm}^2}$ and a laser-pulse duration of 3.5 ns.

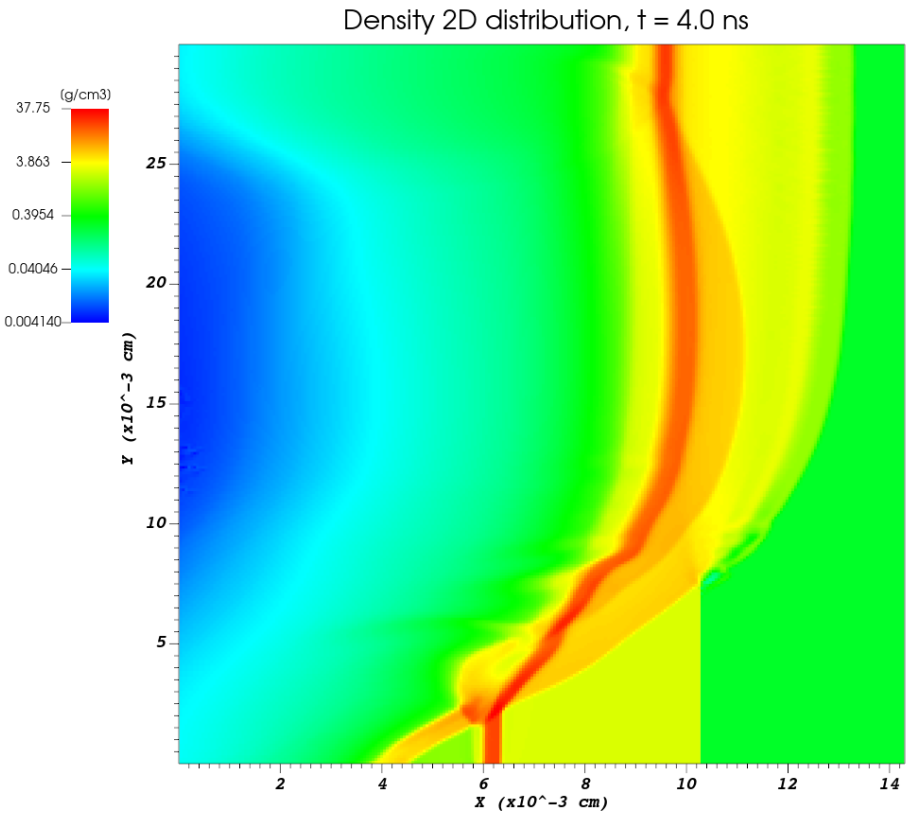

Figure 7.19: Two-dimensional density distribution at $t = 4.0$ ns for the simulation with $I = 8 \times 10^{13}$ $\frac{\mathrm{W}}{\mathrm{cm}^2}$ and a laser-pulse duration of 3.5 ns.

Figures 7.18 and 7.19 show the two-dimensional density structure during the propagation of the leading shock. In agreement with the one-dimensional profiles discussed previously, the leading front is located slightly beyond $x = 80$ μm at $t = 2.2$ ns, while at $t = 4.0$ ns it has propagated to approximately $x = 130$ μm. In the upper portion of the irradiated region, which includes the transverse interval used for the one-dimensional averaging, the compression structure remains approximately planar. The density gradients are predominantly aligned with the longitudinal direction, and the position of the front varies only weakly with y. This confirms that, in this region, the leading shock preserves an approximately one-dimensional character.

The same figures also show that this behavior is not representative of the entire transverse domain. A markedly different geometry develops near the lower boundary of the laser spot, located at approximately $y = 100$ μm. At this transverse boundary, the laser-driven plasma is adjacent to a region that is not directly irradiated. The resulting pressure imbalance generates lateral rarefaction waves, which propagate from the edge of the laser spot toward the center of the irradiated region, while the ablated plasma expands outward. When these rarefaction waves reach the shocked material, they locally reduce the post-shock pressure and slow down the corresponding portion of the shock front. As a result, the compression structure bends toward smaller values of x, as schematically illustrated in Figure 7.1.

The curvature of the leading shock therefore does not remain confined to the immediate edge of the laser spot. As time increases, the lateral rarefaction waves penetrate

progressively farther toward the center of the irradiated region, extending the curved portion of the front. This effect is a general two-dimensional hydrodynamic feature of the simulation. The same mechanism is responsible for the curved structures observed in the pressure, longitudinal velocity, and temperature maps discussed below. Nevertheless, during the considered evolution, these multidimensional effects remain mainly outside the interval $y \in [230\,,\,297]$ μm. This is why the selected averaging band can still be used to extract representative one-dimensional profiles and post-shock quantities for the leading shock.

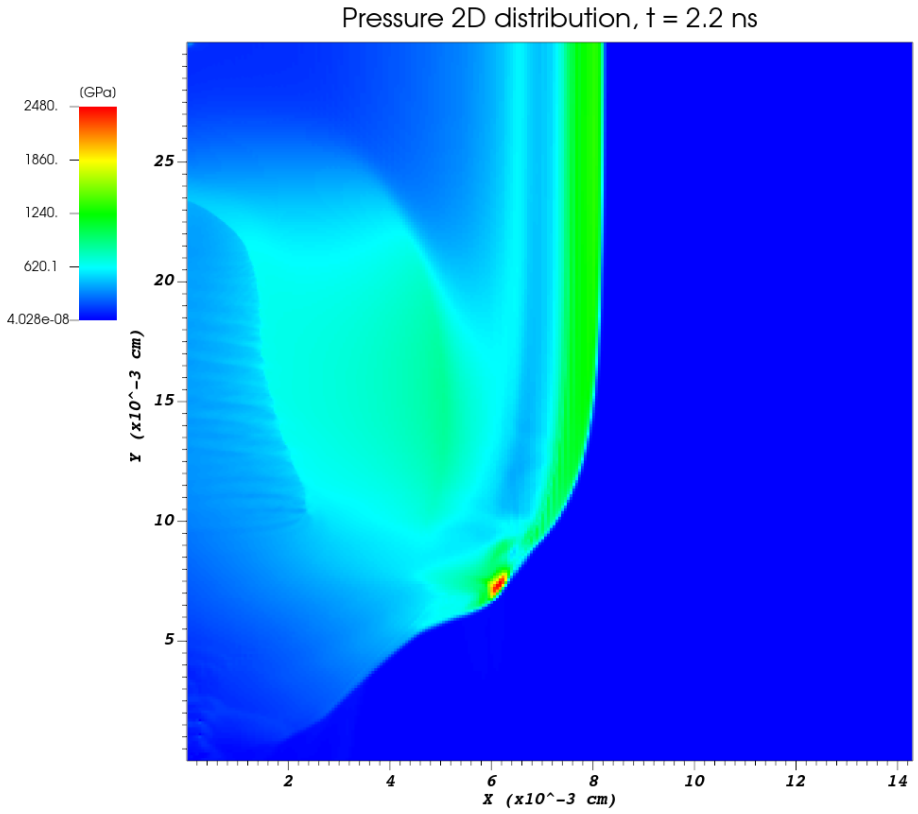

Figure 7.20: Two-dimensional pressure distribution at $t = 2.2$ ns for the simulation with $I = 8 \times 10^{13}\ \frac{\mathrm{W}}{\mathrm{cm}^2}$.

The pressure maps in Figures 7.20 and 7.21 exhibit the same geometrical distinction seen in the density profiles. The pressure front is nearly vertical in the upper part of the domain, while it becomes increasingly curved when approaching the lower edge of the laser spot. The high-pressure region behind the leading shock consequently has an approximately uniform longitudinal extension near the symmetry boundary, but develops a broader and more complex shape in the lateral-expansion region.

A localized pressure maximum is visible near the curved portion of the front. This structure first appears when the longitudinal part of the leading shock leaves the Au layer, which is the slab exhibiting the largest post-shock compression. Since the curved portion of the front reaches the Au-quartz interface at a later time, part of the shocked gold remains concentrated along this oblique section of the wave. Its position and persistence are therefore consistent with highly compressed Au being progressively reached and transported by the curved shock front.

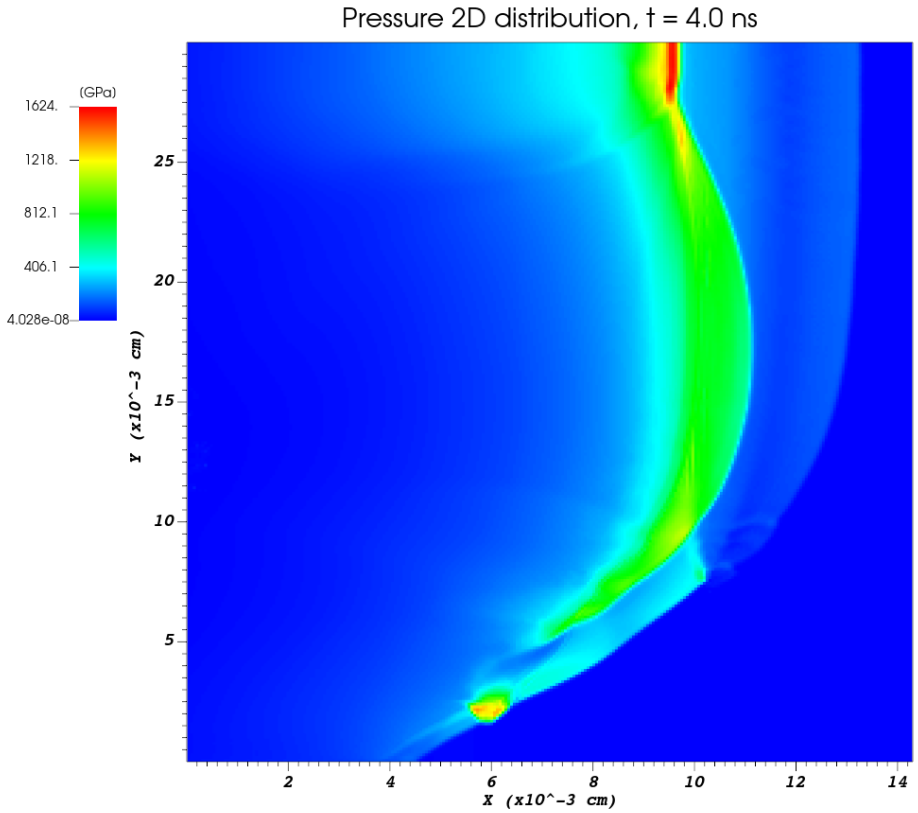

Figure 7.21: Two-dimensional pressure distribution at $t = 4.0$ ns for the simulation with $I = 8 \times 10^{13} \frac{\mathrm{W}}{\mathrm{cm}^2}$.

At $t = 4.0$ ns, the longitudinal leading shock has already propagated deeply into the TMPTA foam, beyond $x \simeq 130$ μm in the upper part of the domain. Several secondary compression fronts are nevertheless visible behind it. Similar structures can also be identified in the density, velocity, and temperature fields. They are generated because the laser continues to deposit energy and sustain the ablation drive during most of the interval preceding this snapshot, launching additional compression waves into the target. Although the pulse has ended by $t = 4.0$ ns, these secondary fronts remain present in the domain. Their detailed evolution is not considered in this work, which focuses exclusively on the first right-propagating leading shock.

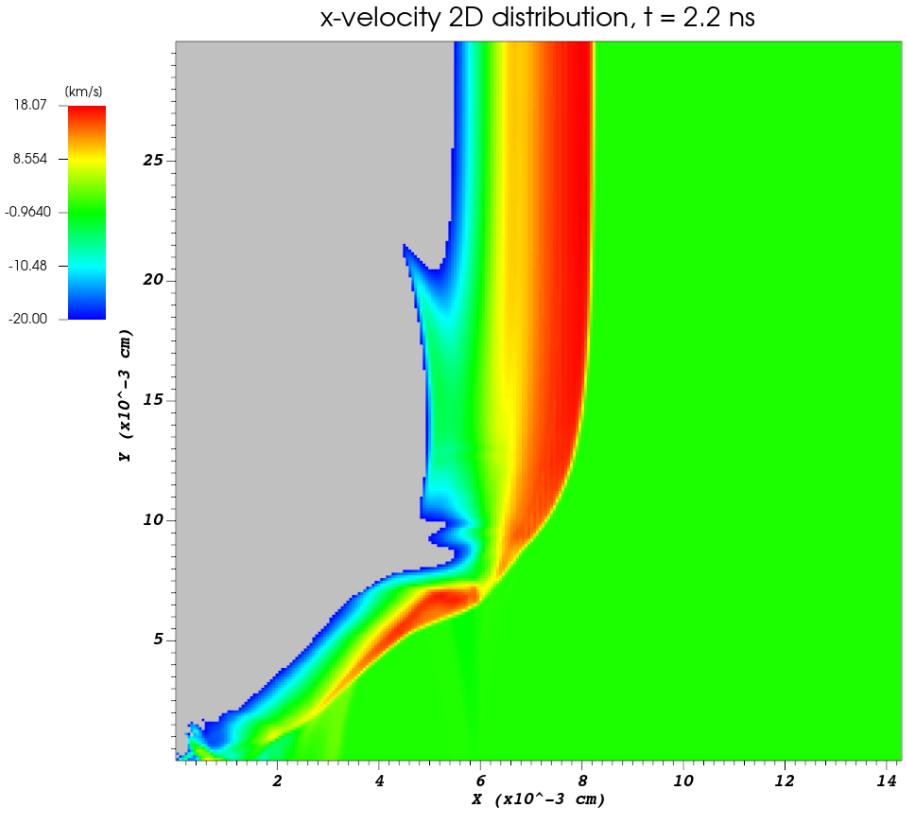

Figure 7.22: Two-dimensional distribution of the longitudinal velocity at $t = 2.2$ ns for the representative simulation.

Figures 7.22 and 7.23 distinguish the forward motion of the compressed target from the plasma expanding toward the laser side. The transition between these regions follows the curved geometry already observed in the density and pressure fields. Near the lower edge of the illuminated area, the longitudinal velocity therefore presents a clear dependence on y, consistently with the lateral deformation of the hydrodynamic structures.

Conversely, the velocity field is substantially more uniform along the transverse direction near the symmetry boundary. In this region, the longitudinal motion is dominant, and the different velocity layers remain nearly parallel to the initial material interfaces. This behavior is consistent with an approximately one-dimensional propagation inside the averaging band.

The gray area corresponds to longitudinal velocities below the lower limit of the displayed color scale, $v_x = -20$ km s^{-1}. These large negative velocities are associated with

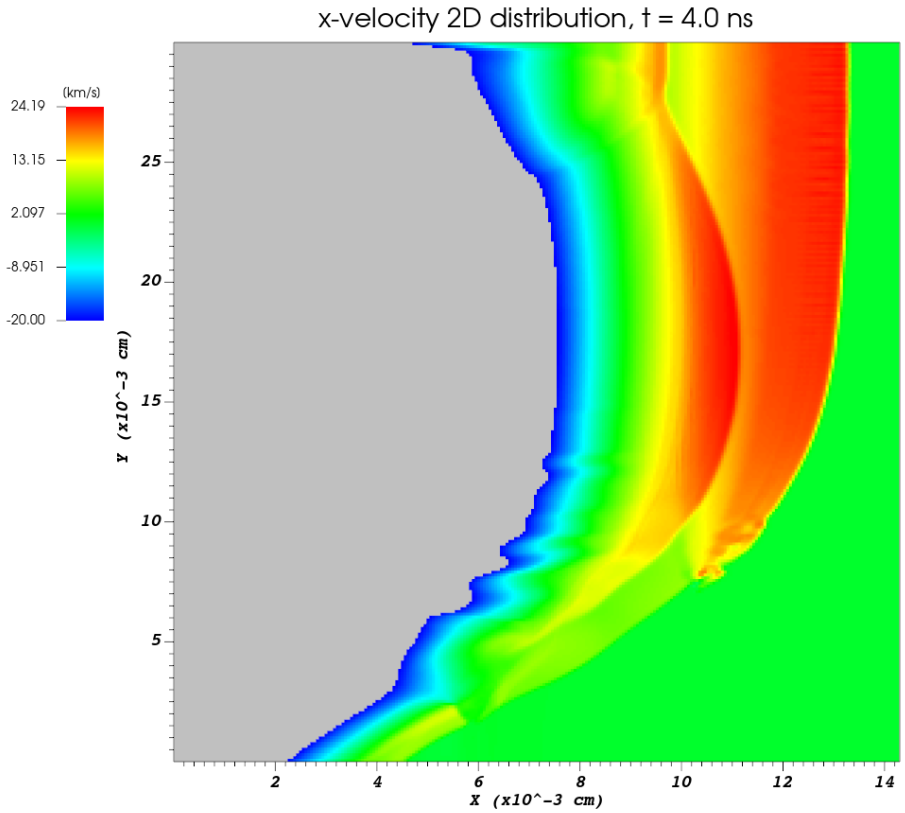

Figure 7.23: Two-dimensional distribution of the longitudinal velocity at $t = 4.0$ ns for the representative simulation.

the ablated and shocked material expanding toward the left outflow boundary. This backward expansion is also responsible for the global rarefaction propagating through the target behind the compression structures, previously identified in the one-dimensional profiles.

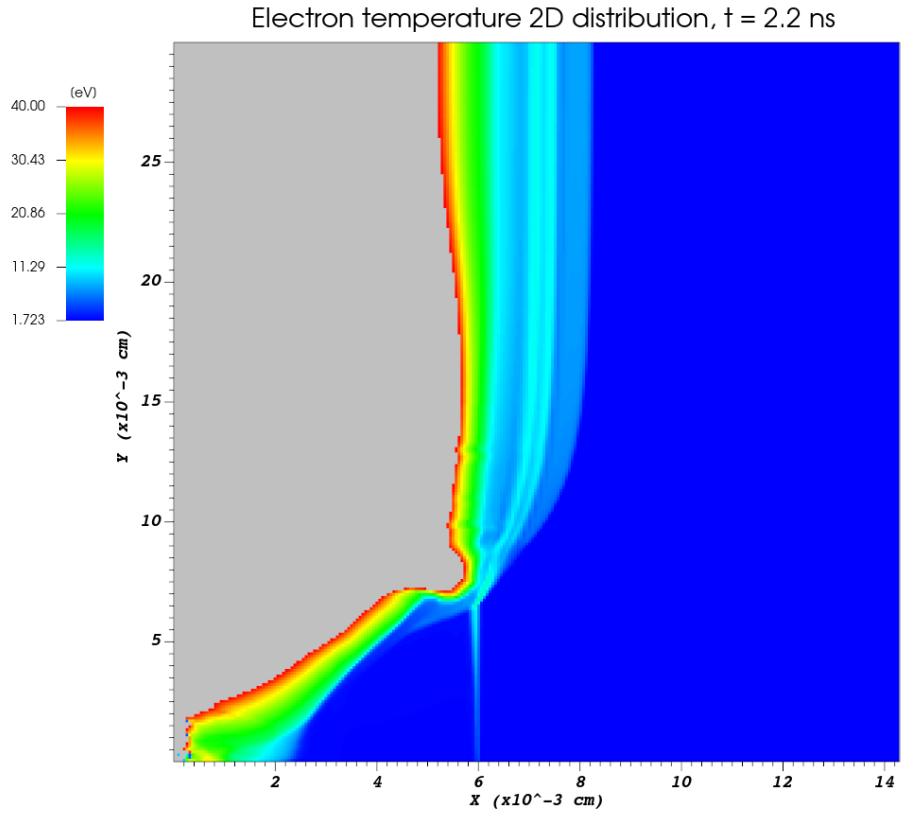

Figure 7.24: Two-dimensional electron-temperature distribution at $t = 2.2$ ns for the representative simulation. The gray region corresponds to temperatures above the upper limit of the displayed color scale, $T_{\mathrm{ele}} = 40$ eV.

The electron and ion temperature maps in Figures 7.24, 7.25, 7.26, and 7.27 present closely related spatial structures, confirming the near thermal equilibrium between T_{ele} and T_{ion} in the shocked quartz and TMPTA foam already observed in the one-dimensional profiles. In these slabs, the temperature distribution follows the geometry of the leading shock previously identified in the density and pressure maps. This behavior is expected, since the increase of both material temperatures is mainly determined by the post-shock thermodynamic state rather than by direct laser ablation. The thermal front is therefore approximately planar in the upper part of the irradiated region, including the transverse interval used for the one-dimensional averaging, while it becomes progressively curved near the lower edge of the laser spot. In the latter region, the lateral rarefaction waves and the transverse expansion of the ablated plasma modify the local shock structure, producing the same two-dimensional deformation already identified in the hydrodynamic variables. This confirms that, although the laser-ablated region is strongly non-uniform and reaches temperatures above the plotted range, the material temperature inside the analyzed slabs remains primarily controlled by shock compression.

The gray regions correspond to temperatures exceeding 40 eV, which is the upper

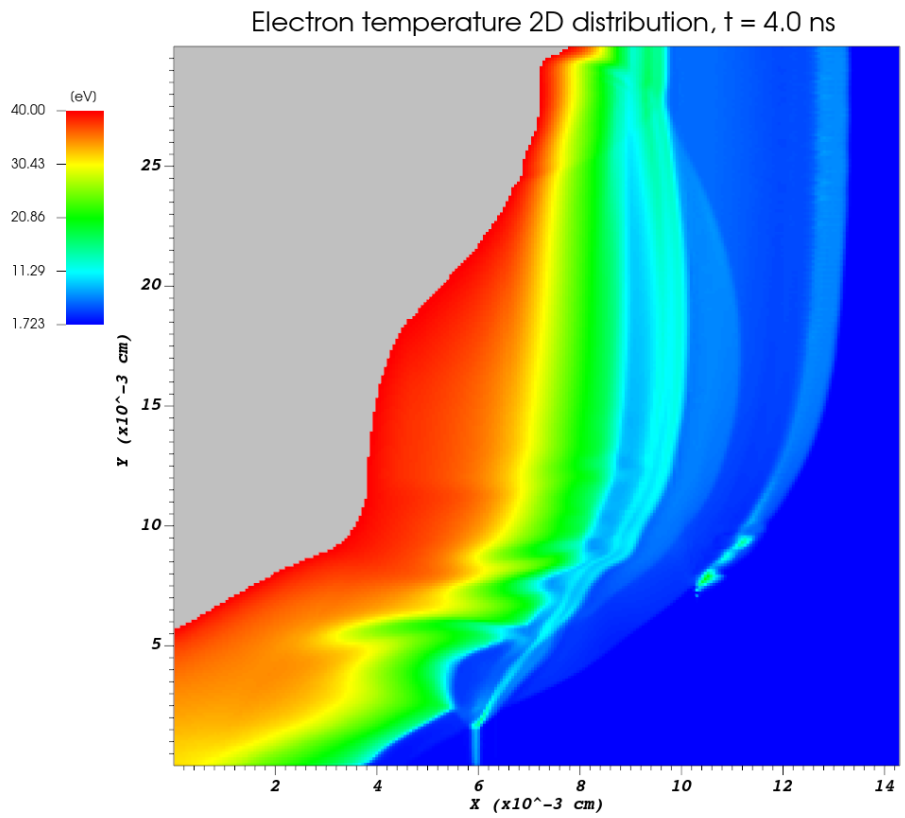

Figure 7.25: Two-dimensional electron-temperature distribution at $t = 4.0$ ns for the representative simulation. The gray region corresponds to temperatures above the upper limit of the displayed color scale, $T_{\mathrm{ele}} = 40$ eV.

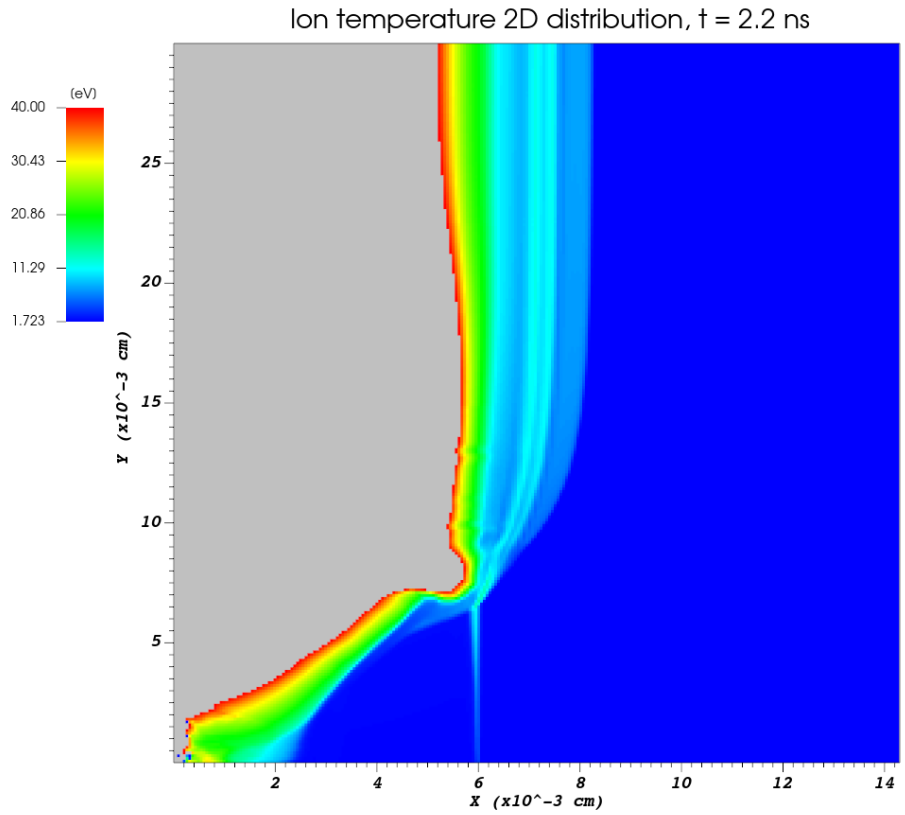

Figure 7.26: Two-dimensional ion-temperature distribution at $t = 2.2$ ns for the representative simulation. The gray region corresponds to temperatures above the upper limit of the displayed color scale, $T_{\text{ion}} = 40$ eV.

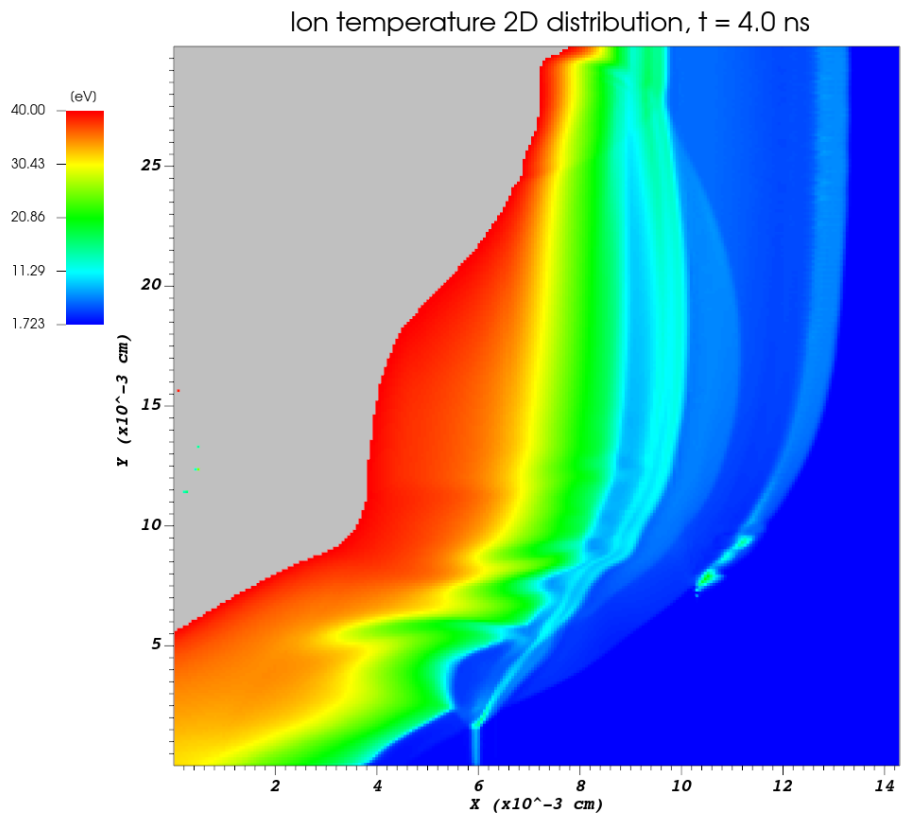

Figure 7.27: Two-dimensional ion-temperature distribution at $t = 4.0$ ns for the representative simulation. The gray region corresponds to temperatures above the upper limit of the displayed color scale, $T_{\text{ion}} = 40$ eV.

limit imposed on the displayed color scales. These regions coincide with the plasma directly heated and ablated by the laser. They therefore identify the high-temperature source region from which energy is subsequently transferred toward the denser parts of the target.

A narrow band with a temperature of approximately 11.3 eV is also visible around the initial position of the Au layer, $x \simeq 60$ μm, including portions of material that have not yet been reached by the leading shock. This heating is produced by radiation emitted by the laser-generated plasma and absorbed within the highly opaque gold layer. The abrupt reduction in temperature beyond the Au slab confirms that the radiation does not significantly penetrate into the initially not shocked quartz and TMPTA foam, consistently with the main purpose of the gold foil in the reference experiment, where it is used to reduce radiative preheating of the sample [5].

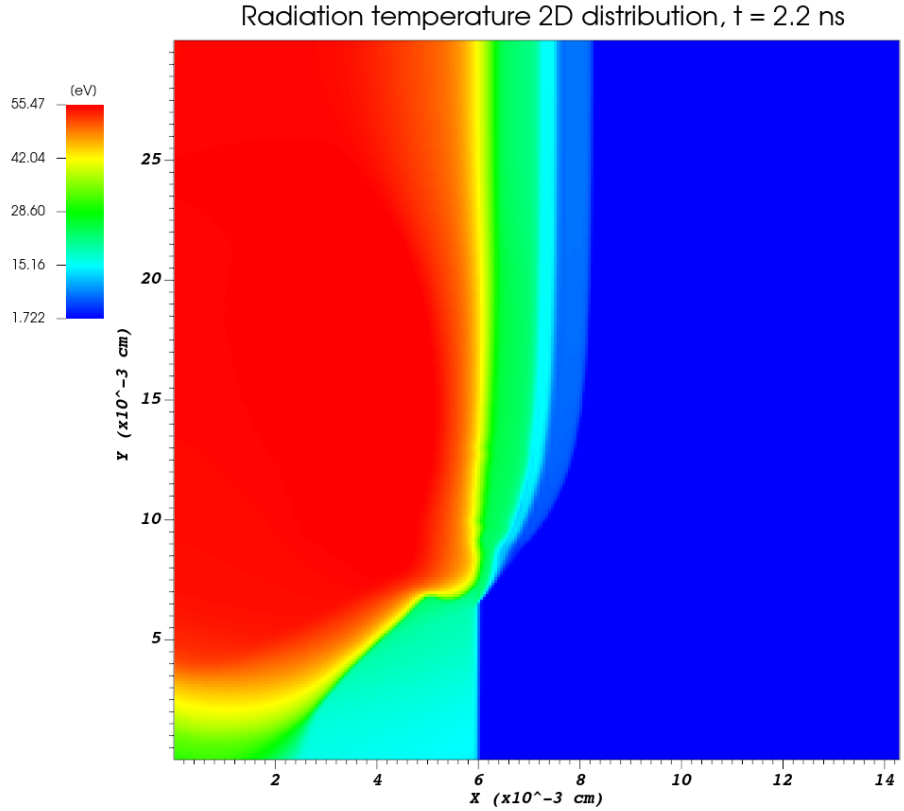

Figure 7.28: Two-dimensional radiation-temperature distribution at $t = 2.2$ ns for the simulation with $I = 8 \times 10^{13}$ $\frac{\mathrm{W}}{\mathrm{cm}^2}$.

The radiation-temperature maps in Figures 7.28 and 7.29 show that, in the quartz and TMPTA foam, T_{rad} follows the same leading-shock geometry identified in the density, pressure, and material-temperature fields. Therefore, also for the radiation component, the heated region is approximately planar inside the transverse interval used for the one-dimensional averaging, whereas it becomes progressively curved near the lower edge of the laser spot. This confirms that the two-dimensional deformation induced by the lateral rarefaction waves affects all the thermodynamic fields associated with the shocked state.

As already discussed from the one-dimensional profiles, the radiation field rapidly reaches the Au layer and is then strongly attenuated. The same behavior is visible in the

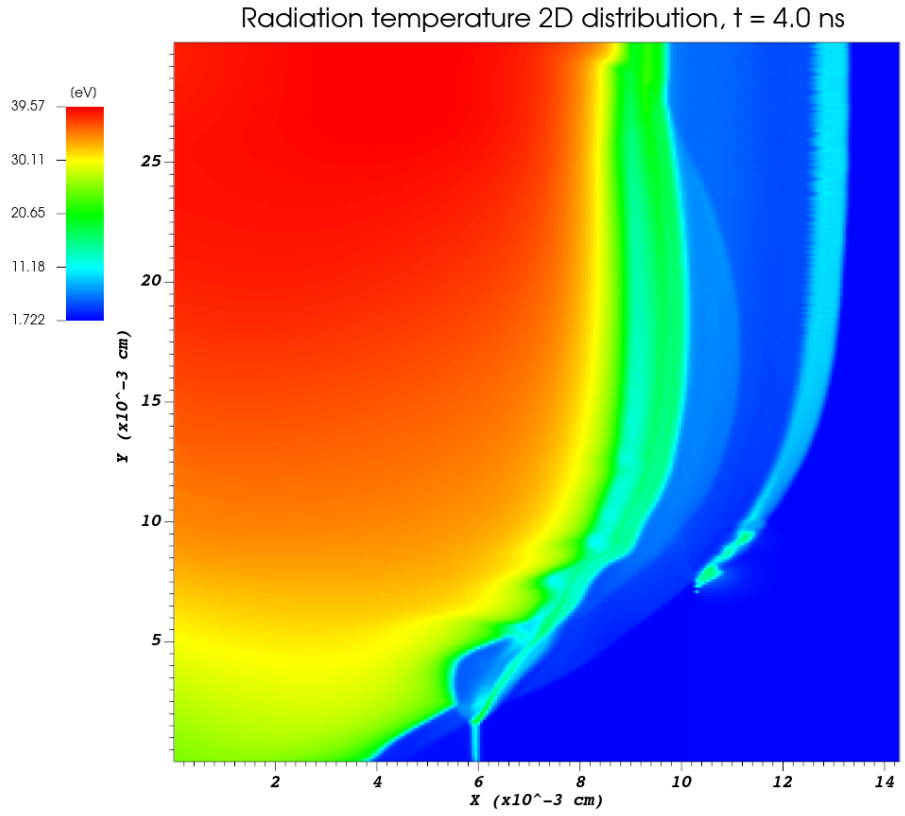

Figure 7.29: Two-dimensional radiation-temperature distribution at $t = 4.0$ ns for the simulation with $I = 8 \times 10^{13} \frac{\mathrm{W}}{\mathrm{cm}^2}$.

two-dimensional maps: beyond the gold foil, T_{rad} decreases sharply before reaching the quartz and TMPTA foam. Thus, also the radiation component of the temperature, in the region used for the quantitative post-shock analysis, remains mainly associated with the shock-heated state.

Overall, the two-dimensional maps show that the simulation cannot be regarded as globally one-dimensional. Strong transverse gradients, curved shock fronts, and lateral plasma expansion are present near the lower boundary of the laser spot. Additional localized and secondary compression structures also develop behind the leading front as a consequence of the sustained laser drive. However, these multidimensional effects remain sufficiently separated from the interval $y \in [230\,,\,297]$ μm during the considered evolution.

Within this averaging band, the leading shock remains approximately planar, and its position depends only weakly on the transverse coordinate. The post-shock regions also exhibit substantially smaller transverse variations than those observed near the edge of the illuminated area. The two-dimensional results therefore support the use of the selected band to construct representative one-dimensional profiles and to extract the longitudinal shock and post-shock quantities employed in the previous analyses.

7.4.2 Critical Density and Energy Deposition

The previous two-dimensional maps showed that the leading shock is approximately planar only in the upper part of the irradiated region, whereas secondary curved compression structures appear behind it. To clarify the origin of these features, the laser energy deposition is now compared with the normalized electron density n_{ele}/n_c.

Using Equation 5.11 and the relation $\omega_L = 2\pi c/\lambda_L$, the critical density associated with the laser wavelength used in the simulation is

$$n_c = \frac{m_{\mathrm{ele}}\pi c^2}{\lambda_L^2 e^2} = 4.018 \times 10^{21}\ \mathrm{cm}^{-3}. \tag{7.13}$$

Here λ_L is the laser wavelength, e is the elementary charge, m_{ele} is the electron mass, and c is the speed of light in the cgs system. Since n_c depends only on the laser wavelength, it remains fixed during the simulation. Conversely, $n_{\mathrm{ele}}(x, y, t)$ evolves as the plasma is heated, ionized, compressed, and expanded. Therefore, the near-critical region, where $n_{\mathrm{ele}}/n_c \simeq 1$, is a dynamic structure and can modify the spatial distribution of the laser deposition during the pulse.

At the beginning of the interaction, the laser deposition is still close to the initial ablator surface. This stage is the most relevant one for the generation of the leading shock analyzed in this work.

Figures 7.30 and 7.31 show that, at $t = 0.4$ ns, the deposited energy is concentrated in the laser-produced plasma in front of the ablator. The deposition region is spatially close to the part of the plasma where n_{ele}/n_c approaches unity, confirming that the laser energy is absorbed in the corona and in the near-critical region, rather than directly inside the denser internal slabs. This early deposition produces the initial ablation pressure that launches the leading shock into the target. For this reason, the leading shock followed in the post-processing is expected to be mainly controlled by the early drive intensity, rather than by the total laser energy deposited later in the domain.

At later times, the plasma corona has already evolved substantially, and the deposition pattern no longer reflects only the initial target geometry.

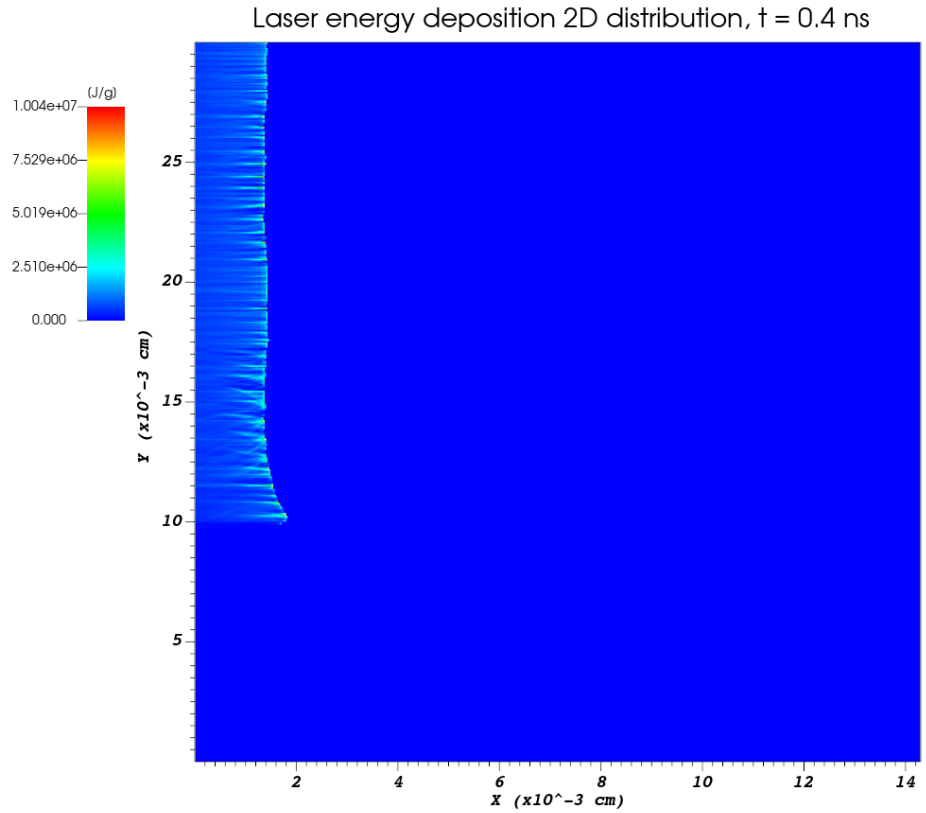

Figure 7.30: Two-dimensional laser energy deposition distribution at $t = 0.4$ ns for the simulation with $I = 8 \times 10^{13}$ $\frac{\mathrm{W}}{\mathrm{cm}^2}$ and a laser-pulse duration of 3.5 ns.

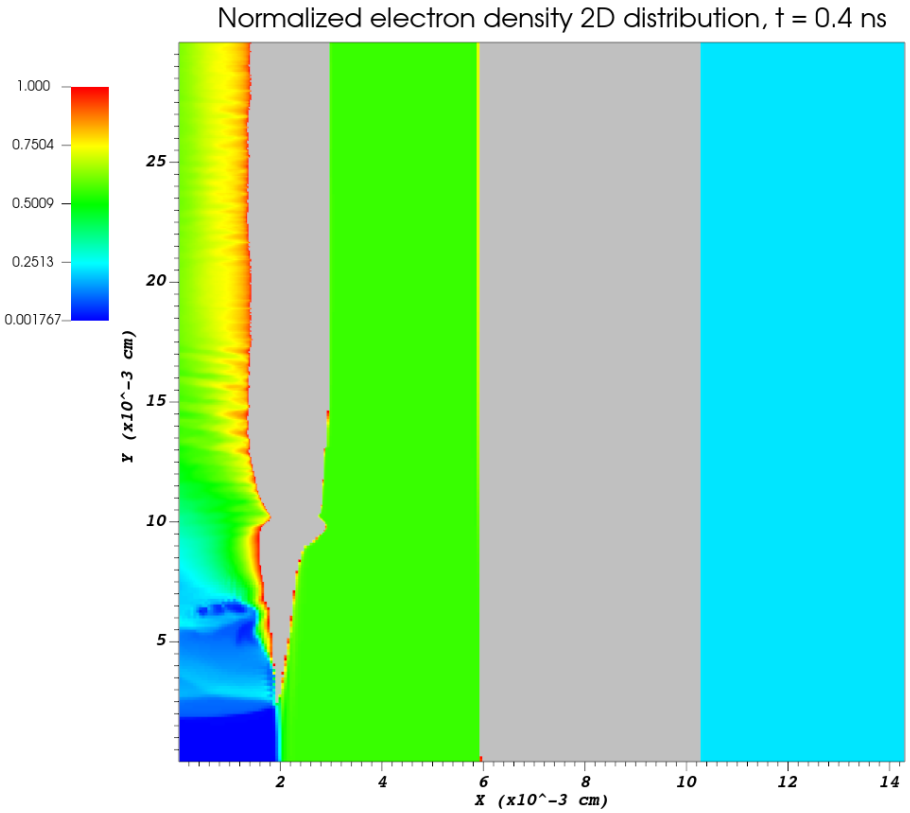

Figure 7.31: Two-dimensional normalized electron-density distribution, n_{ele}/n_c, at $t = 0.4$ ns for the simulation with $I = 8 \times 10^{13}$ $\frac{\text{W}}{\text{cm}^2}$ and a laser-pulse duration of 3.5 ns.

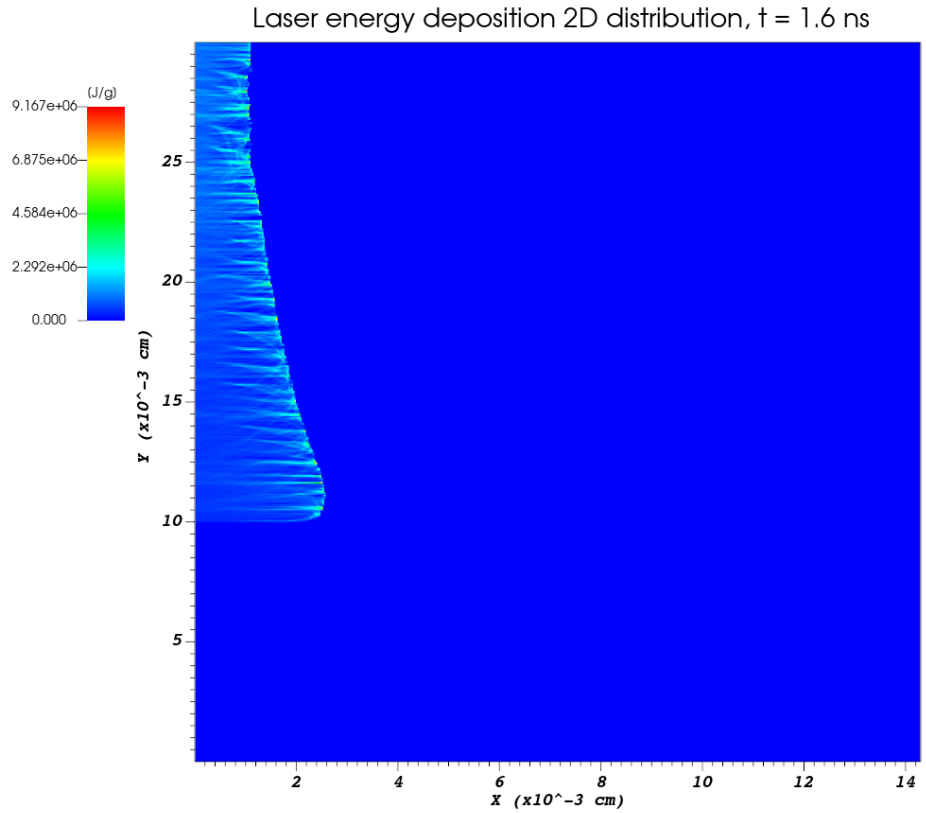

Figure 7.32: Two-dimensional laser energy deposition distribution at $t = 1.6$ ns for the simulation with $I = 8 \times 10^{13}$ $\frac{\mathrm{W}}{\mathrm{cm}^2}$ and a laser-pulse duration of 3.5 ns.

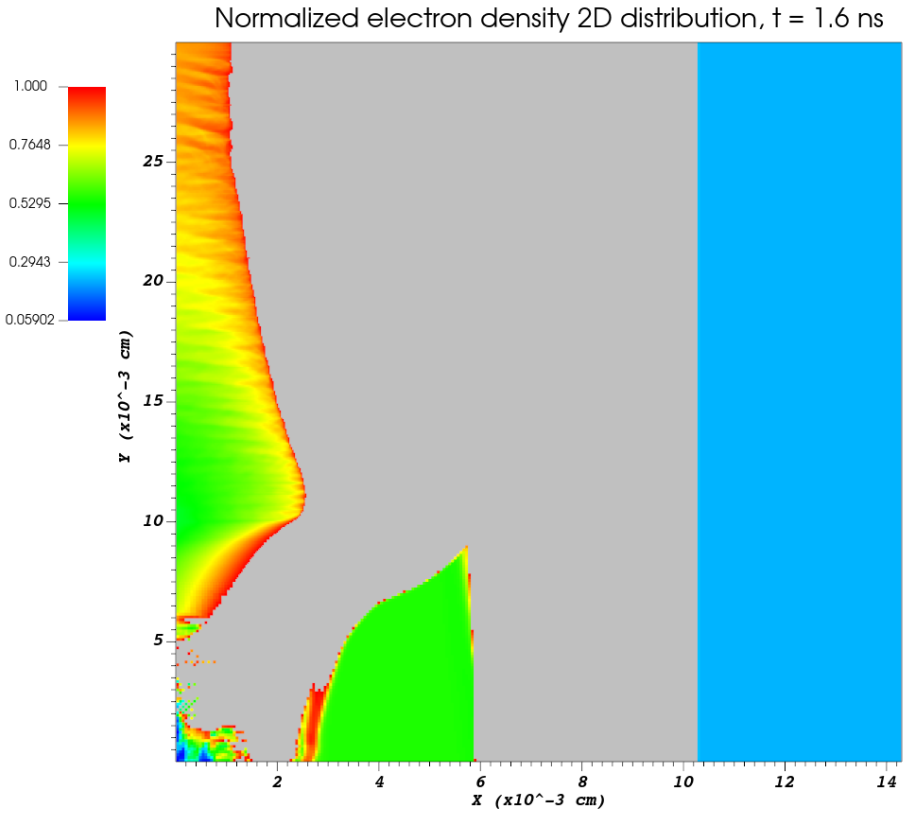

Figure 7.33: Two-dimensional normalized electron-density distribution, n_{ele}/n_c, at $t = 1.6$ ns for the simulation with $I = 8 \times 10^{13}$ $\frac{\text{W}}{\text{cm}^2}$ and a laser-pulse duration of 3.5 ns.

At $t = 1.6$ ns, Figures 7.32 and 7.33 show that the near-critical structure has moved and become curved. This deformation is directly linked to the non-uniform expansion of the laser-produced plasma. Close to the lower edge of the laser spot, around $y \simeq 100$ μm, the plasma is adjacent to a non-irradiated region and can expand both toward the laser side and laterally. This additional expansion reduces the local electron density more efficiently, allowing the laser to penetrate farther before reaching the near-critical region. In the central part of the irradiated area, instead, the plasma expansion is mainly directed toward the left outflow boundary. The lower transverse decompression keeps the electron density higher for a longer time, so the near-critical front remains closer to the laser side and progressively moves toward the left boundary during the transient. The laser deposition follows this evolving structure: the deposition front is no longer approximately vertical, but adapts to the shape of the plasma region where the rays can still propagate and be absorbed. Thus, the deposition pattern becomes a consequence of the evolving coronal plasma, rather than a fixed imprint of the initial laser spot.

The same mechanism becomes even clearer during the later part of the pulse.

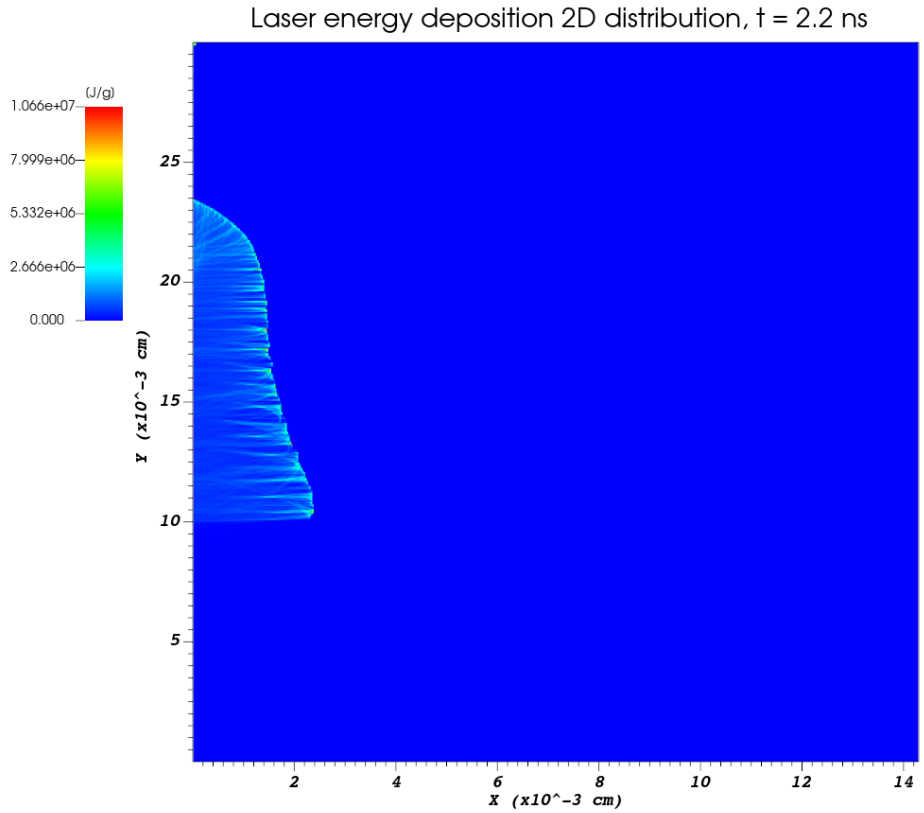

Figure 7.34: Two-dimensional laser energy deposition distribution at $t = 2.2$ ns for the simulation with $I = 8 \times 10^{13}$ $\frac{\mathrm{W}}{\mathrm{cm}^2}$ and a laser-pulse duration of 3.5 ns.

At $t = 2.2$ ns, Figures 7.34 and 7.35 show that the near-critical region has undergone a further deformation. In the central part of the corona, it can approach the left boundary, locally reducing or removing the laser deposition in that region. The deposited energy is instead concentrated where the plasma remains under-critical or near-critical along the ray paths. This explains why the deposition front changes shape during the pulse and

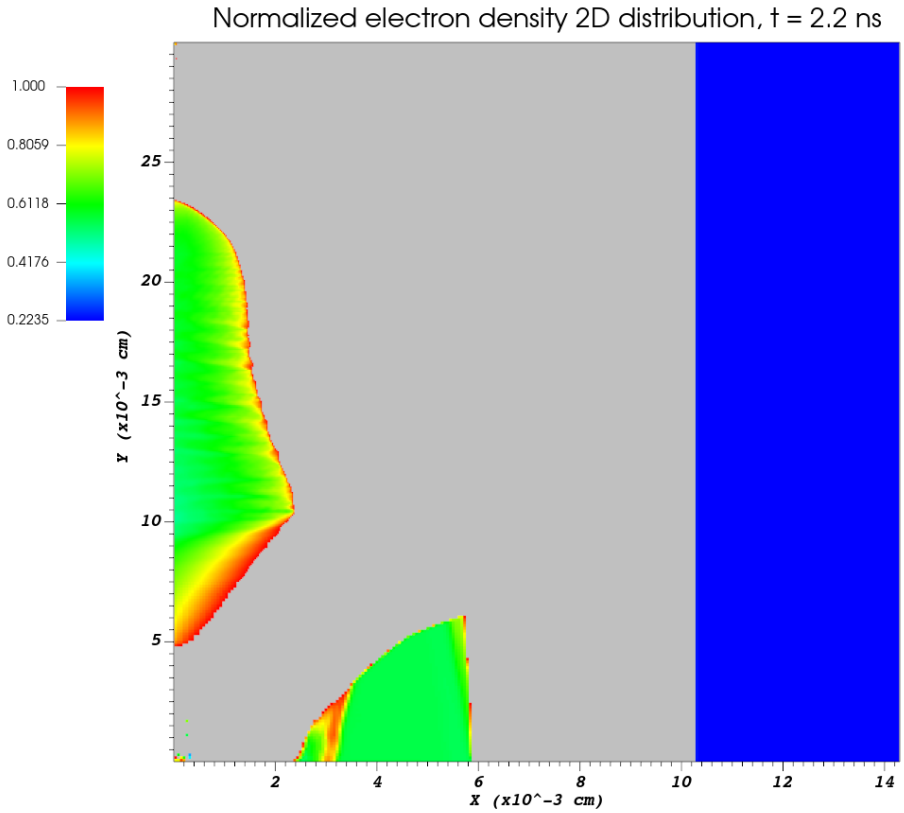

Figure 7.35: Two-dimensional normalized electron-density distribution, n_{ele}/n_c, at $t = 2.2$ ns for the simulation with $I = 8 \times 10^{13}$ $\frac{\text{W}}{\text{cm}^2}$ and a laser-pulse duration of 3.5 ns.

why the later deposition is not expected to generate the same leading-shock structure produced during the initial interaction.

The main conclusion of this comparison is that the first energy deposited during the pulse is responsible for the leading shock analyzed quantitatively in this work, while the later laser deposition mainly contributes to the formation of additional compression structures behind it. These secondary waves, already observed in the pressure, density, velocity, and temperature maps, inherit the curved geometry of the evolving deposition front and of the near-critical plasma region.

A final technical point concerns the early-time deposition map. As shown in Figure 7.30, at $t = 0.4$ ns a weak spurious laser deposition is also visible in the external low-density helium region. This effect is related to the finite ambient density used in the simulation and to its interaction with the ray-tracing algorithm. A more rarefied ambient medium would reduce this contribution, but lower densities are not compatible with the numerical stability of the present setup.

7.5 Model Assessment and Further Improvements

The full-physics laser-driven simulation is developed to reproduce, at a thermofluid-dynamic level, the main sequence occurring in the HEDP experiment of Paddock et al. [5]: laser energy deposition, plasma formation, ablation pressure generation, shock propagation through quartz, and subsequent shock transmission into the TMPTA foam. The objective of this final analysis is therefore not to claim an exact reproduction of each experimental shot, but to assess whether the implemented FLASH model can capture the relevant physical trends and provide post-shock states comparable with the experimental measurements.

The quantitative comparison with the experimental trends is summarized in Table 7.3. For each quantity, the table reports the RMSE, the maximum relative error, and the number of simulated points lying within ±10% of the selected experimental trend.

Quantity	**Quartz**			**TMPTA Foam**		
	RMSE	Max Error	Within 10%	RMSE	Max Error	Within 10%
P	32 GPa	41.4%	1/6	8.1 GPa	18.1%	5/6
u_p	0.11 $\frac{\text{km}}{\text{s}}$	4.90%	6/6	0.44 $\frac{\text{km}}{\text{s}}$	18.7%	0/6
T	0.11 eV	34.7%	0/6	0.12 eV	398%	0/6
U_s	-	-	-	3.18 $\frac{\text{km}}{\text{s}}$	9.17%	6/6

Table 7.3: Summary of the errors obtained in the comparison between the simulated post-shock states and the experimental trends. For each quantity, the root-mean-square error, the maximum relative error, and the number of simulated points lying within ±10% of the selected experimental trend are reported separately for quartz and TMPTA foam.

The comparison shows that the agreement is strongly dependent on the considered quantity. In quartz, the particle velocity is the most accurately reproduced variable, with a maximum relative error of 4.90% and all simulated points within the 10% interval. This indicates that the hydrodynamic response associated with the material motion behind the shock is well captured. The agreement is less satisfactory for the quartz pressure, for which only one point lies within the 10% band and the maximum relative error reaches 41.4%. This larger deviation is consistent with the temporal analysis of the post-shock plateau,

which showed that pressure is one of the quantities most affected by the transient decay of the shocked state. The quartz temperature also shows limited agreement in relative terms.

For the TMPTA foam, the best agreement is obtained for the shock velocity. All simulated points lie within the 10% interval and the maximum relative error is 9.17%. This is an important result, because the foam shock velocity is one of the most direct indicators of the transmitted shock strength. The foam pressure also follows the experimental trend reasonably well, with five out of six points within the 10% interval and a maximum relative error of 18.1%. The particle velocity shows a larger systematic deviation, since none of the points falls within the 10% band, although the maximum error remains below 20%.

The weakest agreement is obtained for the foam temperature, which remains outside the experimental trend. In particular, the largest deviation reported in Table 7.3 is associated with the radiation temperature. Unlike what would be expected for a post-shock state in thermal equilibrium, T_{rad} does not relax to the same value as the matter temperatures T_{ele} and T_{ion}. However, even when only the electron and ion temperatures are considered, the discrepancy remains significant, with a maximum relative error of approximately 242%. This comparison therefore indicates that the model reproduces the hydrodynamic and kinematic trends more reliably than the thermal state, especially in the foam.

This behavior is consistent with the nature of the quantities involved. Temperature is the most difficult variable to compare, both numerically and experimentally. In the simulation, it is directly affected by the tabulated EOS, electron-ion coupling, radiation and electron transport. In the experiment, temperature measurements are also less direct than velocity measurements and are associated with larger diagnostic uncertainty. For this reason, the temperature disagreement should be interpreted as an indication that the present model is more reliable for describing shock dynamics than for providing a fully quantitative prediction of the shocked thermal state. Nevertheless, the temperature scale obtained with the full-physics simulation is much closer to the experimental one than in the simplified gamma-law baseline, where the shocked temperatures were completely outside the relevant experimental range.

A further positive indication comes from the global trend of the simulated data. Although the absolute agreement depends on the considered quantity, the proportionality observed in the comparison plots is generally preserved: larger quartz shock velocities, which are directly related to larger laser intensities, correspond to larger post-shock quantities in both quartz and TMPTA foam. This means that the simulation captures the expected ordering of the shots according to shock strength, even when the absolute values are affected by model limitations.

The larger error spans are generally observed in quartz, especially for pressure. This is consistent with the temporal plateau analysis, where the quartz post-shock state was found to decrease during the shock transit. The most plausible interpretation is that rarefaction waves generated behind the shock progressively interact with the compressed region, reducing the pressure and broadening the range between the minimum and maximum plateau values. As a consequence, the comparison with the experimental pressure trend is less constrained than for quantities less affected by this transient decay. At the same time, the pressure-offset correction introduced to avoid the spurious expansion of the initially heated materials appears to be effective, since the simulated pressures remain on the same scale as the experimental range.

Beyond the transient behavior of the post-shock plateau, the remaining one-dimensional

profiles and two-dimensional distributions are qualitatively consistent with the expected physics of the problem. The laser deposits energy in the low-density and near-critical plasma region, and the deposition region follows the evolution of the critical-density front as the plasma expands and ionizes. The heated material expands, and the resulting ablation pressure launches a shock into the multilayer target. The shock is transmitted across the material interfaces, producing compressed states in quartz and later in the TMPTA foam. The one-dimensional profiles show the expected increase in density, pressure, particle velocity, and temperature across the shock front, while the two-dimensional maps reveal the finite transverse extent of the driven region and the development of secondary compression and rarefaction structures.

A major limitation of the present model is related to the equation of state. The available SESAME tables [19] impose a minimum initial temperature of $T_{\mathrm{in}} = 20000$ K, corresponding to approximately 1.72 eV. This value is much higher than room temperature and therefore produces an initial pre-shock state that is not identical to the experimental one. Since the shock velocity and the post-shock thermodynamic state depend on the Hugoniot of the material, this initial offset can affect the quantitative comparison with the experimental trends. In particular, part of the observed overestimation of the shock velocity may be connected to the combined effect of the elevated initial temperature, the tabulated EOS, and therefore the thermodynamic region sampled during the simulation. This point shows that a more detailed study of the compatibility between the SESAME tables and FLASH is required. In particular, the pre-processing of EOS tables through tools such as EOSPAC6 [22] and opacplot2 [23] should be analyzed more systematically. Such an analysis would make it possible to verify the validity range of the tables, the consistency of the thermodynamic quantities used by FLASH, and the numerical behavior of the EOS calls. This is especially important because the EOS affects not only the physical Hugoniot, but also the numerical stability and time-step of the simulation.

The most evident numerical consequence of the EOS treatment is the appearance of a localized, non-physical ion-temperature hotspot in the helium region, close to the laser-deposition zone. This feature is shown in Figure 7.36, where the ion temperature is plotted at three representative times with the color scale capped at 1000 eV. The cap itself is already far above the physically relevant temperature range for the ionized helium in the laser-illuminated region, which remains of the order of a few hundred eV. It is therefore not physically meaningful for a non-shocked region outside the main laser-heated channel to reach much higher ion temperatures.

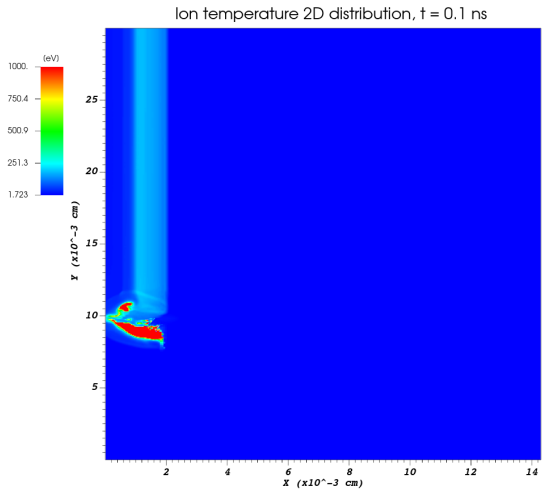

(a) $t = 0.1$ ns

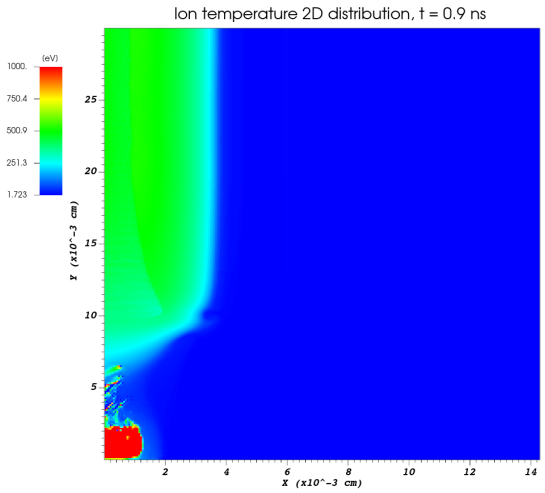

(b) $t = 0.9$ ns

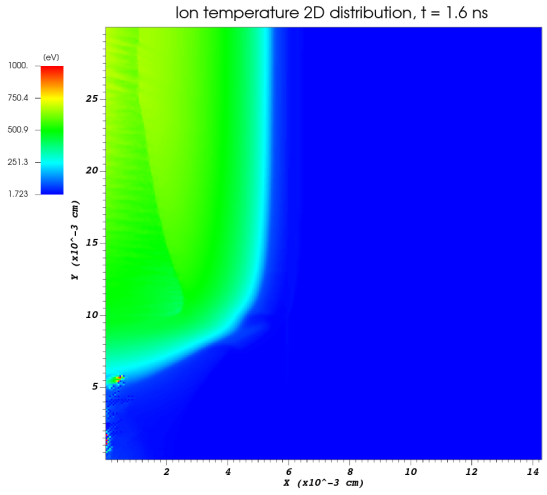

(c) $t = 1.6$ ns

Figure 7.36: Evolution of the two-dimensional ion-temperature field during the early laser-driven transient. The panels show T_{ion} at (a) $t = 0.1$ ns, (b) $t = 0.9$ ns, and (c) $t = 1.6$ ns. The color scale is capped at 1000 eV.

The hotspot is located outside the physical target and is therefore a specific issue of the low-density helium region. For this reason, it seems to not directly affect the ablation region, the shock-generation process, or the extracted quartz and TMPTA foam post-shock states used in the comparison with the experiment. Moreover, as the transient evolves, this structure is progressively advected away from the region relevant to the target dynamics. Its main consequence is therefore numerical rather than physically related to the shock generation and propagation under study. The very high local ion temperature increases the local sound speed and reduces the maximum timestep allowed by the CFL condition, making this helium hotspot the main timestep-limiting region of the simulation.

The helium density used in the simulation is also connected to this numerical issue. From a physical point of view, a lower helium density would be preferable, because it would reduce the amount of material available for spurious energy deposition before the ablation surface. For instance, the reference `LaserSlab` problem uses a much lower ambient density, of the order of 10^{-5} g cm^{-3} [11]. In the present case, however, such a low density amplified the non-physical T_{ion} hotspot and further reduced the timestep. For this reason, the helium density was increased to 10^{-3} g cm^{-3}. This choice should be interpreted as a numerical compromise: it is not the ideal representation of a strongly rarefied ambient medium, but it mitigates the timestep limitation while keeping the problematic region outside the target portion used for the post-shock analysis.

The main remaining modeling limitation concerns the description of the TMPTA foam. In the present simulation, the foam is treated as a homogeneous material at the average density, without resolving its porous microstructure. This approximation is consistent with the experimental interpretation based on an effective foam EOS, but it removes all pore-scale effects from the model. In particular, the simulation cannot capture the local interaction between the shock and the solid foam skeleton, the pore-filling and homogenization process, or possible differences between the thermodynamic response of a real porous medium and that of a uniform low-density material. This limitation is especially relevant for the foam post-shock state, where the comparison with the experiment is more sensitive to the assumed material model.

Furthermore, the flux limiters used for electron conduction and radiation diffusion were kept equal to the reference `LaserSlab` setup [11] and were not subjected to a dedicated sensitivity analysis. Since both electron thermal transport and radiation diffusion influence the energy redistribution from the deposition region to the pressure build-up region, their impact on the ablation pressure and on the final post-shock state should be investigated in future work. Similar sensitivity studies should also be performed on the mesh refinement strategy, the radiation group structure, and the opacity tables. These aspects are not expected to be the primary source of the numerical issues observed in the present work, but they can affect the quantitative predictability of the model once the EOS treatment is better controlled.

Overall, the simulation provides a physically consistent starting point for studying laser-driven HEDP experiments with FLASH. It captures the main hydrodynamic mechanisms expected in the problem: laser absorption, ablation pressure generation, shock propagation, transmission across material interfaces, post-shock compression, and two-dimensional rarefaction effects. The comparison with the experiment shows that several hydrodynamic and kinematic trends are reproduced with reasonable accuracy, especially the quartz particle velocity, the TMPTA shock velocity, and the TMPTA pressure. At the same time, the disagreement in temperature and the sensitivity to the EOS treatment show that the model is not yet quantitatively predictive for all thermodynamic variables.

The most important open issues are the EOS treatment, the numerical hotspot in the low-density helium region, the sensitivity to transport limiters, and the homogeneous description of the foam.

Future improvements should therefore focus first on a more controlled use of EOS tables in FLASH. A systematic study of the EOS pre-processing chain, the minimum table temperature, and the low-density behavior of the tables is necessary to remove or mitigate the non-physical ion-temperature hotspot and to obtain a more reliable initial state. In parallel, sensitivity studies on electron conduction and radiation transport limiters should be performed to assess how energy transport affects the generated ablation pressure and the shock strength. Opacity tables should also be included in this broader sensitivity analysis, although their role is expected to be secondary with respect to the EOS issues discussed above. Once these aspects are better controlled, the same setup could be used to study how different material models and target configurations affect shock generation and propagation in laser-driven HEDP targets.

Despite these limitations, the developed setup provides a useful basis for future studies in the HEDP and ICF fields. In particular, it could be used to investigate how different foam configurations interact with the laser and modify the subsequent shock-generation process. One possible application would be to replace the homogeneous CH ablator with a foam ablator, allowing a direct comparison between shocks generated by a homogeneous ablator and by an inhomogeneous porous structure. This would make it possible to assess whether the use of a foam layer changes the ablation dynamics, the pressure build-up, and the shock transmitted into the target.

Two possible modeling strategies can be followed to include the foam structure. The first one consists in resolving the foam porosity directly within the same hydrodynamic code. This approach has been used in simulations of laser irradiation of targets with a specific microstructure [26], but it requires simplified and regular porosity distributions, such as superposed regular grids, in order to keep the computational cost acceptable. Even with these simplifications, the required mesh resolution remains demanding, because the pore-scale geometry must be resolved together with the macroscopic target evolution. This strategy is therefore useful when the objective is to study explicitly the interaction between the laser, the shock, and an idealized porous geometry, but it becomes computationally expensive for realistic foam morphologies. The second possibility is a multi-scale approach. In this case, a dedicated micro-scale model is used to describe the response of a characteristic foam pore to laser irradiation. The information obtained at the micro-scale is then used to characterize the plasma in the macro-scale hydrodynamic simulation, without explicitly resolving the full foam morphology. This strategy avoids the need for an extremely fine mesh in the complete target simulation, while still retaining information on the foam structure through an effective plasma characterization [27]. Moreover, since the pore response is treated separately from the full target simulation, more complex pore structures could be analyzed without directly increasing the cost of the macroscopic calculation. Such an approach would be particularly useful to test the validity of the homogeneous-density approximation for different foam geometries and irradiation conditions.

Chapter 8

Conclusions

The objective of this thesis was to develop and assess a numerical framework for the simulation of laser-driven shock experiments in high energy density physics, with particular attention to configurations relevant for inertial confinement fusion. The work was organized as a progressive modeling path. A first simplified gamma-law setup was used to isolate the purely hydrodynamic response of the multilayer target, while the main part of the thesis was devoted to the construction of a full-physics laser-driven model able to reproduce the physical sequence of the reference experiment: laser energy deposition, plasma formation, ablation pressure generation, shock propagation through quartz, and shock transmission into the TMPTA foam.

The gamma-law model represented a useful preliminary exercise. In that setup, the laser-target interaction was not simulated explicitly and the shock was generated by imposing an equivalent pressure drive. The materials were described through effective ideal-gas parameters, namely γ and R, chosen to reproduce selected hydrodynamic properties of the experimental system. This approach is therefore not a predictive material model in a strict sense, because its closure relies on information that must be obtained from experimental data, Hugoniot relations, or other reference calculations. Nevertheless, within this limited scope, the model was able to reproduce the main hydrodynamic features of the system with reasonable consistency. In particular, it captured the propagation of the shock, its transmission across the quartz-TMPTA interface, and the qualitative response of the shocked materials.

The main value of the gamma-law baseline is therefore methodological. It shows how much of the experiment can be interpreted in terms of shock dynamics alone, without introducing tabulated equations of state, opacity data, laser absorption, radiation transport, or a multi-temperature plasma description. Its predictive capability remains limited to qualitative or semi-quantitative studies, for example to explore the hydrodynamic response of equivalent materials by varying γ and R. Such a model could still be useful in situations where no EOS tables, opacity data, or detailed plasma information are available. However, it cannot provide a reliable thermal description of the shocked state. The temperature is not reproduced correctly because the gamma-law EOS converts internal energy into temperature through a single ideal-gas-like relation, without accounting for cold compression, ionic and electronic thermal contributions, ionization effects, or the real partition of energy among the material degrees of freedom.

The full-physics setup represents the main modeling result of this thesis. Differently from the pressure-driven baseline, the shock is not imposed through a fixed initial condition, but arises from the laser-matter interaction itself. The use of a three-temperature

radiation-hydrodynamic model allows the electron, ion, and radiation temperatures to evolve separately, while tabulated EOS data, laser energy deposition, electron thermal conduction, radiation transport, and electron-ion energy exchange provide a much more realistic description of the HEDP regime. In this sense, the full-physics model considerably extends the predictive capability of the simulation, because it does not only propagate a prescribed shock, but attempts to reproduce the physical mechanism by which the shock is generated.

The comparison with the experimental trends shows that the full-physics simulation is physically consistent and reasonably well configured. The model captures the main hydrodynamic mechanisms expected in the experiment: laser absorption, ablation-pressure build-up, shock propagation, transmission across material interfaces, post-shock compression, and two-dimensional rarefaction effects. The agreement is strongest for the hydrodynamic and kinematic observables, such as the quartz particle velocity, the TMPTA shock velocity, and the TMPTA pressure. The thermal state is more difficult to reproduce quantitatively, especially in the foam. However, the full-physics setup still represents a clear improvement with respect to the gamma-law baseline, because the simulated temperatures are brought to the correct physical order of magnitude rather than being completely outside the experimental scale.

The remaining discrepancies are mainly related to the increased physical and numerical complexity of the full-physics model. The simulation results depend on several coupled ingredients: the tabulated EOS, the minimum temperature allowed by the tables, the opacity treatment, the electron-conduction and radiation-diffusion limiters, the radiation group structure, the mesh refinement strategy, and the post-processing procedure used to extract representative post-shock states. Among these aspects, the treatment of EOS appears to be the most critical. The initial temperature imposed by the available tables is higher than the experimental room-temperature state, and the low-density behavior of the tables is connected to the appearance of a non-physical ion-temperature hotspot in the helium region. Although this hotspot is outside the target region, it strongly affects the computational cost by limiting the time-step through the CFL condition.

Despite these limitations, the full-physics simulation provides a solid starting point for future studies. The next steps should focus on a systematic sensitivity analysis of the EOS pre-processing chain, the validity range of the tables, the opacity data, the transport limiters, the radiation group structure, and the mesh refinement strategy. These studies would make it possible to distinguish numerical effects from genuine physical trends and to improve the quantitative agreement with the experiment. A more controlled treatment of the EOS tables is particularly important, because the EOS affects not only the Hugoniot and the post-shock thermodynamic state, but also the numerical stability and computational efficiency of the simulation.

A further possible development concerns the treatment of the TMPTA foam. In the present model, the foam is described as a homogeneous material at its average density. This choice is consistent with the comparison performed in this work, since the experimental data are interpreted through an effective Hugoniot of the foam. Therefore, the homogeneous treatment should not be considered the main source of the discrepancies observed in the present results. At most, its effect should be comparable to the difference between the homogeneous SESAME description and the experimental data. A fully resolved porous geometry would instead represent a more advanced modeling step, to be considered after the full-physics setup has been made quantitatively more robust. Starting from the present simulation, future studies could explicitly include simplified

foam microstructures, or reduced models of foam homogenization, in order to investigate pore-scale plasma formation, local shock propagation, and possible morphology-dependent effects.

Beyond the physical results, this thesis also developed a complete numerical and post-processing workflow. The work included the construction of the FLASH setup, the initialization of the multilayer target, the definition of the laser drive, the treatment of boundary conditions and AMR refinement, the extraction of one-dimensional profiles from two-dimensional data, the tracking of the shock position, the identification of post-shock plateaus, and the comparison of simulated quantities with experimental trends. This workflow is an important outcome, because it makes the simulation strategy reproducible and provides a practical basis for future improvements and sensitivity studies.

In conclusion, the two setups developed in this work clarify two different levels of modeling. The gamma-law simulation shows the possibilities and the intrinsic limits of a strongly simplified hydrodynamic description, which can be useful only as a preliminary or exploratory tool when detailed material and plasma data are unavailable. The full-physics setup, instead, represents the main result and the most promising framework for future investigations. It already reproduces the principal hydrodynamic and kinematic features of the reference experiment and provides a physically consistent basis for studying shock generation and evolution in laser-irradiated targets. With further work on EOS tables, transport modeling, numerical sensitivity, and foam morphology, this framework can be developed into a more quantitatively predictive tool for HEDP and ICF-relevant simulations.

Bibliography

[1] Kenneth S. Krane. *Introductory Nuclear Physics*. John Wiley & Sons, New York, 1988.

[2] R. P. Drake. *High-Energy-Density Physics: Fundamentals, Inertial Fusion, and Experimental Astrophysics*. Springer, Berlin Heidelberg, 2006.

[3] Frédéric Perez. Laser-produced plasma physics. Lecture notes, Master 2 QLMN, 2023. Academic year 2023–2024.

[4] B. Fryxell, K. Olson, P. Ricker, F. X. Timmes, M. Zingale, D. Q. Lamb, P. MacNeice, R. Rosner, J. W. Truran, and H. Tufo. Flash: An adaptive mesh hydrodynamics code for modeling astrophysical thermonuclear flashes. *The Astrophysical Journal Supplement Series*, 131:273–334, 2000.

[5] R. W. Paddock et al. Measuring the principal hugoniot of inertial-confinement-fusion-relevant tmpta plastic foams. *Physical Review E*, 107:025206, 2023.

[6] E. F. Toro. *Riemann Solvers and Numerical Methods for Fluid Dynamics*. Springer, 3 edition, 2009.

[7] Ya. B. Zel'dovich and Yu. P. Raizer. *Physics of Shock Waves and High-Temperature Hydrodynamic Phenomena*. Dover Publications, 2002. Edited by W. D. Hayes and R. F. Probstein.

[8] R. Jishnu Chandran and A. Salih. Development of a benchmark solution in compressible liquid flows: Analytical solution to the water shock tube problem. *Journal of Thermal Analysis and Calorimetry*, 147:5279–5292, 2022.

[9] Shalom Eliezer. *The Interaction of High-Power Lasers with Plasmas*. Series in Plasma Physics. Institute of Physics Publishing, Bristol and Philadelphia, 2002.

[10] Randall J. LeVeque. *Finite Volume Methods for Hyperbolic Problems*. Cambridge Texts in Applied Mathematics. Cambridge University Press, Cambridge, United Kingdom, 2002.

[11] Flash Center for Computational Science. *FLASH User's Guide, Version 4.8*, May 2024. Last updated May 6, 2024.

[12] The HDF Group. HDF5, 2026. Hierarchical Data Format, version 5.

[13] HPC@PoliTO. *The HPC@PoliTO User Guide*, June 2025. Version 0.4, draft.

[14] M. J. Turk, B. D. Smith, J. S. Oishi, S. Skory, S. W. Skillman, T. Abel, and M. L. Norman. yt: A Multi-code Analysis Toolkit for Astrophysical Simulation Data. *The Astrophysical Journal Supplement Series*, 192:9, January 2011.

[15] Allen C. Robinson. The mie-grüneisen power equation of state. Technical Report SAND2019-6025, Sandia National Laboratories, 2019.

[16] James McHardy. An introduction to the theory and use of sesame equations of state. Technical Report LA-14503, Los Alamos National Laboratory, 2018.

[17] Steffen Faik. Feos: A new equation-of-state code for hot dense matter. Technical report, Goethe University Frankfurt, 2016. Version 16.7 Package Documentation.

[18] Jeffrey P. Freidberg. *Plasma Physics and Fusion Energy*. Cambridge University Press, Cambridge, United Kingdom, 2007.

[19] Daniel G. Sheppard and David A. Pimentel. SESAME: The Los Alamos National Laboratory's Tabulated Equation of State Database Description with Extensions for Multi-phase Representations. Report LA-UR-25-26258, Los Alamos National Laboratory, July 2025. Rev. 1, issued July 7, 2025.

[20] Los Alamos National Laboratory. TOPS Opacities. `https://aphysics2.lanl.gov/`. Los Alamos T-1 Opacities; Los Alamos Report No. LA-UR-01-1257.

[21] Tomasz Błeński and Jacques Ligou. Average atom calculations of radiation opacities for gold at high density and temperature. *Journal de Physique Colloques*, 49(C7):C7–259–C7–266, 1988. HAL Id: jpa-00228215.

[22] David A. Pimentel. *EOSPAC User's Manual: Version 6.5*. Los Alamos National Laboratory, second edition edition, December 2025. Revision 4, Artifact ID: EOSPAC6-02-01.

[23] Flash Center for Computational Science. Opacplot2 1.0 Documentation. `https://opacplot2.readthedocs.io/en/latest/index.html`, 2016.

[24] HYPRE Project Developers. hypre: High performance preconditioners.

[25] Hank Childs, Eric Brugger, Brad Whitlock, Jeremy Meredith, Sean Ahern, David Pugmire, Kathleen Biagas, Mark C. Miller, Cyrus Harrison, Gunther H. Weber, Hari Krishnan, Thomas Fogal, Allen Sanderson, Christoph Garth, E. Wes Bethel, David Camp, Oliver Rubel, Marc Durant, Jean M. Favre, and Paul Navratil. High Performance Visualization–Enabling Extreme-Scale Scientific Insight, 2012.

[26] M. Cipriani, F. Consoli, M. Scisciò, A. Solovjovas, I. A. Petsi, M. Malinauskas, P. Andreoli, G. Cristofari, E. Di Ferdinando, and G. Di Giorgio. Experimental and simulation study on high-power laser irradiation of 3d-printed microstructures. *Matter and Radiation at Extremes*, 11(2):027401, 2026.

[27] J. Velechovsky, J. Limpouch, R. Liska, and V. Tikhonchuk. Hydrodynamic modeling of laser interaction with micro-structured targets. *Plasma Physics and Controlled Fusion*, 58(9):095004, 2016.